LBNL-42058

ERNEST ORLANDO LAWRENCE BERKELEY NATIONAL LABORATORY

Seismic Imaging of the Shallow Subsurface with High Frequency Seismic Measurements

Bruno Kaelin

Earth Sciences Division

July 1998

Ph.D. Thesis

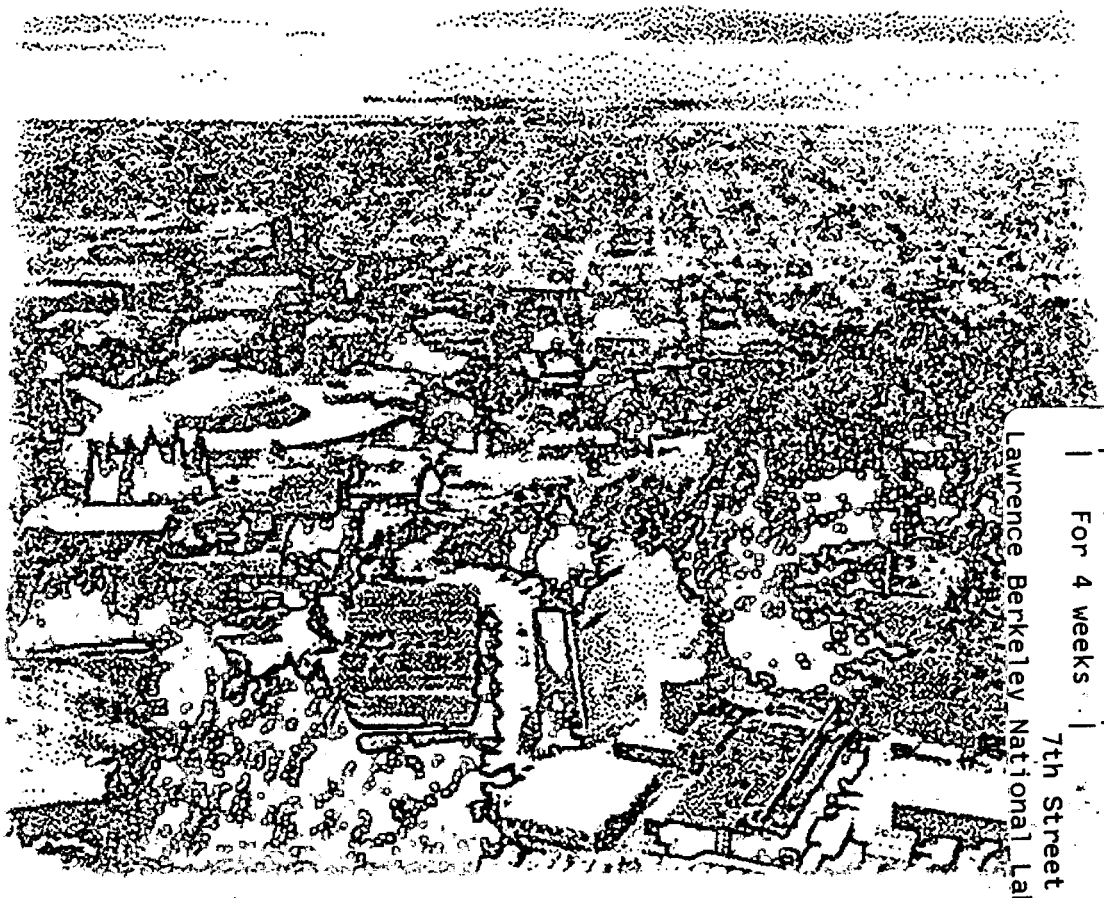

LOAN COPY
Circulates
For 4 weeks
7th Street Warehouse
Lawrence Berkeley National Laboratory

LBNL-42058
Copy 2

DISCLAIMER

This document was prepared as an account of work sponsored by the United States Government. While this document is believed to contain correct information, neither the United States Government nor any agency thereof, nor the Regents of the University of California, nor any of their employees, makes any warranty, express or implied, or assumes any legal responsibility for the accuracy, completeness, or usefulness of any information, apparatus, product, or process disclosed, or represents that its use would not infringe privately owned rights. Reference herein to any specific commercial product, process, or service by its trade name, trademark, manufacturer, or otherwise, does not necessarily constitute or imply its endorsement, recommendation, or favoring by the United States Government or any agency thereof, or the Regents of the University of California. The views and opinions of authors expressed herein do not necessarily state or reflect those of the United States Government or any agency thereof or the Regents of the University of California.

LBNL-42058

Seismic imaging of the shallow subsurface with high frequency seismic measurements

Bruno Kaelin

Ph.D. Thesis

Department of Geology and Geophysics
University of California, Berkeley

and

Earth Science Division
Ernest Orlando Lawrence Berkeley National Laboratory
University of California
Berkeley, CA 94720

July 1998

This work was done at the Center for Computational Seismology supported by the Assistant Secretary for Fossil Energy, Office of Oil, Gas and Shale Technologies, Federal Technology Center, of U.S. Department of Energy under Contract No. DE-AC03-76SF00098.

Abstract

Seismic imaging of the shallow subsurface

with high frequency seismic measurements

by

Bruno Kaelin

Doctor of Philosophy in Geophysics

University of California at Berkeley

Professor Lane R. Johnson, Chair

Elastic wave propagation in highly heterogeneous media is investigated and theoretical calculations and field measurements are presented. In the first part the dynamic composite elastic medium (DYCEM) theory is derived for one-dimensional stratified media. A self-consistent method using the scattering functions of the individual layers is formulated, which allows the calculation of phase velocity, attenuation and waveform. In the low frequency limit the self-consistent formulation is consistent with the Reuss average and in the high frequency limit it yields the correct ray theory average velocity. The comparison with complete numerical solutions shows that the DYCEM theory predicts the coherent wave through randomly layered media. In the second part the DYCEM theory has been generalized for three-dimensional inclusions. The specific case of spherical inclusions is calculated with the exact scattering functions and com-

pared with several low frequency approximations. Spectra and waveforms for materials with solid and liquid inclusions in a solid matrix are presented. The results show that the exact scattering functions are required to adequately describe wave propagation at all frequencies. In the third part log and VSP data of partially water saturated tuffs in the Yucca Mountain region of Nevada are analyzed. The anomalous slow seismic velocities can be explained by combining self-consistent theories for pores and cracks. The effective matrix velocities in the studied tuffs deviate strongly from the individual mineral velocities. This effect may be due to the presence of two dimensional inhomogeneities like cracks and grain contacts. The fourth part analyzes an air injection experiment in a shallow fractured limestone, which has shown large effects on the amplitude, but small effects on the travel time of the transmitted seismic waves. The large amplitude decrease during the experiment is mainly due to the impedance contrast between the small velocities of gas-water mixtures inside the fracture and the formation. The slow velocities inside the fracture allow an estimation of aperture and gas concentration profiles. The aperture estimates range from less than one millimeter to a few millimeters, which is comparable to previous tracer tests.

Contents

List of Figures v

List of Tables x

1 Introduction 1

2 Dynamic composite elastic medium theory. Part I. One-dimensional media 5

2.1 Abstract 5
2.2 Introduction 6
2.3 Dynamic composite elastic medium theory 8
2.3.1 Non-self-consistent theory 9
2.3.2 Self-consistent theory 11
2.3.3 Low and high frequency approximations 13
2.4 Numerical simulations 15
2.4.1 Perturbed media 16
2.4.2 Binary media 25
2.5 Discussion and conclusions 29

3 Dynamic composite elastic medium theory. Part II. Three-dimensional media 30

3.1 Abstract 30
3.2 Introduction 31
3.3 General dynamic composite elastic medium theory (DYCEM) . 32
3.3.1 Non-self-consistent theory 37
3.3.2 Self-consistent theory 38
3.4 Dynamic composite elastic medium theory for spherical inclusions 40
3.4.1 Low frequency approximations 42
3.5 Viscous fluids 45
3.6 Examples 46

3.6.1 Model 1: Solid spherical inclusions with identical radii in a solid matrix 47
3.6.2 Model 1: Solid spherical inclusions with log-normal distributed radii in a solid matrix 54
3.6.3 Model 2: Liquid spherical inclusions with identical radii in a solid matrix 57
3.7 Discussion and conclusions 62

4 Seismic rock properties of partially water saturated tuffs in the Yucca Mountain region derived from well logs and VSP data 64
4.1 Abstract 64
4.2 Introduction 65
4.3 Long wavelength theory for seismic velocities in porous media . 66
4.4 Application for partially water saturated tuffs 70
4.4.1 Log data and VSP data 70
4.4.2 Calculations 71
4.5 Discussion 78
4.6 Conclusions 79

5 Using seismic crosswell surveys to determine the aperture of partially water-saturated fractures 81
5.1 Abstract 81
5.2 Introduction 82
5.3 Theory 83
5.3.1 Effect of a single vertical fracture on seismic waves . . . 83
5.3.2 Seismic properties of air-water mixtures 85
5.3.3 Example of a single fracture with 0.5 mm aperture . . . 89
5.4 Inversion method 92
5.4.1 Windowing the direct wave 92
5.4.2 Defining the objective function 93
5.5 Data and results 95
5.5.1 Seismic monitor survey: data and inversion results 96
5.5.2 Crosswell survey: data and inversion results 101
5.6 Discussion 109
5.7 Conclusions 110
5.8 Appendix: Confidence interval of the parameter estimates . . . 112

References 115

A Comparison between Berryman's theory and Gassmann's equations 125

List of Figures

2.1 Schematic illustration of a transmitted wave through a homogeneous background with velocity v_0 and density ρ_0, and one layer with velocity v_1, density ρ_1 and thickness d_1. The transmitted wave and all reverberations within one layer are considered in the dynamic composite elastic medium theory. 9

2.2 Velocity profiles for the numerical simulations: a) 10% perturbation in velocity and layer thickness, b) 20% perturbation in velocity and layer thickness, c) periodic layering of a binary medium with 5% perturbation in velocity and 10% perturbation in layer thickness, d) random layering of a binary medium with 5% perturbation in velocity and 10% perturbation in layer thickness. v_0 is the mean velocity, d_0 the mean layer thickness, v the velocity and z the position within the stack. 17

2.3 One realization of the 10% perturbed medium of Figure 2.2a. Comparison of the generalized effective medium theory and Kennett's method. a) Phase velocity v, b) attenuation α and c) seismogram. v_0 is the mean velocity, d_0 the mean layer thickness, t the travel time and v_{ray} is the ray theory velocity. 18

2.4 Similar to Figure 2.3 with the 10% perturbation of Figure 2.2a and the ensemble average of 20 realizations. 19

2.5 Similar to Figure 2.3 with the 10% perturbation of Figure 2.2a and the windowed arrival (25 time samples) of one realization. Note that the time scale is different from that in Figure 2.3 and 2.4. 20

2.6 Similar to Figure 2.5 with the 20% perturbation of Figure 2.2b and the windowed arrival (83 time samples) of one realization. . 23

2.7 Single realization of the 10% perturbed medium on the left hand side and of the 20% perturbed medium on the right hand side. The dotted line has been computed with Kennett's method and the solid line with the DYCEM theory. The amplitudes have been normalized by the maximum amplitude of the individual traces. The numbers on the seismograms indicate the absolute amplitude relative to the incident wave. The input pulse is the delta function with $kd_0 = 2\pi$ maximum frequency. 24
2.8 Similar to Figure 2.4 with the periodically layered binary medium of Figure 2.2c and the ensemble average of 20 realizations. The velocity ratio of type 2 to type 1 medium is 3/2 and the velocity and layer thickness are perturbed by 5% and 10%, respectively. 26
2.9 Similar to Figure 2.8 with the randomly layered binary medium of Figure 2.2d and the windowed arrival (66 time samples)of one realization. 27

3.1 A single inclusion with radius R at z=0 in a spherical coordinate system (r,θ,ϕ). 34
3.2 Schematic illustration of an incident plane wave U_{m0} and the transmitted plane wave U_m through a layer of thickness L with randomly distributed inclusions. 36
3.3 Self-consistent calculations of phase velocity and attenuation as a function of normalized frequency for Model 1 with 10% inclusions having radius R_1. v_m is the phase velocity, v_{m0} the matrix velocity and α_m the attenuation, where the index m is either the P-wave or the S-wave. The results for the P-wave are on the left hand side and for the S-wave on the right hand side. 49
3.4 Similar to Figure 3.3: Model 1 with 40% inclusions with radius R_1. 50
3.5 Seismograms for Model 1 with $L = 50\ R_1$ propagation distance for different inclusion concentrations using the self-consistent method. t is the travel time, L the propagation distance, v_{p0} the P-wave velocity and v_{s0} the S-wave velocity of the matrix. The input pulse is a delta function with $k_pR_1 = 20$ maximum frequency. . 51
3.6 Similar to Figure 3.5 for $L = 5000\ R_1$ propagation distance. . . 52
3.7 Log-normal distribution of the inclusion radius R with the mean radius R_{mean} and the standard deviation σ_R. 55
3.8 Similar to the self-consistent calculations in Figure 3.3 for Model 1 with 40% inclusions and the log-normal radius distributions in Figure 3.7. 56
3.9 Seismograms for Model 1 with $L = 5000\ R_{mean}$ propagation distance for 40% inclusions and the log-normal radius distributions in Figure 3.7 using the self-consistent method. 57

3.10 Similar to Figure 3.3 for Model 2 with 10% inclusions having radius R_1=1 mm and different viscosities η using the self-consistent method. 58
3.11 Similar to Figure 3.10 for Model 2 with 40% inclusions. 59
3.12 Similar to Figure 3.5 for Model 2 with R_1 = 1 mm inclusion radius and L = 50 R_1 propagation distance. 60
3.13 Similar to Figure 3.6 for Model 2 with R_1 = 1 mm inclusion radius and L = 5000 R_1 propagation distance. 61

4.1 Schematic outline of the theory. Step A: Calculation of the uncracked matrix. Step B: Introducing grain boundaries and cracks into the matrix. Step C: Introducing pores and porefluids. . . . 68
4.2 Interval measurements of porosity, pore water saturation, bulk density, P-velocity and S-velocity. The lithological identifications were obtained from Geslin et al. (1994). 72
4.3 Comparison of measured VSP-velocities and calculated velocities. 74
4.4 Velocities of the uncracked matrix and calculated crack densities, crack water saturations and effective matrix velocities. 76
4.5 Poisson ratio of the uncracked and cracked matrix. 77

5.1 Velocity of air-water mixtures calculated with Wood's equation. Small amounts of air have a strong effect and the velocity can be smaller than the velocity of each individual constituent. 88
5.2 Example of seismic waves transmitted through a partially water saturated single fracture with 0.5 mm aperture. The ambient pressure inside the fracture is 230 kPa and the velocity and density of the formation are 3860 m/s and 2450 kg/m^3, respectively. These values are equal to the top receiver of the monitor survey (Figure 5.4). The solid lines and boxes show the time window, which was used to compute the spectra. a) shows the seismogram, b) the modulus changes and c) the phase changes for different air concentrations. 90
5.3 Geometry of the shallow wells at the Conoco borehole test facility. GW6 was drilled at GW3 with a slant well drilling rig at 30° from the vertical and penetrates the fracture at 25 m depth. 97
5.4 Monitor survey: Measured data at receiver 1 at different times during air injection. Similar to Figure 5.2, the solid lines and boxes show the time window, which was used to compute the spectra. a) shows the seismogram, b) the modulus changes and c) the phase changes at different times. 99

5.5 Monitor survey: Inversion results for the top receiver at 21.7 m depth. The error bars indicate the 95% confidence interval determined by the t-test. The last figure on the right hand side shows the observed changes (dotted line) and the unexplained part of those changes by the single fracture model (solid line, equation (5.10)). Reliable aperture estimates can only be obtained if the velocity drops below 100 m/s and are marked by solid boxes. The mean aperture for the first receiver is 0.49 mm (95% confidence interval: 0.35 mm-0.66 mm) 102

5.6 Similar to Figure 5.5. Monitor survey: Inversion results for receiver 2 at 22.7 m depth. The mean aperture for the second receiver is 0.90 mm (95% confidence interval: 0.62 mm-1.07 mm) 103

5.7 Monitor survey: The dotted lines are the measured traces at receiver 1 and 2 during the experiment. The fitted traces are overlain on top of the data and are calculated using the parameters in Figure 5.5 and 5.6. 104

5.8 Seismograms of receiver 4: a) Seismogram before the air injection. Traces have been individually normalized by their maximum. Crosses denote the arrival time of the direct wave. b) Seismogram after the air injection. Traces have been individually normalized by the maximum before the air injection. c) Seismogram after the air injection. Traces have been individually normalized by their maximum. 106

5.9 Average parameter estimates derived from the individual inversions of receiver 3, 4 and 5. The error bars denote one standard error derived by the weighted least square method. Reliable aperture estimates can only be obtained if the velocity drops below 100 m/s and are marked by solid boxes. 107

5.10 Example of an inversion: Student's t for different pairs of air concentration and aperture at the first receiver during the monitor survey at the end of the experiment with four stacked windows. The minimum objective function is at 66.7% air concentration and 0.33 mm aperture. The critical t-value for this example is t = 2.26 for the 95% confidence level and the shaded area denotes the 95% confidence interval. If Student's t exceeds 9.99, no values are plotted. 114

A.1 Comparison between Beryman's exact theory and Gassmann's equations. K is the bulk modulus, μ the shear modulus, Δ the relative difference, ν the Poisson's ratio, ρ the density and ϕ the porosity. $K_0/K_f = 5$ and $\nu_0 = 0.1$. 128

A.2 Similar to Figure A.1: $K_0/K_f = 5$ and $\nu_0 = 0.25$ 129

A.3 Similar to Figure A.1: $K_0/K_f = 5$ and $\nu_0 = 0.4$ 130

List of Tables

3.1 Material properties of the matrix and inclusions: P-wave velocity v_p, S-wave velocity v_s, density ρ and dynamic viscosity η. 47

4.1 Seismic velocity, Poisson ratio and density of the important minerals in UZ16. 71

4.2 Average volume concentrations and one standard deviation of the different minerals in UZ 16. 73

5.1 Parameters for Figure 5.2. c is the air concentration, v the velocity and ρ the bulk density inside the fracture, dt the travel time delay of the first transmitted wave, λ the seismic wavelength, d = 0.5 mm the fracture aperture and f the frequency. The velocity v has been calculated with Wood's equation and 230 kPa ambient pressure. To calculate the reflection coefficient R between formation and fracture, we have used the same formation properties (velocity=3860 m/s and density=2450 kg/m^3) as in Figure 5.4. 91

5.2 Velocity and density in the Fort Riley formation derived from the crosswell survey between GW1 and GW3. Depth is relative to the surface at the location of the fracture. 96

Acknowledgements

This thesis would not have been possible without the guidance and encouragement of my adviser Lane Johnson. I would like to thank him for his support and his original ideas, which made my thesis what it is today. His great personality, his immense knowledge and his enthusiasm for science were a constant inspiration to explore unknown territory and to solve longstanding physical problems.

Ernie Majer deserves my gratitude for providing me with the financial support needed to work on the basic physics of wave propagation. I also enjoyed working with him in various field projects, where he helped to improve the data acquisition many times.

Many thanks to Patty Seifert for providing me with many puzzling laboratory measurements and insightful discussions. Her strong will for finding physically reasonable answers and her integrity were a constant encouragement for me.

Raymond Jeanloz and Jamie Rector deserve my gratitude for their helpful insight in the preparation of my thesis. My thanks also to Valerie Korneev and Lane Johnson for their excellent work on scattering of elastic waves by inclusions. Without them, my work would still be one-dimensional. My appreciation also to the people in the CCS group at the Berkeley National Laboratory for their help over the years. In particular, I would like to thank Ramsey Haught, Don Lippert, Tom Daley and Ken Williams for introducing me to Ponca City and the freeway culture of the central valley. Their company made it all worthwhile.

I would like to thank Stefan Finsterle, April James, Henk Keers, Chaincy Kuo, Julie Najita, Paul Parker and Patty Seifert for keeping up the culture of taking lunch breaks, which gave me sometimes a much needed break. Many thanks go to all the people, who kept in touch and spent time with me. Last but not least, my appreciation to my parents and my siblings for being there for me.

Chapter 1

Introduction

Over the last three decades enormous strides have been made in understanding the connections between physical properties of rocks and elastic wave propagation. Scientists have discovered a variety of relations, such as wave velocity versus porosity, velocity versus fluid saturation and lithology. Unfortunately, most of the theories developed by the oil industry provide unreliable results at shallow depths. Small effective pressures, poor consolidation and inhomogeneities have been pointed out to be responsible for the discrepancy.

The first major breakthrough in predicting the elastic moduli of porous media at low frequencies was achieved by Gassmann (1951). Gassmann's equations relate elastic moduli of fluid saturated rocks to the properties of the dry frame and the fluid and are still widely used, but they provide little insight into the physics of wave propagation. However, Gassmann's equations are consistent with the low frequency limit of Biot's theory (Biot, 1956a) and a special case of Berryman's theory (Berryman, 1980a), both discussed below.

Biot developed a theory of wave propagation in fluid saturated porous media that focuses on macroscopic fluid flow. Biot's theory (1956a; 1956b) shows that acoustic waves create relative motion between the fluid and the solid frame due to inertial effects. As the matrix is accelerated, the fluid lags behind, resulting in viscous dissipation of acoustic energy. At seismic frequencies, the predicted attenuation is usually too small compared to measurements. Many rocks show much more dispersion and attenuation than predicted by Biot's theory.

Another fluid flow mechanism, often called "local-flow" or "squirt-flow", is based upon microscopic fluid motion. The pore space of a rock is generally very heterogeneous, some regions being very compliant while others are very stiff. This can result in fluid being squeezed out of grain contacts into nearby pores, or squeezed between adjacent cracks having different orientations with respect to a passing stress wave. While most of local fluid flow models can be fit to experimental data, they have not the predictive power of Gassmann's or Biot's theory, because they are all highly dependent on details of the microstructure that cannot yet be adequately quantified.

A different approach to study porous media is to calculate elastic scattering from pores and grains. Elastic scattering occurs whenever velocity or density heterogeneities are present. Although the scattered energy is not absorbed by the rock as heat, it results in energy loss to the primary pulse. In one-dimensional stratified media, scattering has been studied extensively and is regarded as the

main attenuation mechanism for acoustic waves. A three-dimensional scattering approach to calculate the elastic properties of spherical inclusions in the low frequency limit was presented by Kuster and Toksöz (1974). Berryman (1980a) modified their approach and obtained the self-consistent theory for spherical inclusions, which is consistent with Gassmann's equations if Gassmann's assumption that the saturated and dry shear modulus are the same is fulfilled (Appendix A). However, Berryman's theory is only valid in the low frequency limit without considering scattering attenuation. Although Berryman's theory provides more insight into the physics of elastic wave propagation, it has rarely been used by other authors. Many critics believe that a major flaw of the self-consistent theory is its prediction of a threshold of rigidity at a finite concentration of fluid in a solid matrix.

In Chapter 2, I develop a self-consistent theory for one-dimensional stratified media to demonstrate the validity and limitations of self-consistent theories. The theory, called the DYnamic Composite Elastic Medium theory (DYCEM), is based upon the scattering function of the individual layers in a stack of layers. The theory is applied to perturbed and binary media and the results are compared with the exact propagator method by Kennett (1983).

Chapter 3 explores the generalized self-consistent theory used in Chapter 2 for three-dimensional inclusions. First, the effect of one single inclusion upon an incident plane wave is discussed. Then, the obtained scattering function is

incorporated into the self-consistent theory to compute the elastic properties of many three-dimensional inclusions at any frequency. For the special case of spherical inclusions, I present spectra and waveforms of materials with solid and liquid inclusions in a solid matrix.

The case study of seismic rock properties of highly porous tuffs in the Yucca Mountain region is presented in Chapter 4. The Yucca Mountain region in the southwestern part of Nevada is currently being evaluated as a potential site for a nuclear waste repository. Several seismic reflection surveys have been conducted in the past, which provided small penetration depths with discontinuous layers. I use log and VSP data to derive the elastic properties of the matrix material. Berryman' theory is used to describe the pores and O'Connell and Budiansky's theory (1974) the grain contacts and microcracks.

Chapter 5 describes the importance of *a priori* knowledge and the large impact of volatiles on seismic waves. Crosswell surveys before and after an air injection experiment into a local fracture zone are analyzed. Travel times show no significant change due to the experiment, but the amplitudes decrease by orders of magnitudes. I use a single vertical fluid layer with variable air concentration to simulate the experiment and to invert for fracture apertures.

Chapter 2

Dynamic composite elastic medium theory. Part I. One-dimensional media

2.1 Abstract

Wave propagation in stratified media may be described by scattering theory, effective medium theory or ray theory, depending upon the frequency range. We present a dynamic composite elastic medium (DYCEM) theory which describes wave propagation at all frequencies. In the first part of the series we consider randomly layered one-dimensional media and in the second part media with three-dimensional inclusions. Non-self-consistent and self-consistent methods using the scattering functions of the individual layers are formulated which allow the calculation of phase velocity, attenuation and waveforms. In the low frequency limit only the self-consistent method agrees with the Reuss average and in the high frequency limit it yields the correct ray theory average velocity. The comparison with complete numerical solutions shows that our theory predicts the coherent wave through randomly layered media. Hence, the dynamic

composite elastic medium theory can be used to compute frequency dependent elastic properties of randomly layered media without calculating the complete wave propagation solution.

2.2 Introduction

An almost universal feature of materials encountered in the earth is that they tend to be heterogeneous on many scales. These heterogeneities include variation in mineral composition, grain size, porosity, pore size, pore fluid properties, and conditions of temperature and stress. In the past fifty years the characterization of such inhomogeneities on different scales and their influence on wave propagation have been studied extensively. The first major breakthrough in predicting the elastic moduli of porous media was achieved by Gassmann (1951). Biot (1956a, 1956b) developed independently a theory to predict velocity and attenuation in porous media by taking fluid flow within the pores into account. Biot's theory was later successfully modified by Dvorkin et al. (1995) to account for squirt flow between soft and stiff pores.

In this study we consider a different approach to the study of heterogeneous media that involves scattering. One of the best known works using this approach is the theory for a stratified medium by O'Doherty and Anstey (1971), who predicted the attenuation and time delay of a pulse through a randomly layered medium. There was some controversy about the derivation of their theory, which

led to a number of modified theories (e.g., Schoenberger and Levin, 1974; Banik et al., 1985a; Banik et al., 1985b; Burridge et al., 1988; Shapiro et al., 1994). The properties of these theories for one-dimensional media are relatively easy to check because numerical methods are available for calculating complete solutions for layered media.

A truly three-dimensional scattering approach to calculate the elastic properties of spherical inclusions in the low frequency limit was first presented by Kuster and Toksöz (1974). Berryman (1980a) showed that their theory is not self-consistent and therefore not valid for large inclusion concentrations. Berryman modified Kuster and Toksöz's theory and obtained a self-consistent theory for spherical inclusions and elliptical inclusions in the low frequency limit (Berryman, 1980a; Berryman, 1980b). Berryman's self-consistent theory is only valid in the low frequency limit and does not consider attenuation due to scattering. Using a self-consistent dynamic composite elastic medium (DYCEM) theory, we have been able to compute attenuation and phase velocity of a medium with spherical inclusions at all frequencies (chapter 3). However, controversy still exists about the validity of self-consistent theories, and, in the case of three-dimensional problems, complete numerical solutions are not available to help resolve the controversy. Hence, in this paper we formulate a dynamic composite elastic medium theory for the one-dimensional problem analogous to the three-dimensional problem. The method is applied to numerical simulations of

perturbed and binary media and compared with a complete numerical solution to illustrate the validity, interpretation and limitations of the dynamic composite elastic medium theory. Having demonstrated the validity of this approach for one-dimensional media, the method is extended to the case of three-dimensional media in a companion paper.

2.3 Dynamic composite elastic medium theory

In order to calculate the first arrival of seismic waves through a stack of layers, we perform the following thought experiment. First, we assume a homogeneous medium of thickness L, velocity v_0 and density ρ_0. For a normally incident plane wave, the resulting wave field at distance L is

$$U = U_0 e^{-ik_0 L}, \tag{2.1}$$

where k_0 is the complex wavenumber and U and U_0 are the spectra of the wave field at distance L and of the incident wave, respectively. Equation (2.1) can also be written in terms of the attenuation α_0 and phase velocity v_0

$$U = U_0 e^{-\alpha_0 L} e^{-i\frac{\omega}{v_0}L}, \tag{2.2}$$

where ω is the angular frequency. Comparing equation (2.1) and (2.2) we obtain

$$\alpha_0 \;=\; -\Im\{k_0\}, \qquad v_0 = \Re\{\frac{\omega}{k_0}\}, \tag{2.3}$$

where the symbol $\Im$ represents the imaginary part and $\Re$ the real part.

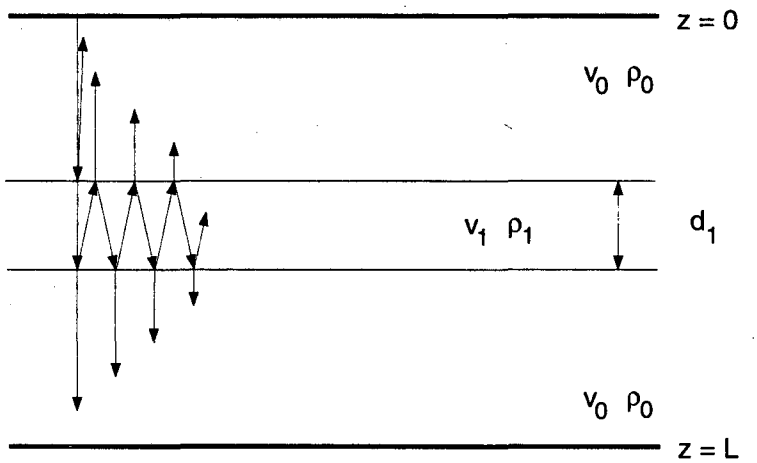

Figure 2.1: Schematic illustration of a transmitted wave through a homogeneous background with velocity v_0 and density ρ_0, and one layer with velocity v_1, density ρ_1 and thickness d_1. The transmitted wave and all reverberations within one layer are considered in the dynamic composite elastic medium theory.

2.3.1 Non-self-consistent theory

Next we introduce one layer with thickness d_1, velocity v_1 and density ρ_1 into the previously homogeneous medium (Figure 2.1). The wave field U_1 at distance L becomes

$$U_1 = U_0 A_{10} e^{-ik_0 L} \tag{2.4}$$

with

$$A_{10} = \frac{1 - R_{10}^2}{1 - R_{10}^2 e^{-i2k_1 d_1}} e^{-i(k_1 - k_0)d_1}$$
$$R_{10} = \frac{\rho_1 v_1 - \rho_0 v_0}{\rho_1 v_1 + \rho_0 v_0},$$

where A_{10} is the scattering function of the new layer for a normally incident

wave and R_{10} is the reflection coefficient between the background and the new layer (Aki and Richards, 1980). The wave field U_1 can also be expressed in terms of the non-self-consistent wavenumber k_{NS}

$$U_1 = U_0 e^{-ik_{NS}L} \tag{2.5}$$

and with equation (2.4), we obtain

$$k_{NS} = k_0 + \frac{i}{L} \ln A_{10}. \tag{2.6}$$

Equation (2.6) is exact since it takes into account all the reverberations within the new layer. Next we randomly place more layers into the background medium and assume that the distances between the layers are much larger than the layer thicknesses. Hence, the first arrival shows no considerable contribution of reverberations between the different layers. Using this approximation, equation (2.4) for N_1 layers becomes

$$U_{N_1} = U_0 \prod_{n=1}^{N_1} A_{n0} e^{-ik_0 L} \tag{2.7}$$

and equation (2.6) becomes

$$k_{NS} = k_0 + \frac{i}{L} \sum_{n=1}^{N_1} \ln A_{n0} \tag{2.8}$$

with

$$A_{n0} = \frac{1 - R_{n0}^2}{1 - R_{n0}^2 e^{-i2k_n d_n}} e^{-i(k_n - k_0)d_n}$$

$$R_{n0} = \frac{\rho_n v_n - \rho_0 v_0}{\rho_n v_n + \rho_0 v_0}.$$

Including the background layers, N is the total number of layers in the stack and the scattering functions A_{n0} for n=N_1+1,...,N are unity. Hence, equation (2.8) is equivalent to

$$k_{NS} = k_0 + \frac{i}{L}\sum_{n=1}^{N} \ln A_{n0} \tag{2.9}$$

The non-self-consistent wavenumber k_{NS} in equation (2.9) is dependent upon the choice of the matrix wavenumber k_0. If the background and the layers are interchanged, the resulting non-self-consistent wavenumber will generally be different. Hence, equation (2.9) has to be modified in a self-consistent way to eliminate the arbitrary choice of the matrix. Nevertheless, equation (2.9) is the resulting wavenumber for multiple forward scattering, if the interactions between the layers are being ignored.

2.3.2 Self-consistent theory

With an increasing number of layers, reverberations between the layers become important and the non-self-consistent theory is no longer valid. In this case, a self-consistent formulation is needed (e.g., Berryman, 1980a). To accomplish this task, we have to replace the true background medium by an effective medium. In this way, all the layers, including the true background layers, act as scatterers relative to the effective medium and the arbitrary choice of the matrix has been eliminated. The properties of the effective medium are determined by all layers in the stack, but multiple scattering is limited to two neighboring

layers and the reflection coefficient is computed relative to the effective medium properties. To compute the self-consistent wavenumber k_S, we simply replace the background by the effective medium and equation (2.9) becomes

$$k_S = k_S + \frac{i}{L}\sum_{n=1}^{N} \ln A_{nS} \tag{2.10}$$

or

$$\frac{i}{L}\sum_{n=1}^{N} \ln A_{nS} = 0, \tag{2.11}$$

with

$$\begin{aligned} A_{nS} &= \frac{1 - R_{nS}^2}{1 - R_{nS}^2 e^{-i2k_n d_n}} e^{-i(k_n - k_S)d_n} \\ R_{nS} &= \frac{\rho_n v_n - \rho_S v_S}{\rho_n v_n + \rho_S v_S} \\ \rho_S &= \frac{1}{L}\sum_{n=1}^{N} \rho_n d_n, \end{aligned}$$

where A_{nS}, v_S and ρ_S are the self-consistent scattering function, phase velocity and density, respectively. Since the wavenumbers are complex, equation (2.11) describes a set of two equations, which must be solved for the real and the imaginary parts of k_S at each frequency. In general, these equations can not be solved analytically. From a number of numerical methods to solve nonlinear equations, we found Muller's numerical method (Press et al., 1992) the fastest and most stable.

2.3.3 Low and high frequency approximations

In order to compare the results of this study with other theories and to show the limitations of the dynamic composite elastic medium theory, it is helpful to determine the low and high frequency limits. At low frequencies the scattering function between layer n and m becomes

$$A_{nm} = \left[1 + \frac{1}{2}\frac{R_{nm}^2}{1-R_{nm}^2}(2k_n d_n)^2 + i\frac{2R_{nm}^2}{1-R_{nm}^2}k_n d_n\right]^{-1} e^{-i(k_n-k_m)d_n}. \tag{2.12}$$

With equation (2.9) and (2.12), the non-self-consistent wavenumber is therefore

$$k_{NS} = k_0 - \frac{i}{L}\sum_{n=1}^{N}\left[\frac{2R_{n0}^2}{1-R_{n0}^2}(k_n d_n)^2 + i\frac{2R_{n0}^2}{1-R_{n0}^2}k_n d_n + i(k_n - k_0)d_n\right] \tag{2.13}$$

and, in the limit of low frequencies, the non-self-consistent phase velocity becomes

$$\frac{1}{v_{NS}} = \frac{1}{L}\sum_{n=1}^{N}\frac{1+R_{n0}^2}{1-R_{n0}^2}\frac{d_n}{v_n}. \tag{2.14}$$

With equation (2.11) and (2.12) the self-consistent wavenumber is the solution of the equation

$$\frac{i}{L}\sum_{n=1}^{N}\left[\frac{2R_{nS}^2}{1-R_{nS}^2}(k_n d_n)^2 + i\frac{2R_{nS}^2}{1-R_{nS}^2}k_n d_n + i(k_n - k_S)d_n\right] = 0 \tag{2.15}$$

and in the limit of low frequencies the self-consistent phase velocity is

$$\frac{1}{v_S} = \left[\rho_S\frac{1}{L}\sum_{n=1}^{N}\frac{d_n}{\rho_n v_n^2}\right]^{\frac{1}{2}}. \tag{2.16}$$

Thus, in the low frequency limit, the self-consistent phase velocity (equation (2.16)) is equal to the correct Reuss average (Reuss, 1929), but the non-self-consistent phase velocity (equation (2.14)) is different.

At high frequencies, the scattering function between layer n and m becomes

$$A_{nm} = (1 - R_{nm}^2)e^{-i(k_n - k_m)d_n}. \tag{2.17}$$

With equation (2.9) and (2.17) the non-self-consistent wavenumber is

$$k_{NS} = k_0 + \frac{i}{L}\sum_{n=1}^{N}\left[\ln(1 - R_{n0}^2) - i(k_n - k_0)d_n\right] \tag{2.18}$$

and in the limit of high frequencies the non-self-consistent phase velocity is

$$\frac{1}{v_{NS}} = \frac{1}{L}\sum_{n=1}^{N}\frac{d_n}{v_n}. \tag{2.19}$$

With equation (2.11) and (2.17) the self-consistent wavenumber is obtained from

$$\frac{i}{L}\sum_{n=1}^{N}\left[\ln(1 - R_{nS}^2) - i(k_n - k_S)d_n\right] = 0 \tag{2.20}$$

and in the limit of high frequencies the self-consistent phase velocity is

$$\frac{1}{v_S} = \frac{1}{L}\sum_{n=1}^{N}\frac{d_n}{v_n}. \tag{2.21}$$

In the high frequency limit, both theories yield the correct ray theory phase velocity (equation (2.19) and (2.21)), but only the self-consistent phase velocity is correct for both frequency limits. The attenuation of both theories shows the ω^2 dependence of the Rayleigh scattering for stratified media (equation (2.13) and (2.15)). However, there exist no equivalent attenuation averages to compare with the low frequency attenuation limits. At high frequencies, the non-self-consistent approach yields the correct sum of all the transmission coefficients (equation (2.18)). The non-self-consistent attenuation is generally different and has to be inspected for each specific case (equation (2.20)).

2.4 Numerical simulations

For the following numerical simulations we have used the self-consistent theory only because its phase velocity is correct for both frequency limits. We have used Kennett's propagator method (Kennett, 1983) to calculate the exact seismogram of waves propagating through a stack of layers at normal incidence. Kennett's method requires a specific realization of the medium, whereas the dynamic composite elastic medium theory does not require information about the position of the layers within the stack. However, our theory assumes evenly distributed but uncorrelated layers in the stack. With Kennett's method this can be simulated by averaging different realizations, i.e., by using ensemble averages. To compute the attenuation and phase velocity with Kennett's method we have computed the complex spectrum of the seismogram

$$U = |U|\, e^{i\phi}, \qquad \phi = \arctan \frac{\Im\{U\}}{\Re\{U\}} \tag{2.22}$$

where |U| is the modulus and ϕ the phase. Comparing equation (2.22) with equation (2.2), the attenuation α and the phase velocity v are

$$\alpha = -\frac{1}{L} \ln \left| \frac{U}{U_0} \right|, \qquad v = -\frac{\omega L}{\phi - \phi_0}. \tag{2.23}$$

The computation of the phase velocity v requires continuous phase functions ϕ and ϕ_0, whereas the phase ϕ in equation (2.22) is defined only in the interval [-$\pi/2$, $\pi/2$]. Thus, the phase ϕ has to be unwrapped, which can cause non-uniqueness. Nevertheless, we found the phase velocity to be a useful tool for

comparing numerical simulations.

2.4.1 Perturbed media

There exist a number of studies concerning wave propagation in layered perturbed media (e.g., Banik et al., 1985b; White et al., 1990; Goff et al., 1994; Shapiro et al., 1994). Most of these studies characterize the medium with statistical parameters. In this study, we are focusing on the microscopic scale, i.e., the medium is perturbed and the layers are truly random. One can also think of homogeneous mineral layers, which have slightly different physical properties. Burridge et al. (1988) have shown that the propagation distance has to be large to obtain reliable estimates of the scattering effects. We have found that this condition is fulfilled if the propagation distance is four times larger than the maximum wavelength. In terms of the normalized frequency kd_0, the condition is therefore fulfilled if $kd_0 > 2\pi \cdot 4/N$, where k is the wavenumber, d_0 the mean layer thickness and N the number of layers in the stack. Once this condition is fulfilled, the attenuation coefficient will remain unchanged if more layers are added to the stack. Thus, the attenuation coefficient is equal to the inverse of the localization length, which has been frequently used in radiophysics and more recently in elastic wave propagation.

For all the following simulations we chose the unit impulse function as the incident wave. For our first simulation, we chose 500 layers with constant density.

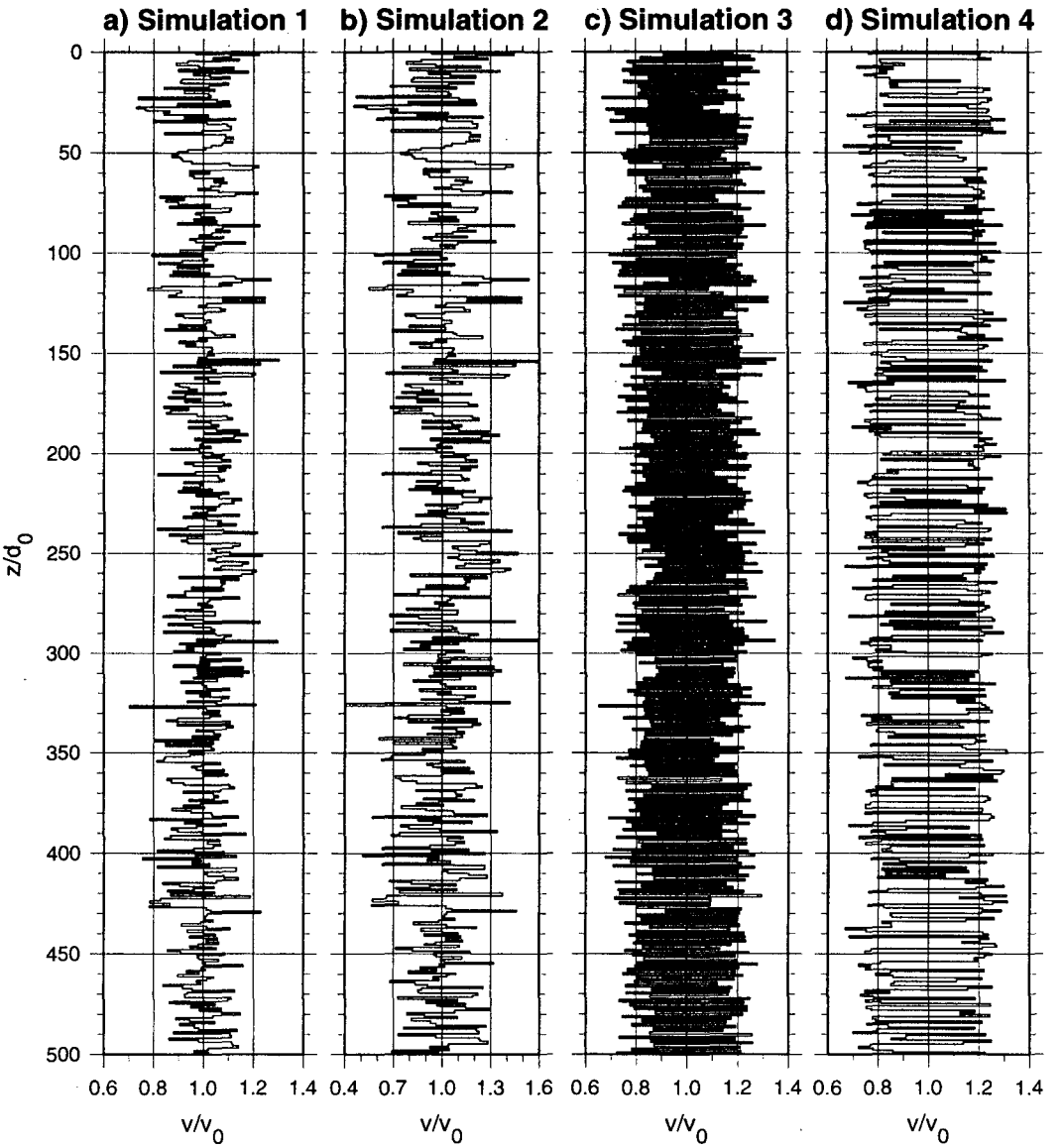

Figure 2.2: Velocity profiles for the numerical simulations: a) 10% perturbation in velocity and layer thickness, b) 20% perturbation in velocity and layer thickness, c) periodic layering of a binary medium with 5% perturbation in velocity and 10% perturbation in layer thickness, d) random layering of a binary medium with 5% perturbation in velocity and 10% perturbation in layer thickness. v_0 is the mean velocity, d_0 the mean layer thickness, v the velocity and z the position within the stack.

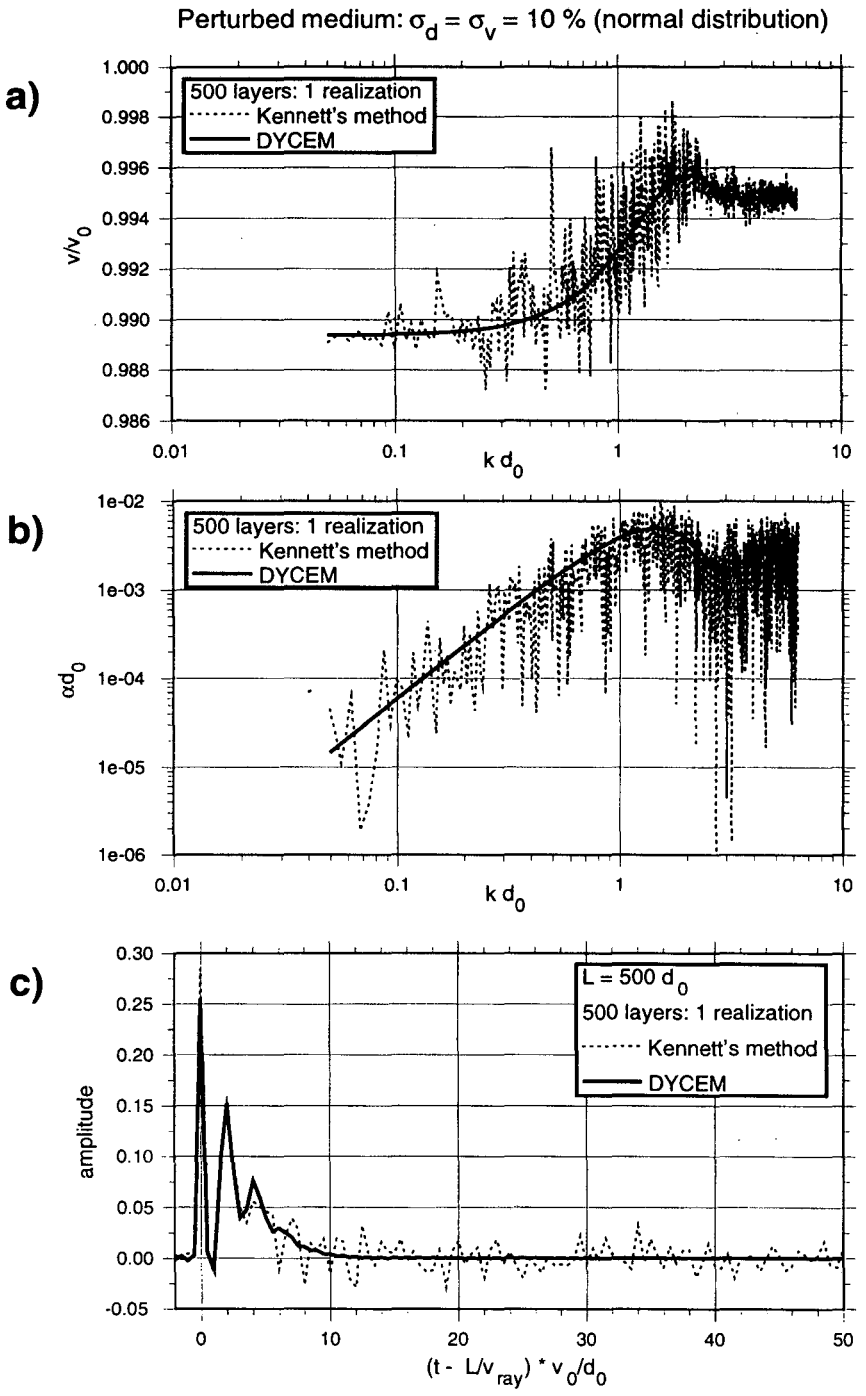

Figure 2.3: One realization of the 10% perturbed medium of Figure 2.2a. Comparison of the generalized effective medium theory and Kennett's method. a) Phase velocity v, b) attenuation α and c) seismogram. v_0 is the mean velocity, d_0 the mean layer thickness, t the travel time and v_{ray} is the ray theory velocity.

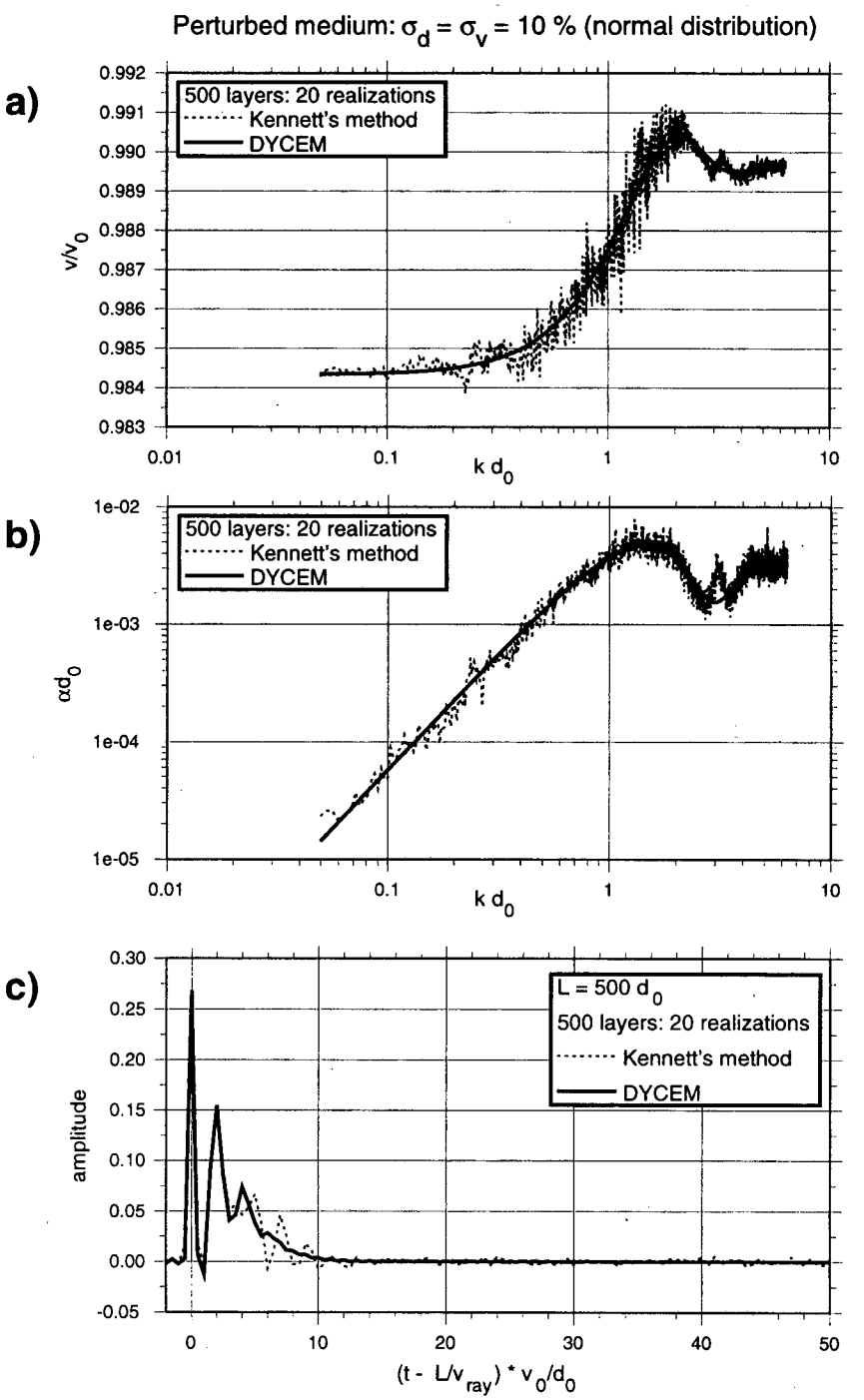

Figure 2.4: Similar to Figure 2.3 with the 10% perturbation of Figure 2.2a and the ensemble average of 20 realizations.

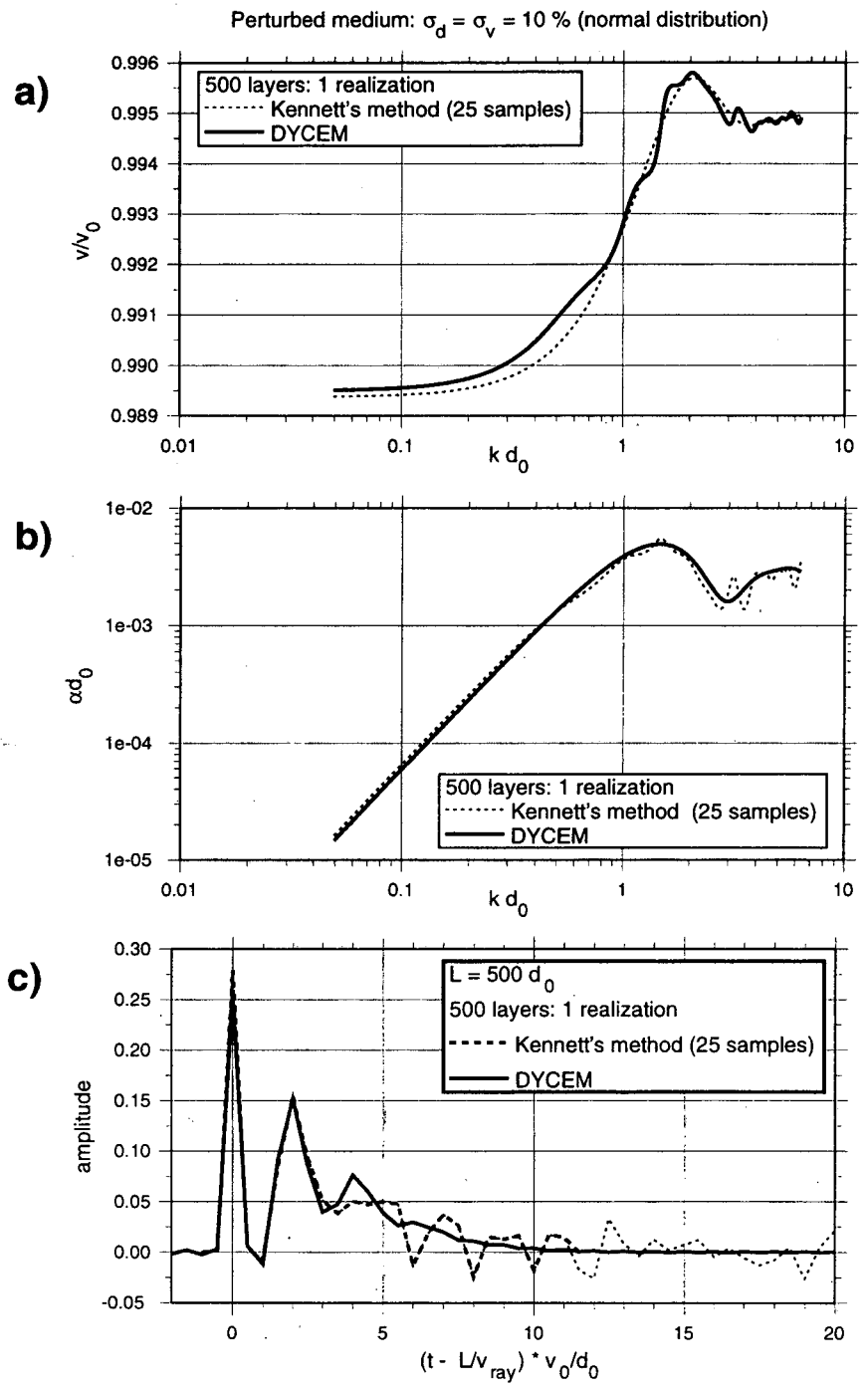

Figure 2.5: Similar to Figure 2.3 with the 10% perturbation of Figure 2.2a and the windowed arrival (25 time samples) of one realization. Note that the time scale is different from that in Figure 2.3 and 2.4.

The velocity and layer thickness had a normal distribution with 10% standard deviation (Figure 2.2a). With the restriction above, the attenuation and phase velocity are significant if $kd_0 > 0.05$. Figure 2.3 shows the phase velocity, attenuation and seismogram of one single realization. The normalized attenuation αd_0 shows that the perturbed medium acts as a low pass filter due to scattering attenuation. As expected, Kennett's method shows interference effects, which are typical for this single realization. The dynamic composite elastic medium (DYCEM) theory shows a smooth spectrum, but predicts the average velocity and attenuation of Kennett's method at all frequencies. The time axis in Figure 2.2c has been normalized by the ray velocity. Hence, the first arrival at time zero is the high frequency wave traveling with the ray theory velocity. After performing an ensemble average with 20 different realizations, most of the interferences are suppressed and Kennett's method and the dynamic composite elastic medium theory agree well at all frequencies (Figure 2.4). In the process of ensemble averaging, the incoherent signals have been suppressed and only the coherent signal remains. Hence, the dynamic composite elastic medium theory has to be interpreted as the coherent part of the seismogram at all frequencies. Even for one single realization, the dynamic composite elastic medium theory describes the first few arrivals reasonably well (Figure 2.3c). This feature agrees with Burridge et al. (1988), who have shown that the coherent field in the seismogram can be described without ensemble averaging. One can therefore choose

a time window and apply it to the seismogram obtained by Kennett's method with only one realization and compare it with our theory. We have chosen the position and length of the time window according to the non-zero part of the dynamic composite elastic medium theory seismogram (Figure 2.3c). The results in Figure 2.5 show good agreement between our theory and Kennett's method with only one realization.

For the second numerical simulation we chose 500 layers with constant density and increased the perturbation of velocity and layer thickness to 20% (Figure 2.2b). For the computation with Kennett's method we used a single realization and the time window in the same manner as in the previous example. The results in Figure 2.6 show good agreement for this strongly perturbed medium.

So far we have kept the number of layers constant, because the phase velocity and attenuation remain constant and are independent upon the propagation distance if $kd_0 > 2\pi \cdot 4/N$. However, the scattering effects can also be analyzed with the seismogram as a function of propagation distance. Figure 2.7 shows the normalized seismograms for the 10% and 20% perturbed media. The time axis has been normalized by the ray velocity and the first arrival at time zero is the high frequency wave traveling with the ray theory velocity. In the 10% perturbed medium, this wave can be observed at every propagation distance, but in the 20% perturbed medium, the wave is totally attenuated after about 600 layers. In both examples the low frequency wave with the Reuss average

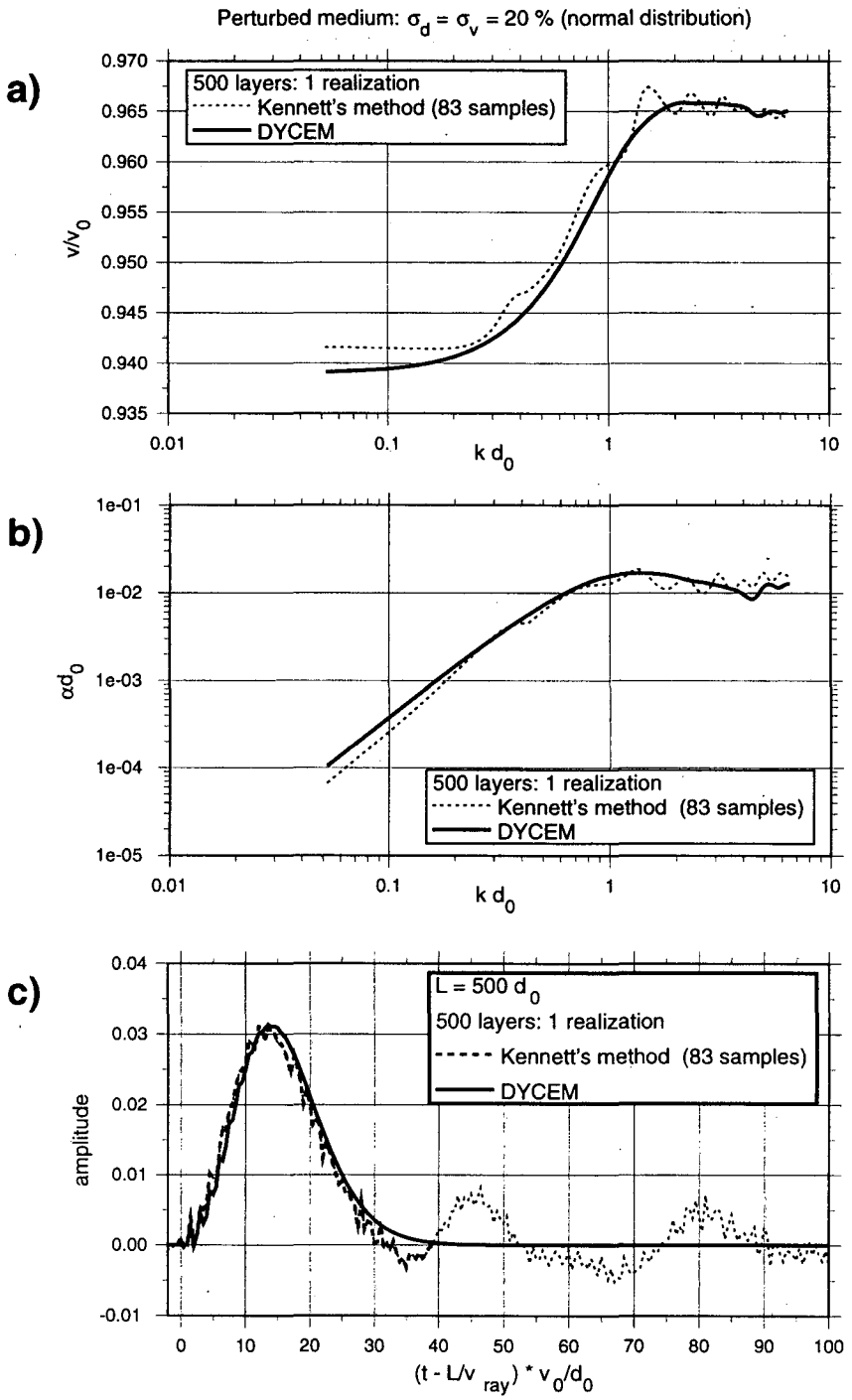

Figure 2.6: Similar to Figure 2.5 with the 20% perturbation of Figure 2.2b and the windowed arrival (83 time samples) of one realization.

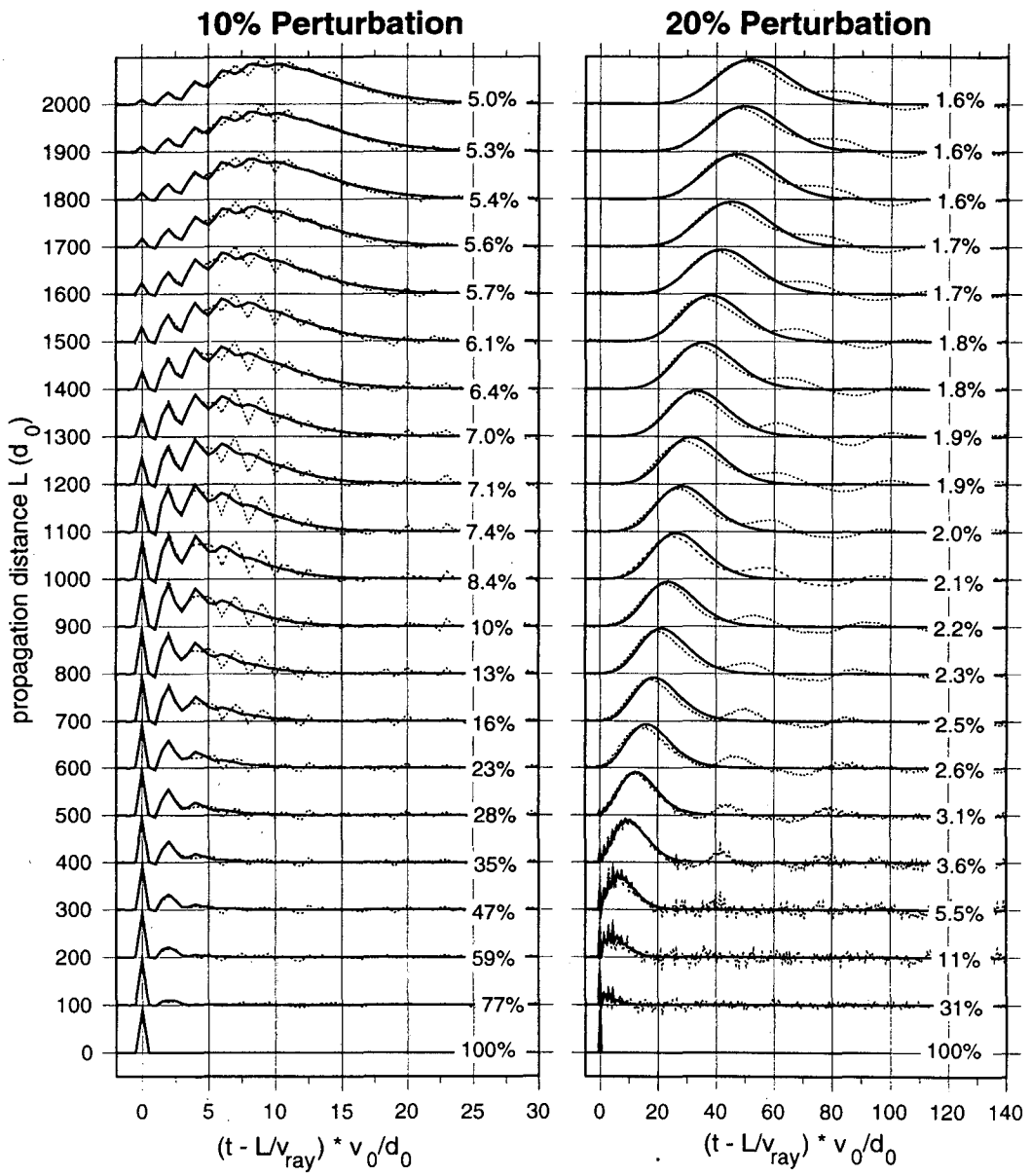

Figure 2.7: Single realization of the 10% perturbed medium on the left hand side and of the 20% perturbed medium on the right hand side. The dotted line has been computed with Kennett's method and the solid line with the DYCEM theory. The amplitudes have been normalized by the maximum amplitude of the individual traces. The numbers on the seismograms indicate the absolute amplitude relative to the incident wave. The input pulse is the delta function with $kd_0 = 2\pi$ maximum frequency.

velocity becomes dominant with increasing propagation distance. The absolute amplitudes however are much smaller for these waves, but they do not decay as rapidly as for the wave with the ray theory velocity. Figure 2.7 shows generally good agreement of the coherent wave between Kennett's method and our theory.

2.4.2 Binary media

In practical applications stratified media often consist of materials with distinct but different physical properties. For instance, in many sedimentary basins there exists periodic layering of sand and shale. In the following we simulate a stratified binary medium, i.e., a layer is either of type 1 or type 2. Binary sediments have been studied by a number of authors (e.g., Richards and Menke, 1983; Frazer, 1994; Marion et al., 1994). In particular the study by Marion et al. (1994) is relevant to our work, since it considers experimental data of velocity dispersion over a wide frequency range in binary one-dimensional media. In the third and fourth simulation the velocity ratio of type 2 to type 1 material was 3/2. The layer thickness and the velocity were normally distributed with standard deviations of 10% and 5%, respectively.

For our third simulation we chose a periodic layering of two materials, i.e., each type 1 layer lies always between type 2 layers (Figure 2.2c). Figure 2.8 shows the results of this calculation for 500 layers and an ensemble average of 20 realizations. The unwrapping of the phase with Kennett's method was

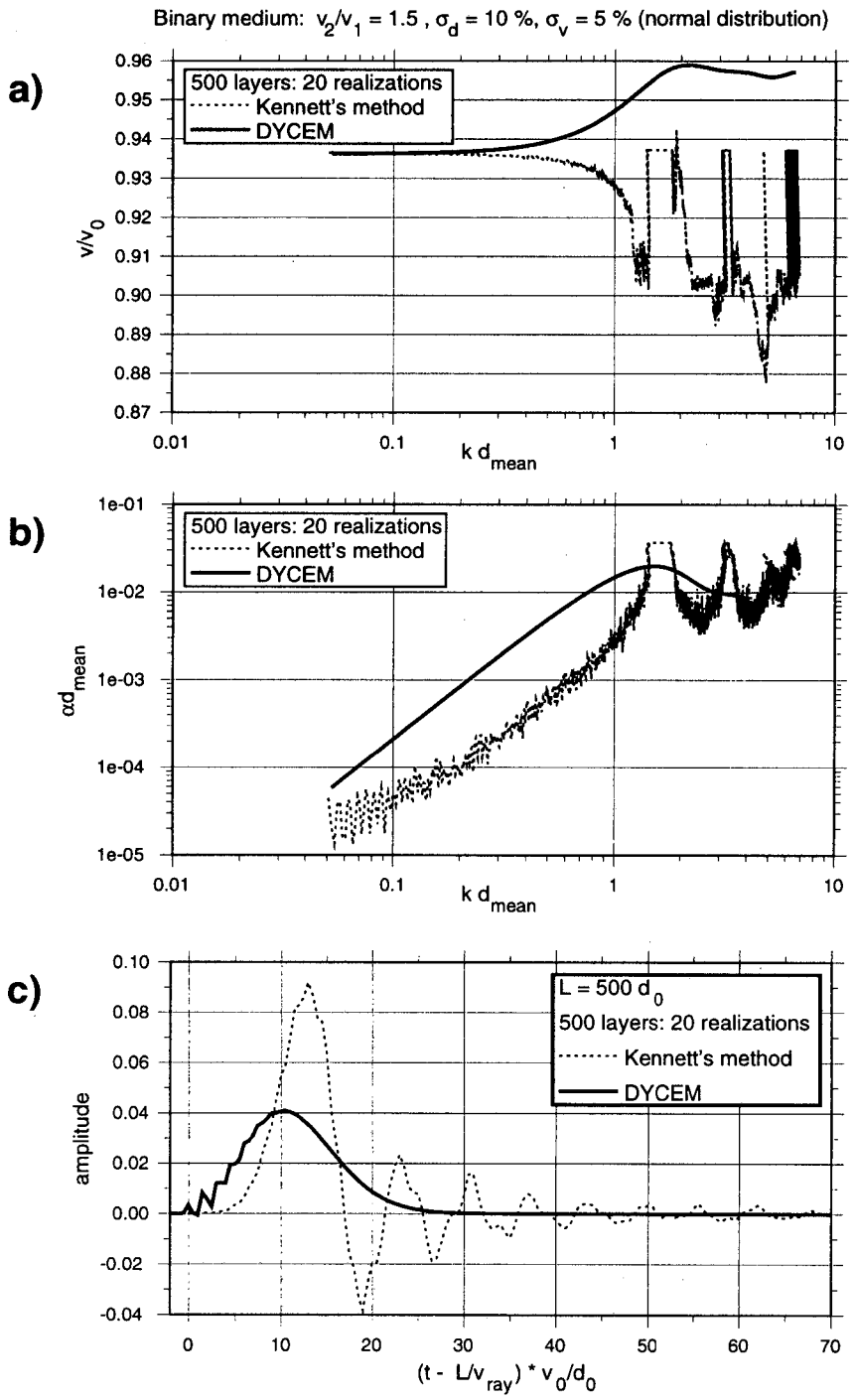

Figure 2.8: Similar to Figure 2.4 with the periodically layered binary medium of Figure 2.2c and the ensemble average of 20 realizations. The velocity ratio of type 2 to type 1 medium is 3/2 and the velocity and layer thickness are perturbed by 5% and 10%, respectively.

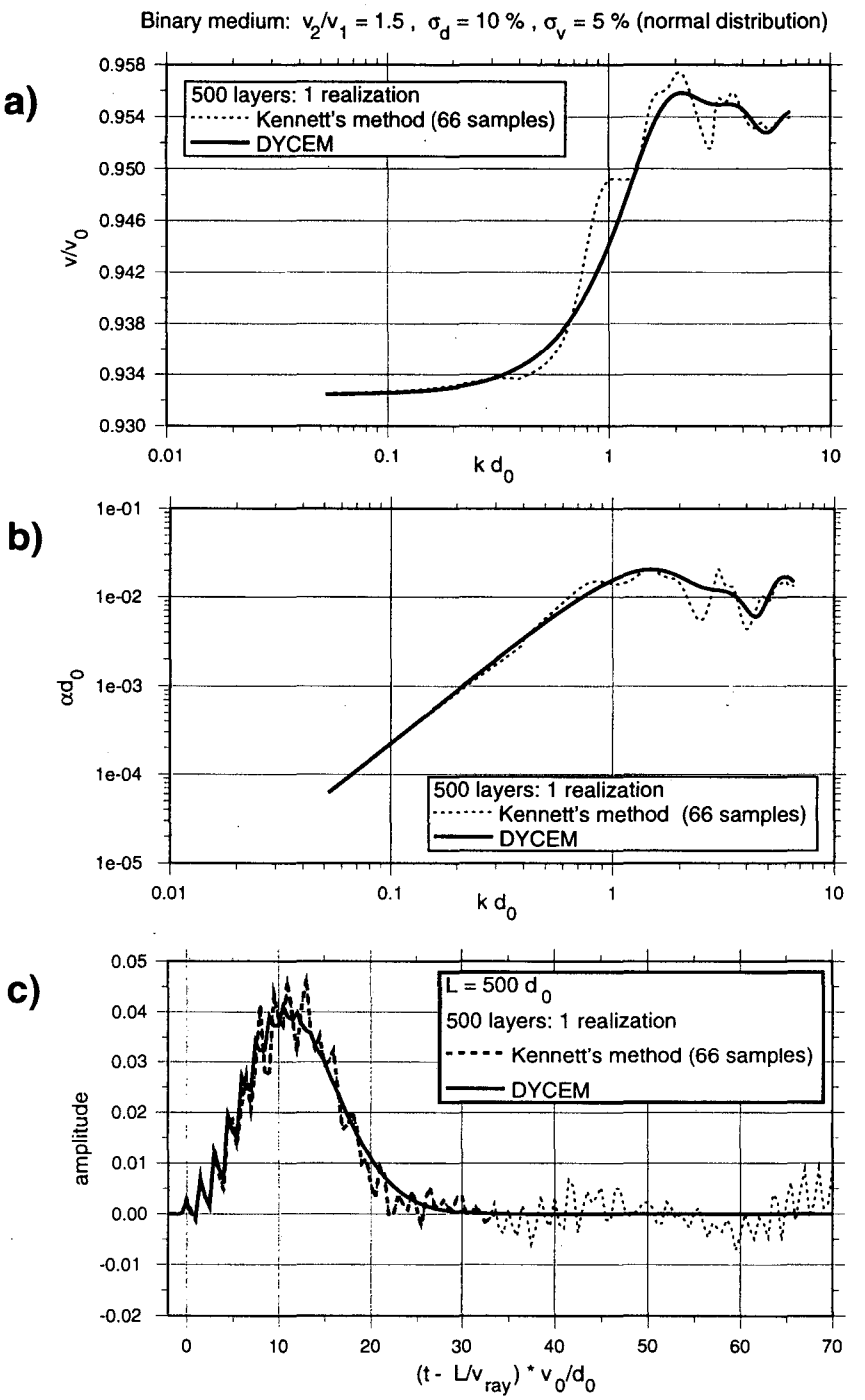

Figure 2.9: Similar to Figure 2.8 with the randomly layered binary medium of Figure 2.2d and the windowed arrival (66 time samples)of one realization.

not successful for some higher frequencies due to the strong attenuation (Figure 2.8b). However, this does not interfere with the observation that the difference between the dynamic composite elastic medium theory and Kennett's method is generally large at most frequencies. The seismogram of Kennett's method shows strong oscillations of the wavelet, which can not be observed on the seismogram of the dynamic composite elastic medium theory (Figure 2.8c). The reason for this discrepancy lies in the violation of the basic assumption of the dynamic composite elastic medium theory, which requires randomly distributed layers within the stack. If this assumption is not fulfilled, multiple scattering between the individual layers becomes important and causes strong dispersion of the phase velocity (Figure 2.8a) and marked resonances in the amplitude (Figure 2.8b).

For our fourth simulation we shuffled the type 1 and type 2 layers and placed them randomly in the stack (Figure 2.2d). Since the first arrival should therefore be coherent, we performed the numerical simulation for one realization only and windowed the arrival in the same manner as in the earlier examples. The results in Figure 2.9 show generally good agreement. Only at higher frequencies does Kennett's method show some interferences (Figure 2.9a and 2.9b) which can not be predicted by the dynamic composite elastic medium theory. Nevertheless, the waveform of the first arrival is almost identical except for the high frequency interferences (Figure 2.9c). Compared with the experimental results

of Marion et al. (1994), the transition from low to high frequency phase velocity is less abrupt, but the center of this zone at $kd_0=1$ agrees well with the experimental data.

2.5 Discussion and conclusions

The comparison between the non-self-consistent and self-consistent theory has demonstrated that only the self-consistent theory accurately predicts the phase velocity at all frequencies. This is a strong argument for the validity of self-consistent theories, and we conjecture that this also applies for three-dimensional media. The comparison between a complete numerical solution and the dynamic composite elastic medium theory shows good agreement for perturbed and binary media if the media are truly random. In this case our theory predicts the coherent arrival of a seismic wave at all frequencies. In addition, our theory is not restricted to small impedance contrasts between the layers. Another advantage of the dynamic composite elastic medium theory is that it can be computed independently of the travel distance. Any intrinsic attenuation within the layers can easily be incorporated by making the velocities complex.

Chapter 3

Dynamic composite elastic medium theory. Part II. Three-dimensional media

3.1 Abstract

Non-self-consistent and self-consistent methods of estimating velocity and attenuation of P-waves and S-waves at all frequencies for heterogeneous media with three-dimensional inclusions are formulated using the scattering functions of the individual inclusions. The methods are the generalization of methods for one-dimensional media presented in the first paper of this series. The specific case of spherical inclusions is calculated with the exact scattering function and compared with several low frequency approximations. The self-consistent estimates are consistent with Berryman's low frequency approximation. We present spectra and waveforms of materials with solid and liquid inclusions in a solid matrix. The results show that the exact scattering functions are required to adequately describe wave propagation at all frequencies. The analysis of liquid inclusions demonstrates that viscous damping may become important only if

scattering attenuation due to spherical pores is small.

3.2 Introduction

Over the last few decades the influence of three-dimensional inclusions on wave propagation has been studied extensively. On one hand, wave propagation has been described by scattering from the inclusions (e.g., Spitzer, 1943; Foldy, 1945; Silberman, 1957; Kuster and Toksöz, 1974; Twersky, 1975; Berryman, 1980a; Berryman, 1980b). On the other hand, fluid flow inside the inclusions has been attributed to have a major effect on wave propagation (e.g., Biot, 1956a; Biot, 1956b; O'Connell and Budiansky, 1977; Dvorkin et al., 1995; Sams et al., 1997).

In the present series of papers we focus on elastic wave propagation which includes scattering and viscous attenuation. The analysis of one-dimensional media has shown that the elastic properties of randomly layered media can be described by the scattering function of the individual layers (chapter 2). In the following, we derive the analogous general dynamic composite elastic medium (DYCEM) theory for three-dimensional inclusions. The results are compared for the special case of spherical inclusions with various low frequency approximations and the general result is applied to solid and liquid inclusions in a solid matrix.

3.3 General dynamic composite elastic medium theory (DYCEM)

A number of different methods have been used to describe the effects of multiple scattering upon the propagation of a plane wave. One is to represent the multiple scattering in terms of an integral equation for the average field (Foldy, 1945; Twersky, 1975) and then solve this integral equation by the method of stationary phase (Ishimaru, 1978). This same integral equation can also be converted to a differential equation which is then solved for a plane wave (Mehta, 1983). Another approach is to estimate the coherent field directly by averaging the effects of multiple scattering in the forward direction over the first Fresnel zone by the method of stationary phase (Groenenboom and Snieder, 1995). Still another approach, which is similar to the one followed in this paper, is to average the scattering field in the forward direction by using the parabolic approximation (Korneev and Johnson, 1998). While these different methods involve somewhat different approximations, any of them could be used for the purposes of this paper, which is to determine the effect of scattering upon the wavenumber of the average field, and all of the methods would produce the same results. In this paper we derive the basic equations in a method slightly different from those just described, primarily to point out how results can be obtained when the concentration of scatterers becomes large, which is generally assumed to be small in the studies mentioned above.

In the following we follow the basic idea of Korneev and Johnson (1998) to calculate P-waves and S-waves in media with three-dimensional inclusions. First we study the effect of one single inclusion on an incident plane wave. Then we use the obtained scattering function to calculate plane waves propagating through media with a small number of three-dimensional inclusions. Finally, we formulate the non-self-consistent and self-consistent estimates to describe the effects of many inclusions.

If a plane wave propagates along the z-axis through an elastic medium, the resulting plane wave at distance z is

$$U_m = U_{m0} e^{-ik_m z}, \tag{3.1}$$

where the index m represents either the P-wave or S-wave, k_m is the corresponding complex wavenumber and U_m and U_{m0} are the spectra of the wave field at distance z and of the incident wave, respectively. Equation (3.1) can also be written in terms of the attenuation α_m and phase velocity v_m

$$U_m = U_{m0} e^{-i\frac{\omega}{v_m}z} e^{-\alpha_m z}, \tag{3.2}$$

where ω is the angular frequency. Comparing equation (3.1) and (3.2), we obtain

$$\alpha_m = -\Im\{k_m\}, \qquad v_m = \Re\{\frac{\omega}{k_m}\}. \tag{3.3}$$

Attenuation and phase velocity are both a function of the complex wavenumber and their frequency dependent properties can therefore be calculated.

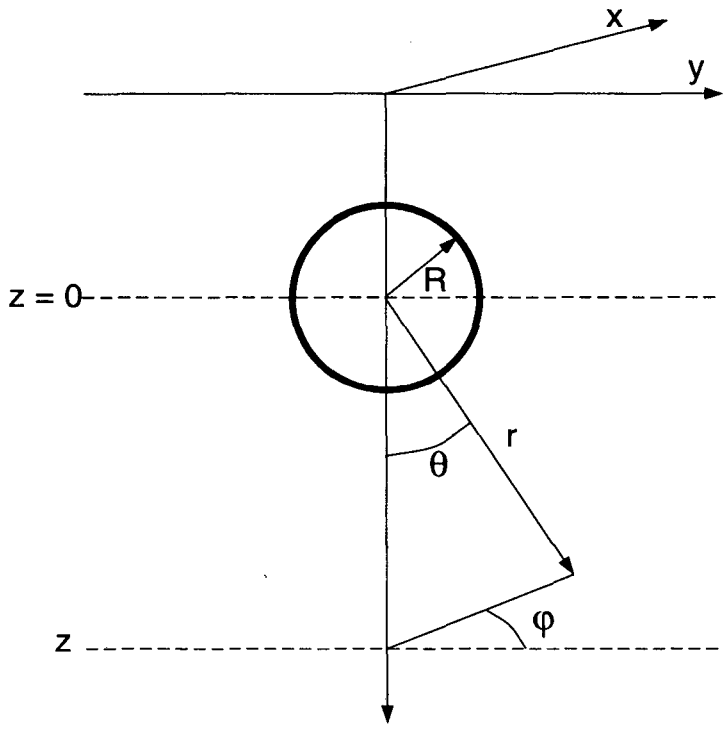

Figure 3.1: A single inclusion with radius R at z=0 in a spherical coordinate system (r,θ,ϕ).

If there is a single inclusion inside the medium, the disturbance of an incident plane wave propagating along the z-axis is described by the scattered field U_m^{sc} and the total field outside the inclusion U_m^{tot} has the form

$$U_m^{tot} = U_m + U_m^{sc}(r, \theta, \phi) \tag{3.4}$$

in a spherical coordinate system (r,θ,ϕ) centered on the scatterer (Figure 3.1). In the far field the scattered field becomes (Korneev and Johnson, 1996)

$$U_m^{sc}(r, \theta, \phi) = U_m A_{mm}(\theta, \phi) \frac{\cos\theta}{r} e^{-ik_m(r-z)}, \tag{3.5}$$

where A_{mm} is the scattering function for P-waves or S-waves. If a small number of inclusions are randomly distributed inside a layer of thickness L (Figure 3.2), the average disturbance of the initial wave field ΔU_m at distance L is

$$\Delta U_m \;=\; L\Delta M \iint U_m^{sc}(r, \theta, \phi) dx dy \tag{3.6}$$

or

$$\Delta U_m \;=\; U_m L\Delta M \iint A_{mm}(\theta, \phi) \frac{z}{r^2} e^{-ik_m(r-z)} dx dy, \tag{3.7}$$

where the integration is over the entire plane perpendicular to the direction of the incident wave and ΔM is the number of inclusions per unit volume. The forward traveling wave is coherently influenced by the inclusions within a few central Fresnel zones only (Van de Hulst, 1957). Thus, we have to consider the forward scattered amplitudes only and can use the parabolic approximation

$$A_{mm}(\theta, \phi) \;\sim\; A_{mm}(\theta = 0, \phi = 0) \equiv A_m(0) \tag{3.8}$$

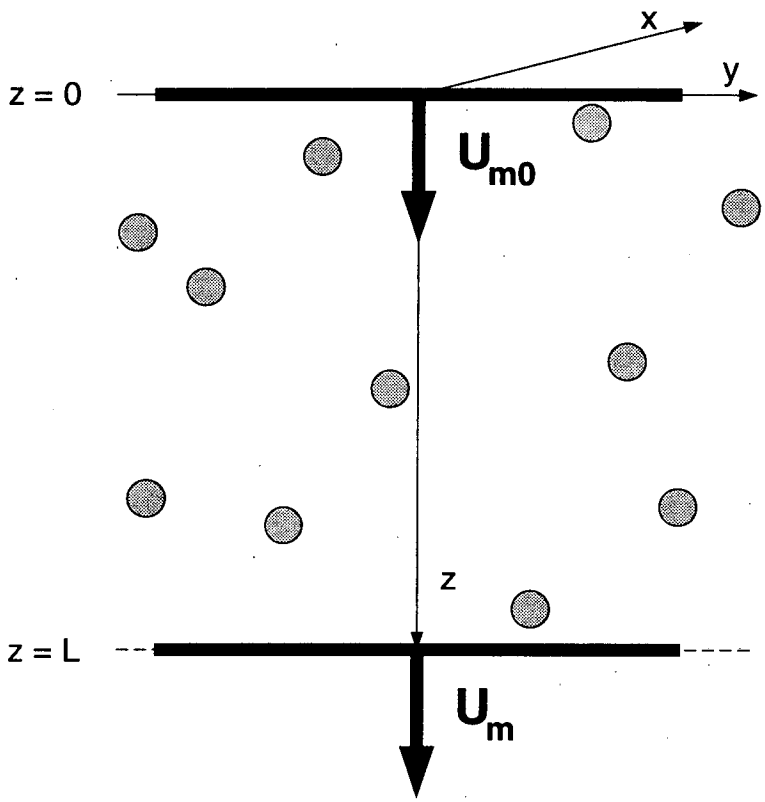

Figure 3.2: Schematic illustration of an incident plane wave U_{m0} and the transmitted plane wave U_m through a layer of thickness L with randomly distributed inclusions.

$$r \sim z + \frac{x^2+y^2}{2r}, \qquad \frac{z}{r} \sim 1.$$

With this approximation equation (3.7) becomes

$$\Delta U_m = U_m L \Delta M \frac{A_m(0)}{r} \iint e^{-ik_m \frac{x^2+y^2}{2r}} dx dy \tag{3.9}$$

$$= U_m L \Delta M \frac{A_m(0)}{r} \int_0^\infty \pi e^{-ik_m \frac{\xi}{2r}} d\xi \tag{3.10}$$

$$= -i2\pi U_m \frac{A_m(0)}{k_m} L \Delta M. \tag{3.11}$$

Since the number of inclusions is very small, the disturbance of the initial wave field at distance L can also be described by the Taylor series expansion of equation (3.1) keeping the first order derivative

$$\Delta U_m = -iLU_m \Delta k_m \tag{3.12}$$

and comparing with equation (3.11), the wavenumber change is

$$\Delta k_m = 2\pi \frac{A_m(0)}{k_m} \Delta M. \tag{3.13}$$

3.3.1 Non-self-consistent theory

In the first paper of this series, we have shown that only the self-consistent theory yields the correct attenuation and phase velocity in one-dimensional media at all frequencies. Nevertheless, the non-self-consistent theory is still a good approximation for small inclusion concentrations and is generally easy to compute. We will also use the non-self-consistent theory to derive the self-consistent theory, analogous to the one-dimensional case.

To derive the non-self-consistent wavenumber $(k_m)_{NS}$, we assume a homogeneous matrix of type 0 with inclusions of type 1. For this composite elastic medium, equation (3.13) becomes

$$\Delta k_m = \frac{2\pi}{k_{m0}} [A_m(0)]_{10} \Delta M, \tag{3.14}$$

where the indices 1 and 0 indicate the type 1 inclusion and the type 0 matrix, respectively. Equation (3.14) can be integrated over the number of inclusions and we obtain

$$(k_m)_{NS} = k_{m0} + \frac{2\pi}{k_{m0}} [A_m(0)]_{10} M, \tag{3.15}$$

where M is the number of inclusions per unit volume. If there are N_1 different kind of inclusions, equation (3.15) can be generalized to

$$(k_m)_{NS} = k_{m0} + \frac{2\pi}{k_{m0}} \sum_{n=1}^{N_1} [A_m(0)]_{n0} M_n, \tag{3.16}$$

where M_n is the number of the n-th type inclusion per unit volume. Including the matrix, N is the total number of objects and the scattering functions $[A_m(0)]_{n0}$ for $n=N_1+1,\ldots,N$ are taken to be zero. Equation (3.16) is therefore equivalent to

$$(k_m)_{NS} = k_{m0} + \frac{2\pi}{k_{m0}} \sum_{n=1}^{N} [A_m(0)]_{n0} M_n. \tag{3.17}$$

3.3.2 Self-consistent theory

As the number of inclusions increases, the non-self-consistent theory is no longer valid and a self-consistent formulation is needed (chapter 2). Analogous

to the one-dimensional media, we replace the true background medium by the effective medium. In this way, all objects including the matrix act as scatterers relative to the effective medium. To compute the self-consistent wavenumber $(k_m)_S$, we simply replace the matrix by the effective medium and equation (3.17) becomes

$$(k_m)_S = (k_m)_S + \frac{2\pi}{(k_m)_S} \sum_{n=1}^{N} [A_m(0)]_{nS} M_n \tag{3.18}$$

or

$$\frac{2\pi}{(k_m)_S} \sum_{n=1}^{N} [A_m(0)]_{nS} M_n = 0. \tag{3.19}$$

It is also necessary to introduce the self-consistent density defined by

$$\rho_S = \sum_{n=1}^{N} \rho_n V_n M_n, \tag{3.20}$$

where V_n is the volume and ρ_n the density of the n-th type inclusion. Equation (3.19) is the analogous result to equation (2.11) for one-dimensional media. We showed for one-dimensional media (chapter 2) that the self-consistent formulation is valid if the layers are randomly distributed. In analogy with that result, we therefore conjecture that equation (3.19) is valid for randomly distributed three-dimensional inclusions.

3.4 Dynamic composite elastic medium theory for spherical inclusions

A spherical inclusion is one of the few three-dimensional objects for which the scattering problem has an exact solution. For light scattering it was formulated by Mie (1908) and a comprehensive discussion of the topic can be found in Van de Hulst (1957). Elastic scattering by spherical inclusions has been the topic of a number of studies, where some authors used potentials in their approach (e.g., Ying and Truell, 1956; Truell et al., 1969; Yamakawa, 1962) and others used displacements (e.g., Petrashen, 1950; Korneev and Johnson, 1993; Korneev and Johnson, 1996). Since we have formulated the scattering problem in terms of displacements, we use the results for incident P-waves and S-waves by Korneev and Johnson (1996) for our calculations.

For one single spherical type 1 inclusion with radius R_1 in a homogeneous type 0 background, Korneev and Johnson (1996) give the scattering functions

$$[A_p(0)]_{10} = \frac{i}{k_{p0}} \sum_{l \geq 0}^{\infty} (2l+1) a_l^{pp} \tag{3.21}$$

$$[A_s(0)]_{10} = \frac{i}{2k_{s0}} \sum_{l \geq 1}^{\infty} (2l+1)(b_l^{ss} + c_l^s), \tag{3.22}$$

with

$$a_l^{pp}(R_1, k_{p0}, k_{s0}, \rho_0, k_{p1}, k_{s1}, \rho_1)$$

$$b_l^{ss}(R_1, k_{p0}, k_{s0}, \rho_0, k_{p1}, k_{s1}, \rho_1)$$

$$c_l^s(R_1, k_{s0}, k_{s1}).$$

Here a_l^{pp}, b_l^{ss} and c_l^s are the l-th order canonical scattering coefficients, which consist of spherical Bessel and Hankel functions. For spherical inclusions we can define the concentration

$$c_n = \frac{4\pi}{3} R_n^3 M_n, \tag{3.23}$$

where R_n is the radius of the n-th type inclusion. With equation (3.17) and (3.23) the non-self-consistent wavenumber is

$$(k_m)_{NS} = k_{m0} + \frac{3}{2k_{m0}} \sum_{n=1}^{N} [A_m(0)]_{n0} \frac{c_n}{R_n^3} \tag{3.24}$$

with

$$\sum_{n=1}^{N} c_n = 1$$

and with equation (3.19) and (3.23) the self-consistent wavenumber is the solution of the equation

$$\frac{3}{2(k_m)_S} \sum_{n=1}^{N} [A_m(0)]_{nS} \frac{c_n}{R_n^3} = 0 \tag{3.25}$$

with

$$\rho_S = \sum_{n=1}^{N} \rho_n c_n, \quad \sum_{n=1}^{N} c_n = 1.$$

To obtain the self-consistent wavenumbers, equation (3.25) must be solved simultaneously for P-waves and S-waves. Since the wavenumbers are complex, equation (3.25) describes a set of four equations for each frequency. In general, equation (3.25) cannot be solved analytically and we have applied Muller's numerical method (Press et al., 1992) to compute the self-consistent wavenumbers.

3.4.1 Low frequency approximations

The general results of the dynamic composite elastic medium theory for spherical inclusions can be compared with the low frequency solution by Berryman (1980a). At low frequencies the scattering function between a type 1 inclusion and type 0 background for the P-wave becomes (Korneev and Johnson, 1996)

$$\begin{aligned}[A_p(0)]_{10} &= R^3 k_{p0}^2 [B_0 - B_1 - B_2] \\ &\quad -iR^6 k_{p0}^5 \left[B_0^2 + \frac{2+\gamma_0^3}{3\gamma_0^3} B_1^2 + \frac{3+2\gamma_0^4}{10\gamma_0^4} B_2^2 \right]\end{aligned} \tag{3.26}$$

and for the S-wave

$$\begin{aligned}[A_s(0)]_{10} &= R^3 k_{s0}^2 \left[-B_1 - \frac{3}{4\gamma_0^2} B_2 \right] \\ &\quad -iR^6 k_{s0}^5 \left[\frac{2+\gamma_0^3}{3} B_1^2 + 3\frac{3+2\gamma_0^5}{40\gamma_0^4} B_2^2 \right]\end{aligned} \tag{3.27}$$

with

$$\begin{aligned} v_{p0}^2 &= \frac{K_0 + \frac{4}{3}\mu_0}{\rho_0}, \qquad v_{s0}^2 = \frac{\mu_0}{\rho_0}, \qquad \gamma_0^2 = \left(\frac{v_{s0}}{v_{p0}}\right)^2 \\ B_0(K_1, K_0, \mu_0) &= \frac{K_0 - K_1}{3K_1 + 4\mu_0}, \qquad B_1(\rho_1, \rho_0) = \frac{\rho_0 - \rho_1}{3\rho_0} \\ B_2(\mu_1, K_0, \mu_0) &= \frac{20}{3} \frac{\mu_0(\mu_1 - \mu_0)}{6\mu_1(K_0 + 2\mu_0) + \mu_0(9K_0 + 8\mu_0)}, \end{aligned}$$

where K_0, μ_0, ρ_0 and K_1, μ_1, ρ_1 are the bulk modulus, shear modulus and density of the type 0 background and of the type 1 inclusion, respectively. With equation (3.24) and (3.26) the non-self-consistent wavenumber at low frequencies

for the P-wave is therefore

$$
\begin{aligned}
(k_p)_{NS} &= k_{p0} + \frac{3k_{p0}}{2}\sum_{n=1}^{N}\left[B_0 - B_1 - B_2\right]c_n \\
&\quad -i\frac{3k_{p0}^4}{2}\sum_{n=1}^{N}\left[B_0^2 + \frac{2+\gamma_0^3}{3\gamma_0^3}B_1^2 + \frac{3+2\gamma_0^4}{10\gamma_0^4}B_2^2\right]R_n^3 c_n
\end{aligned}
\tag{3.28}
$$

and with equation (3.27) for the S-wave

$$
\begin{aligned}
(k_s)_{NS} &= k_{s0} - \frac{3k_{s0}}{2}\sum_{n=1}^{N}\left[B_1 + \frac{3}{4\gamma_0^2}B_2\right]c_n \\
&\quad -i\frac{3k_{s0}^4}{2}\sum_{n=1}^{N}\left[\frac{2+\gamma_0^3}{3}B_1^2 + 3\frac{3+2\gamma_0^5}{40\gamma_0^4}B_2^2\right]R_n^3 c_n,
\end{aligned}
\tag{3.29}
$$

with

$$
\begin{aligned}
B_0(K_n, K_0, \mu_0) &= \frac{K_0 - K_n}{3K_n + 4\mu_0}, \qquad B_1(\rho_n, \rho_0) = \frac{\rho_0 - \rho_n}{3\rho_0} \\
B_2(\mu_n, K_0, \mu_0) &= \frac{20}{3}\frac{\mu_0(\mu_n - \mu_0)}{6\mu_n(K_0 + 2\mu_0) + \mu_0(9K_0 + 8\mu_0)}
\end{aligned}
$$

In the low frequency limit, equation (3.28) and (3.29) simplify to

$$
(v_p)_{NS} = v_{p0}\left[1 + \frac{3}{2}\sum_{n=1}^{N}\left(B_0 - B_1 - B_2\right)c_n\right]^{-1} \tag{3.30}
$$

$$
(v_s)_{NS} = v_{s0}\left[1 - \frac{3}{2}\sum_{n=1}^{N}\left(B_1 + \frac{3}{4\gamma_0^2}B_2\right)c_n\right]^{-1}. \tag{3.31}
$$

With equation (3.25) and (3.26) the self-consistent elastic moduli at low frequencies for the P-wave are obtained from

$$
\begin{aligned}
0 &= \sum_{n=1}^{N}\left[B_0 - B_1 - B_2\right]c_n \\
&\quad -i(k_p)_S^3\sum_{n=1}^{N}\left[B_0^2 + \frac{2+\gamma_S^3}{3\gamma_S^3}B_1^2 + \frac{3+2\gamma_S^4}{10\gamma_S^4}B_2^2\right]R_n^3 c_n
\end{aligned}
\tag{3.32}
$$

and with equation (3.27) for the S-wave

$$
\begin{aligned}
0 &= \sum_{n=1}^{N}\left[B_1 + \frac{3}{4\gamma_S^2}B_2\right]c_n \\
&\quad + i(k_s)_S^3 \sum_{n=1}^{N}\left[\frac{2+\gamma_S^3}{3}B_1^2 + 3\frac{3+2\gamma_S^5}{40\gamma_S^4}B_2^2\right]R_n^3 c_n,
\end{aligned}
\tag{3.33}
$$

with

$$
\begin{aligned}
(v_p)_S^2 &= \frac{K_S + \frac{4}{3}\mu_S}{\rho_S}, \qquad (v_s)_S^2 = \frac{\mu_S}{\rho_S}, \qquad \gamma_S^2 = \left(\frac{(v_s)_S}{(v_p)_S}\right)^2 \\
B_0(K_n, K_S, \mu_S) &= \frac{K_S - K_n}{3K_n + 4\mu_S}, \qquad B_1(\rho_n, \rho_S) = \frac{\rho_S - \rho_n}{3\rho_S}, \\
B_2(\mu_n, K_S, \mu_S) &= \frac{20}{3}\frac{\mu_S(\mu_n - \mu_S)}{6\mu_n(K_S + 2\mu_S) + \mu_S(9K_S + 8\mu_S)}
\end{aligned}
$$

where K_S, μ_S and ρ_S are the self-consistent bulk modulus, shear modulus and density. In the low frequency limit, equation (3.32) and (3.33) simplify to

$$
\begin{aligned}
\sum_{n=1}^{N} B_0(K_n, K_S, \mu_S)c_n &= 0 \\
\sum_{n=1}^{N} B_1(\rho_n, \rho_S)c_n &= 0 \\
\sum_{n=1}^{N} B_2(\mu_n, K_S, \mu_S)c_n &= 0
\end{aligned}
\tag{3.34}
$$

Equation (3.30) and (3.31) describe the non-self-consistent elastic properties in the low frequency limit for P-waves and S-waves, respectively. Kuster and Toksöz (1974) have formulated the non-self-consistent estimates differently, but for small inclusion concentrations their phase velocities agree with those obtained here. Equation (3.34) describes the self-consistent elastic properties in the low frequency limit and was first derived by Berryman (1980a), where the

solutions of equation (3.34) are discussed in detail. Berryman has shown that the estimates for the bulk and shear moduli always satisfy the rigorous Hashin-Shtrikman bounds (Hashin and Shtrikman, 1963) and reduce to the exact results in those cases where exact results are known.

It is important to note that in the low frequency approximation the real part of the wavenumbers are independent of the inclusion radii, but the imaginary part is proportional to R^3 (equation (3.28), (3.29), (3.32)) and (3.33)). Thus, at low frequencies the attenuation due to scattering of P-waves and S-waves always depends on the microscopic geometry of the inclusions, whereas the velocity does not.

3.5 Viscous fluids

The case of fluid inclusions is of special interest in geophysical problems. There exist a variety of theories which predict significant effects of pore fluids on seismic and ultrasonic waves due to fluid flow in pores and cracks (e.g., Biot, 1956a; Biot, 1956b; O'Connell and Budiansky, 1977; Dvorkin et al., 1995). In the case of the dynamic composite elastic medium theory, the fluid movement within the inclusions can be incorporated by treating fluids as viscoelastic materials. A detailed derivation of elastic waves in linearly viscous fluids is given by Caviglia and Morro (1988). They have shown that there exist transverse and longitudinal

waves in viscous fluids. The wavenumber of the transverse wave is

$$k_T = \sqrt{\frac{\omega\rho}{2\eta}}(1-i) \tag{3.35}$$

and of the longitudinal wave

$$k_L = \frac{\omega}{v_0}\sqrt{\frac{1+\sqrt{1+(Q_L^{-1})^2}}{2\left[1+(Q_L^{-1})^2\right]}}\left[1-i\frac{Q_L^{-1}}{1+\sqrt{1+(Q_L^{-1})^2}}\right], \tag{3.36}$$

with

$$Q_L^{-1} = \frac{4\omega\eta}{3\rho v_0^2},$$

where ρ is the density and η the dynamic viscosity of the fluid. v_0 is the low frequency velocity and Q_L the quality factor of the longitudinal wave. The elastic parameters are therefore

$$K = \rho v_0^2, \qquad \mu = i\omega\eta, \tag{3.37}$$

where K is the bulk modulus and μ is the shear modulus of the fluid. Since the shear modulus is purely imaginary, the transverse wave is a diffusive wave and causes attenuation of the longitudinal wave. With equation (3.37) viscous fluids are easily incorporated into the general dynamic composite elastic medium theory.

3.6 Examples

For all the following examples we have chosen composites that consists of only two different materials to simplify the interpretation of the results. We

Table 3.1: Material properties of the matrix and inclusions: P-wave velocity v_p, S-wave velocity v_s, density ρ and dynamic viscosity η.

Material	v_p (m/s)	v_s (m/s)	ρ (kg/m^3)	η (Pa s)
Matrix	6000	4000	2650	0
Inclusion in Model 1	4500	3000	2300	0
Inclusion in Model 2	1500	0	1000	0.001

have also assumed that the number of inclusions is equal to the number of matrix objects. Thus, if R_1 is the inclusion radius, the matrix radius R_0 is

$$R_0 = R_1 \sqrt[3]{\frac{1-c}{c}}, \tag{3.38}$$

where c is the inclusion concentration.

3.6.1 Model 1: Solid spherical inclusions with identical radii in a solid matrix

For the first example we chose a material with 10% inclusions having identical radii and the material properties in Table 3.1. Figure 3.3 shows the phase velocity and attenuation for P-waves and S-waves, respectively. The self-consistent method has been calculated with equation (3.25) and the non-self-consistent method with equation (3.24). The difference between the two methods is small due to the small inclusion concentration, although the non-self-consistent method consistently gives higher velocities and lower attenuation at low frequencies. The self-consistent low frequency approximation has been com-

puted with the scattering functions in equation (3.32) and (3.33), i.e., Rayleigh scattering has been assumed. The low frequency approximation and the exact solution merge if $k_m R_1 < 0.1$. A closer inspection of Figure 3.3 shows that the Rayleigh approximation for the attenuation is valid for $k_m R_1 < 0.4$, i.e., the phase velocity starts to deviate from the Rayleigh approximation before the attenuation does.

Based on the non-dimensional frequency $k_m R_1$, the frequency dependence of P-waves and S-waves can be separated into three different regimes:

- $k_m R_1 < 0.1$: This low frequency range is commonly called the Rayleigh regime and can be described by the low frequency approximation. The phase velocity is less than the matrix velocity and the attenuation is proportional to ω^4.

- $0.1 < k_m R_1 < 10$: This intermediate frequency range marks the transition from the low frequency to the high frequency behavior. The phase velocity is slightly less than the effective medium velocity at lower frequencies, but rises sharply to the matrix velocity at higher frequencies. The attenuation shows no simple power law frequency dependence and starts to oscillate at higher frequencies.

- $k_m R_1 > 10$: In this high frequency range the phase velocity approaches the matrix velocity and the attenuation becomes approximately constant. The

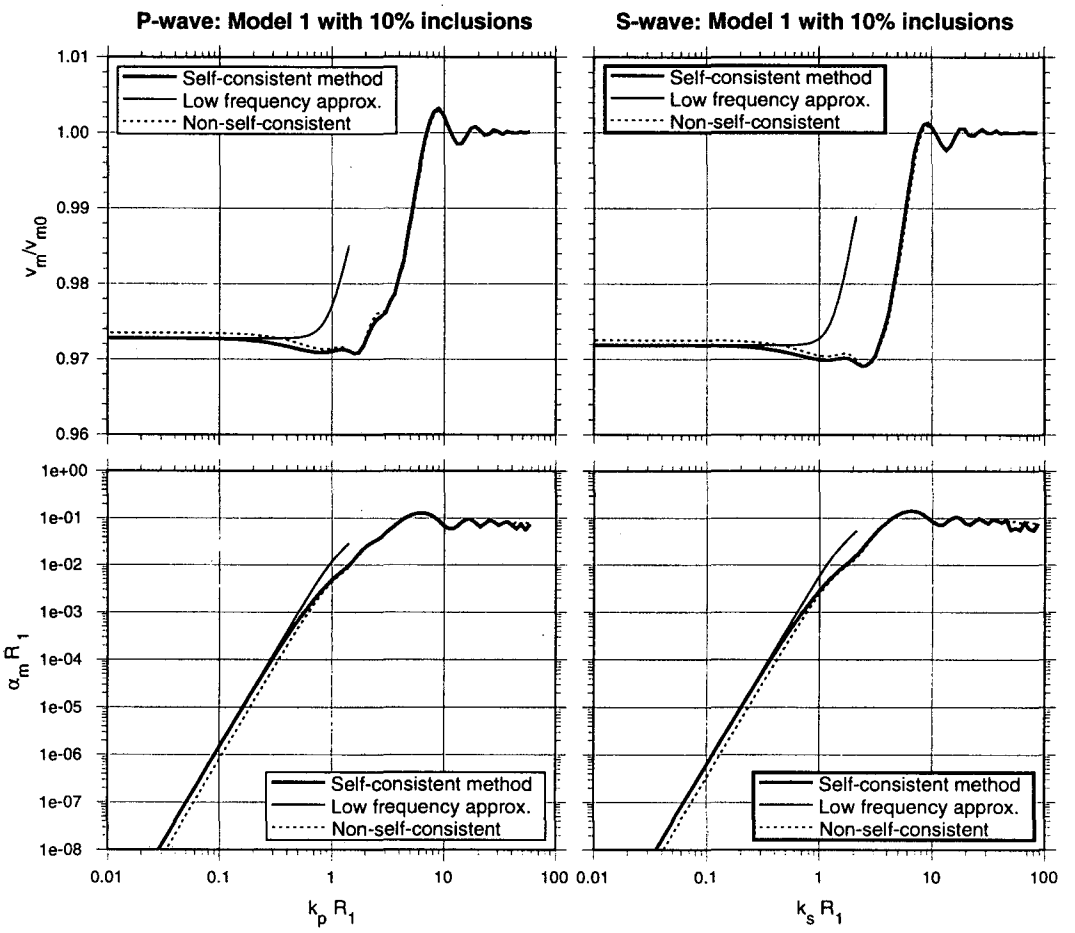

Figure 3.3: Self-consistent calculations of phase velocity and attenuation as a function of normalized frequency for Model 1 with 10% inclusions having radius R_1. v_m is the phase velocity, v_{m0} the matrix velocity and α_m the attenuation, where the index m is either the P-wave or the S-wave. The results for the P-wave are on the left hand side and for the S-wave on the right hand side.

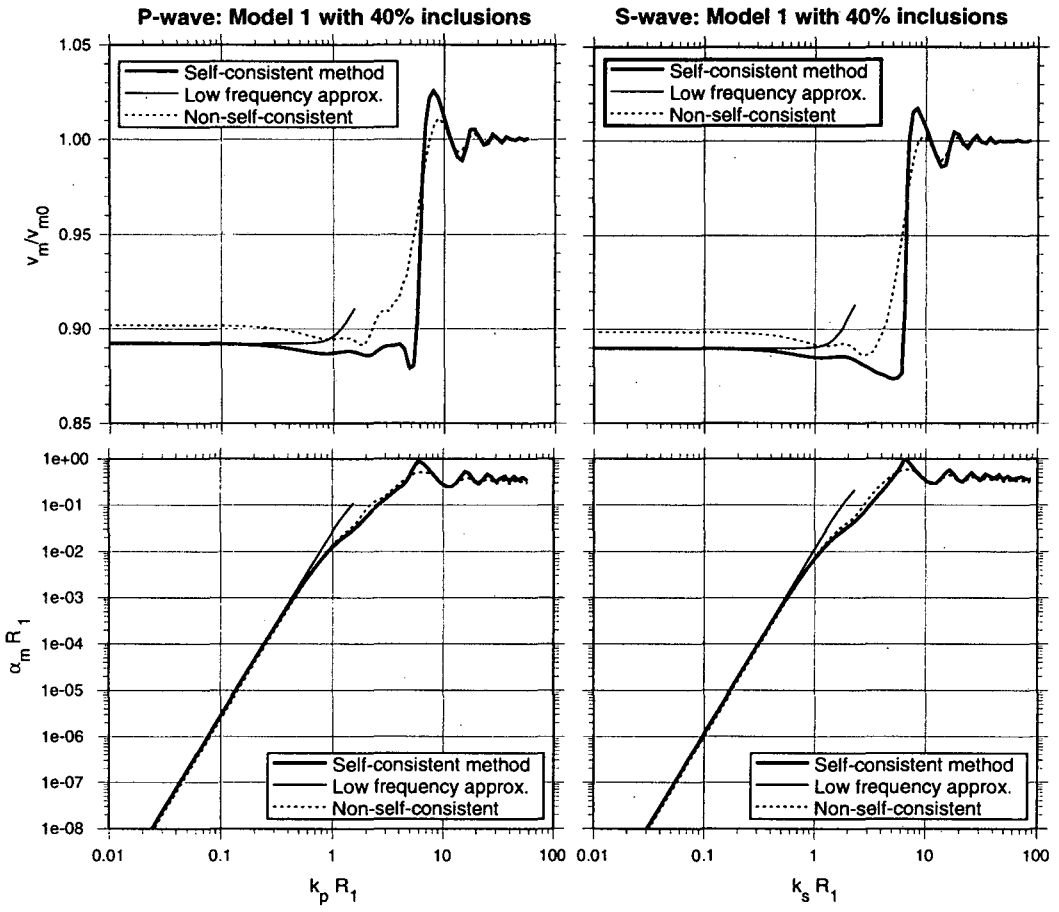

Figure 3.4: Similar to Figure 3.3: Model 1 with 40% inclusions with radius R_1.

oscillations in velocity and attenuation are due to resonance effects within the inclusions and are therefore characteristic of the inclusion dimensions and properties.

Figure 3.4 shows similar results for 40% inclusions with identical radii. Now, at low frequencies the non-self-consistent phase velocity deviates significantly from the self-consistent results. Only at higher frequencies do the two methods begin to merge, which indicates that the interaction between the inclusions

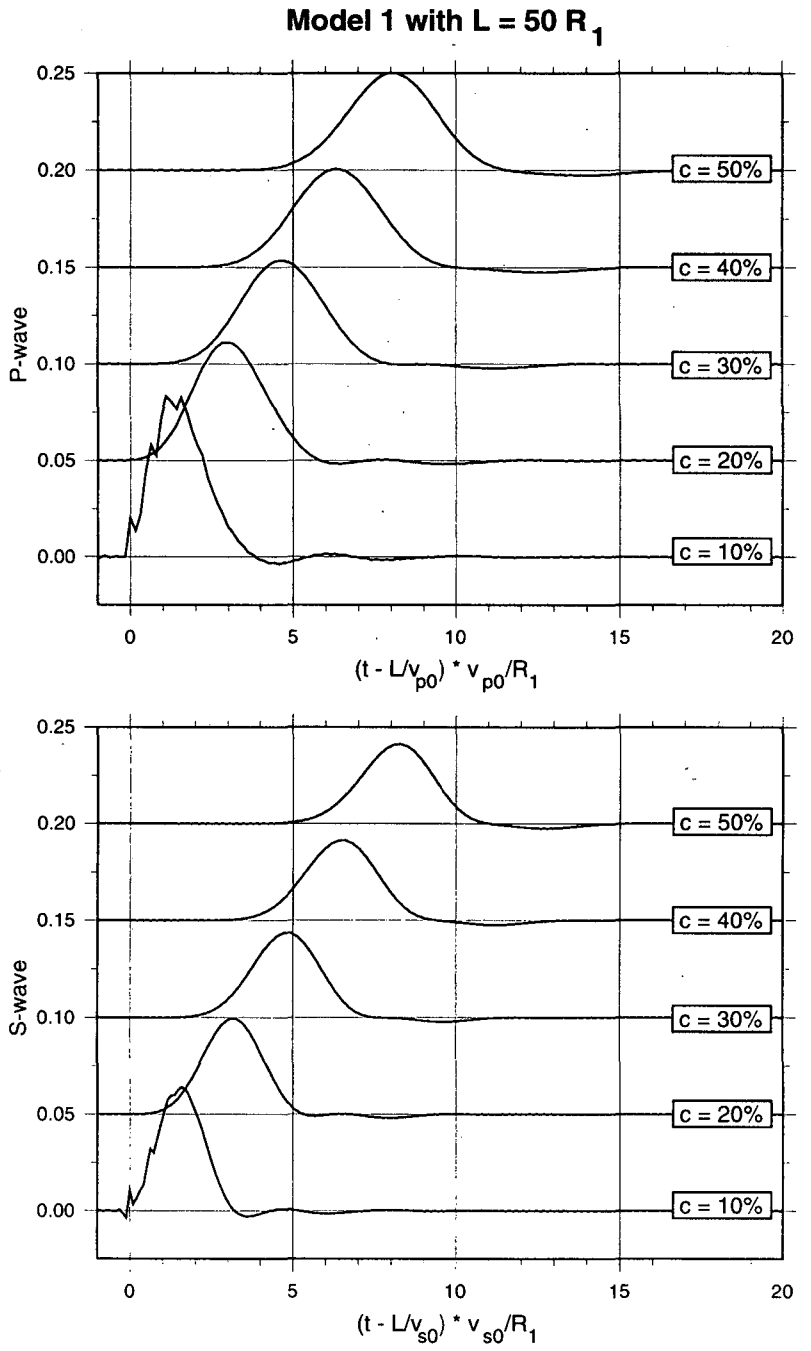

Figure 3.5: Seismograms for Model 1 with L = 50 R_1 propagation distance for different inclusion concentrations using the self-consistent method. t is the travel time, L the propagation distance, v_{p0} the P-wave velocity and v_{s0} the S-wave velocity of the matrix. The input pulse is a delta function with $k_pR_1 = 20$ maximum frequency.

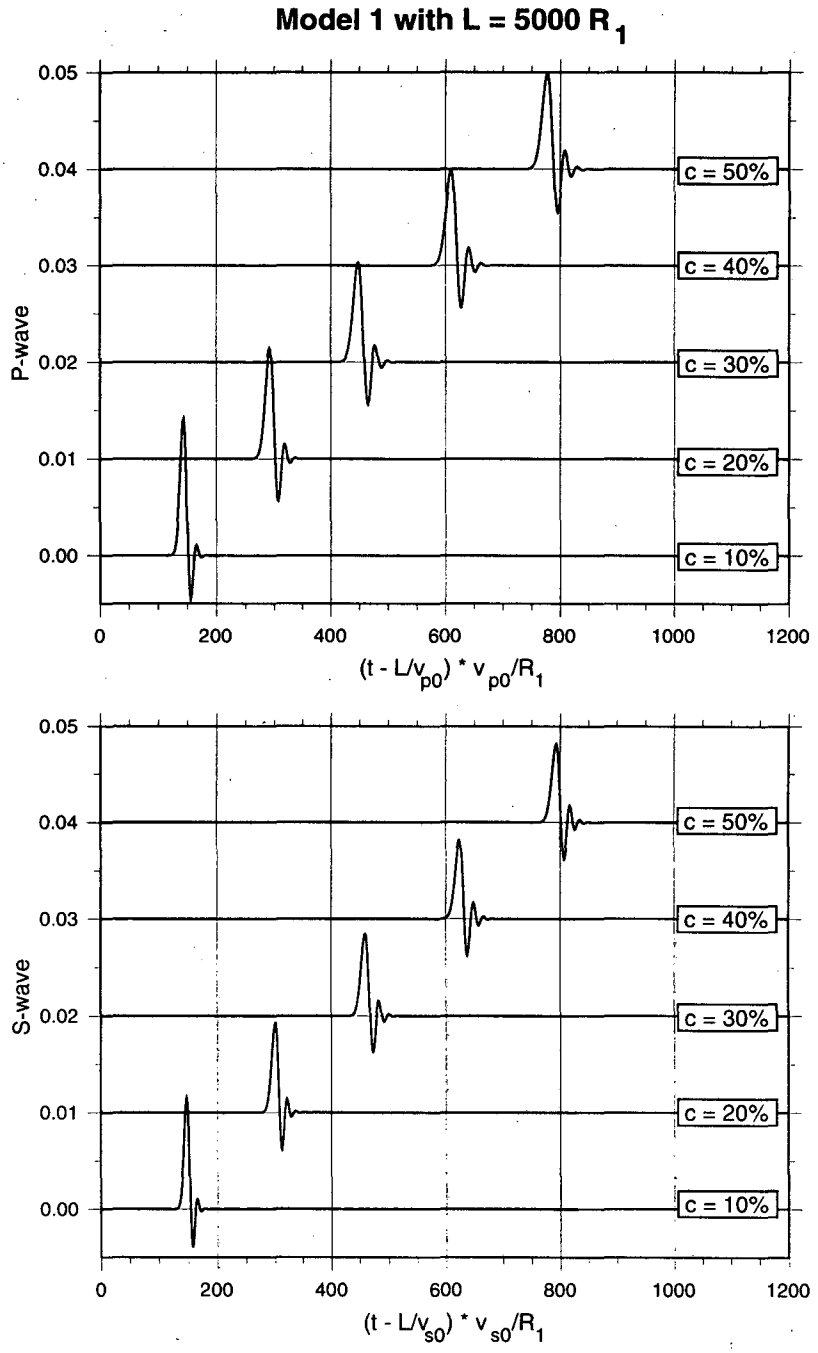

Figure 3.6: Similar to Figure 3.5 for L = 5000 R_1 propagation distance.

becomes less important. In comparison to Figure 3.3, the self-consistent phase velocity changes more rapidly from the low to the high frequency behavior, because the first resonance peak of the inclusions is much stronger. In addition, the interference effects at high frequencies are more pronounced. The phase velocity and attenuation enables one to compute seismograms for different inclusion concentrations. Figure 3.5 shows the seismograms for the Model 1 inclusions with $L = 50\ R_1$ propagation distance. The waveforms look similar to the waveforms in one-dimensional media except for the small oscillations following the primary pulse. For 10% inclusion concentration the wave traveling with the matrix velocity can still be observed. With increasing concentration the high frequencies have been attenuated and the slower low frequency wave becomes dominant. The travel time is approximately a linear function of the inclusion concentration and the amplitude changes are small for P-waves and S-waves. However, the primary pulse widens significantly with more inclusions. The appearance of the seismograms changes significantly for $L = 5000\ R_1$ propagation distance (Figure 3.6). The signal becomes more oscillatory and is no longer confined to one dominant pulse. The travel time is still a linear function of the inclusions concentration and the amplitude changes remain small.

3.6.2 Model 1: Solid spherical inclusions with log-normal distributed radii in a solid matrix

In general, inclusion radii are rarely uniform and a distribution in radius is more appropriate. In hydrological problems, the log-normal distribution is commonly used, partly because there are no negative values possible. Figure 3.7 shows log-normal radius distributions with 0%, 20% and 100% standard deviations. We have used these distribution and Model 1 with 40% inclusions to compute phase velocity and attenuation using the self-consistent method. Both phase velocity and attenuation show that 20% standard deviation is sufficient to suppress most of the resonance effects within the inclusions (Figure 3.8). The phase velocity changes less rapidly from low to high frequency behavior and the attenuation at lower frequencies increases due to a few large inclusions. With 100% standard deviation these features become more pronounced. The phase velocity behavior resembles the standard linear solid model (Aki and Richards, 1980), but the frequency power law for the attenuation is different. The overall attenuation due to scattering is stronger due to some large inclusions. The effect of the log-normal radius distributions on the seismogram is shown in Figure 3.9, where the oscillatory nature is being suppressed, the duration of the first pulse is increased and the amplitudes have decreased. However, the duration of the entire wavelet remains approximately the same.

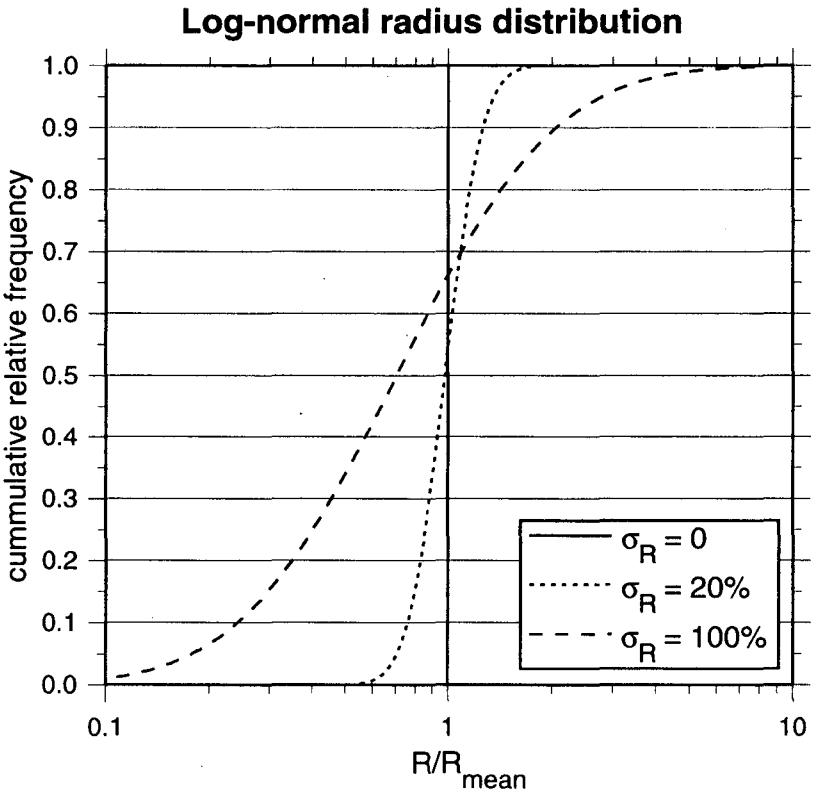

Figure 3.7: Log-normal distribution of the inclusion radius R with the mean radius R_{mean} and the standard deviation σ_R.

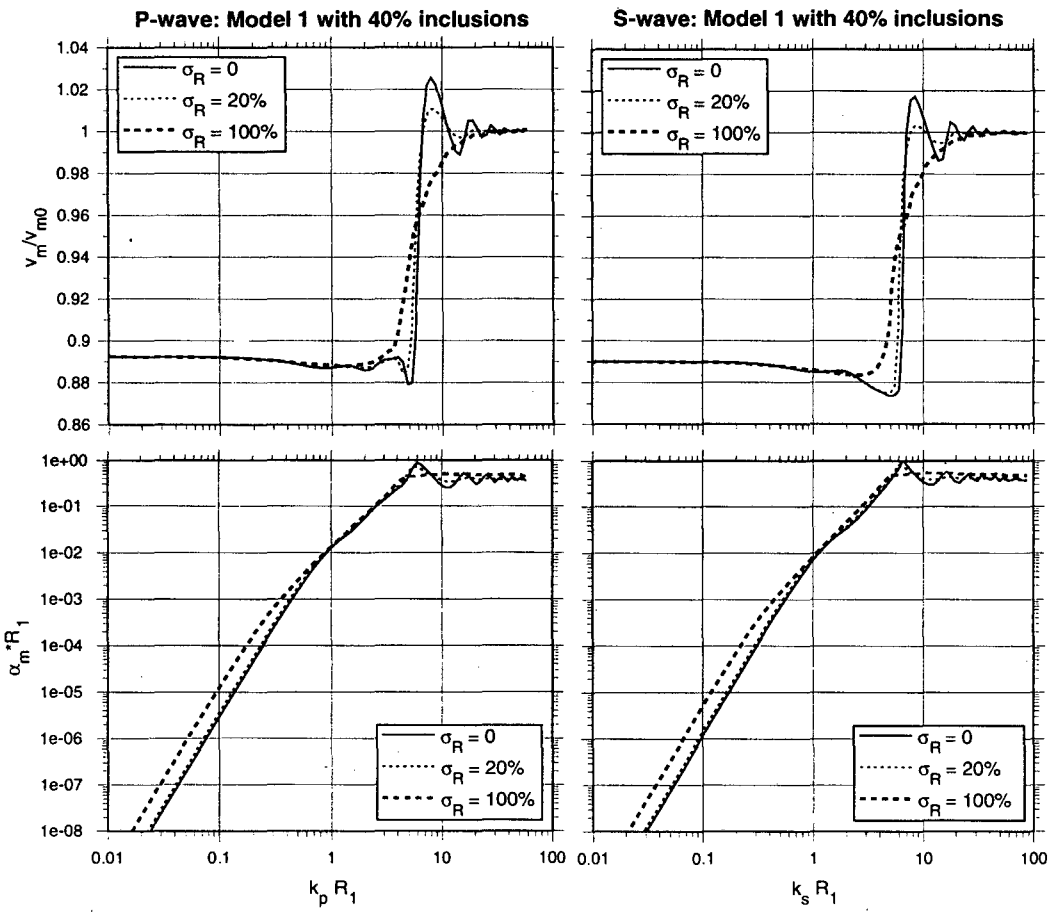

Figure 3.8: Similar to the self-consistent calculations in Figure 3.3 for Model 1 with 40% inclusions and the log-normal radius distributions in Figure 3.7.

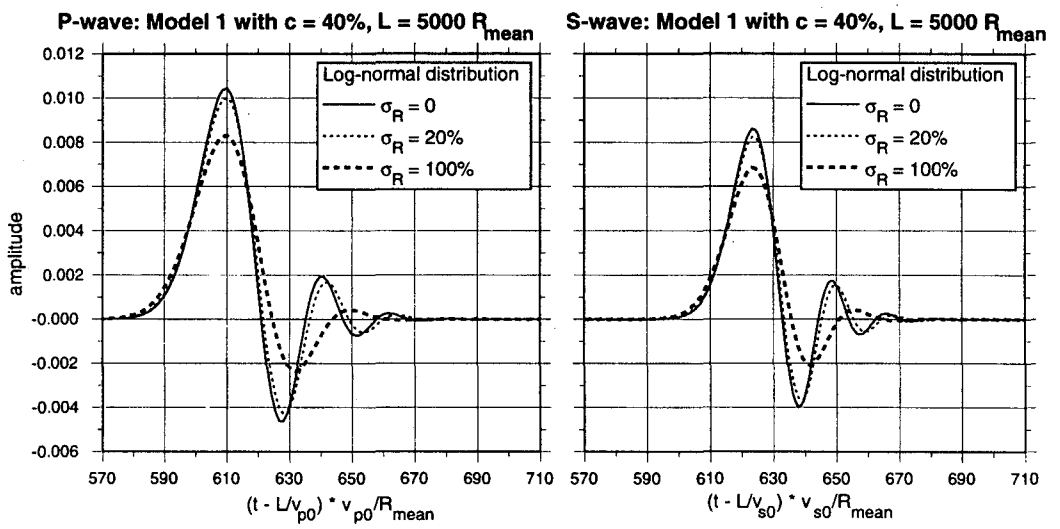

Figure 3.9: Seismograms for Model 1 with L = 5000 R_{mean} propagation distance for 40% inclusions and the log-normal radius distributions in Figure 3.7 using the self-consistent method.

3.6.3 Model 2: Liquid spherical inclusions with identical radii in a solid matrix

The inclusion type in Model 2 is water and the material properties are listed in Table 3.1. For the following calculation we varied the viscosity of water by four decades to demonstrate the effect of viscous damping. Figure 3.10 and 3.11 show the phase velocity and attenuation for 10% and 40% inclusions with 1 mm radius, respectively. For 10% inclusions, the effect of viscous damping on the phase velocity is generally small for P-waves and S-waves and at low frequencies only viscous damping becomes stronger than scattering attenuation. However, the total attenuation at those frequencies is small enough to be negligible in practical applications. With 40% inclusions, the resonance effects at higher

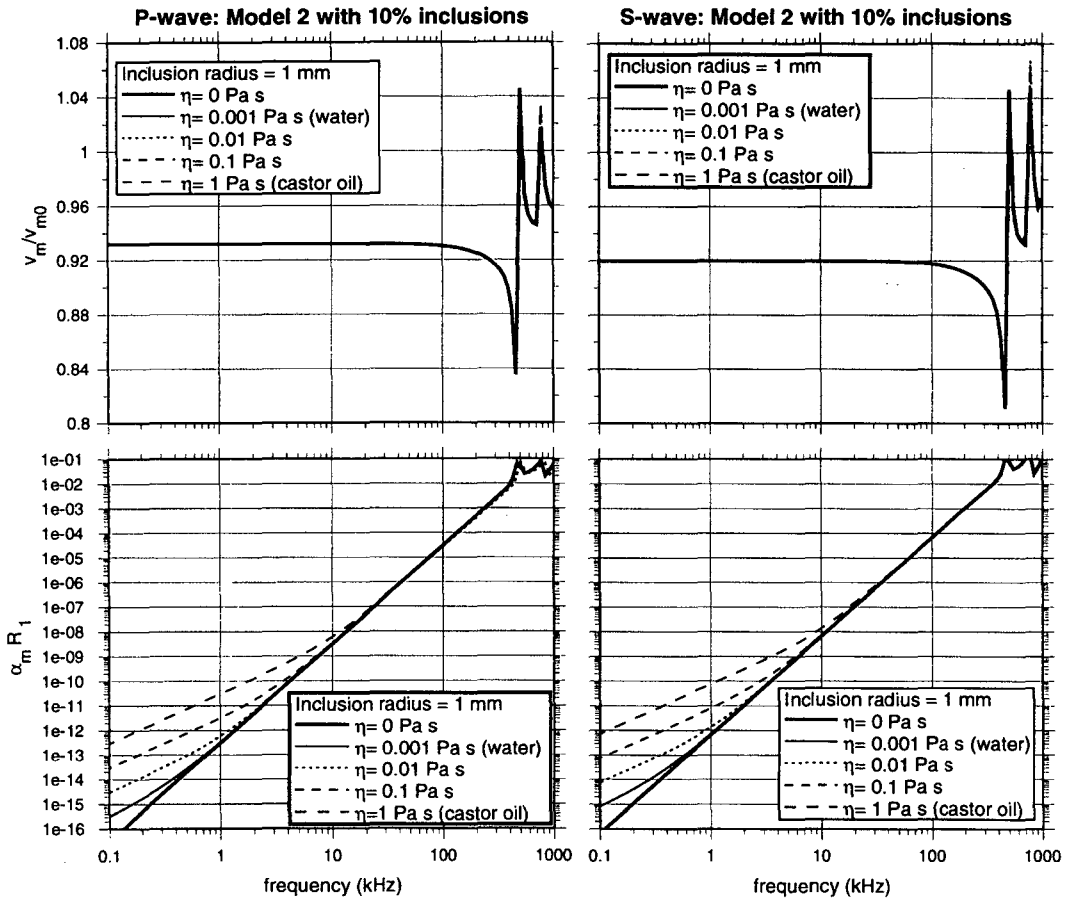

Figure 3.10: Similar to Figure 3.3 for Model 2 with 10% inclusions having radius R_1=1 mm and different viscosities η using the self-consistent method.

frequencies have been suppressed and the total attenuation is stronger, but viscous damping is still only important for highly viscous fluids.

Figure 3.12 shows the seismograms for water inclusions with R_1 = 1 mm radius and L = 50 R_1 propagation distance. In contrast to Model 1 (Figure 3.5), the waveforms are strongly dependent on the inclusion concentration. With 10% concentration dispersion is already pronounced and the seismogram still contains all the frequencies. The high frequency wave at time zero is the strongest

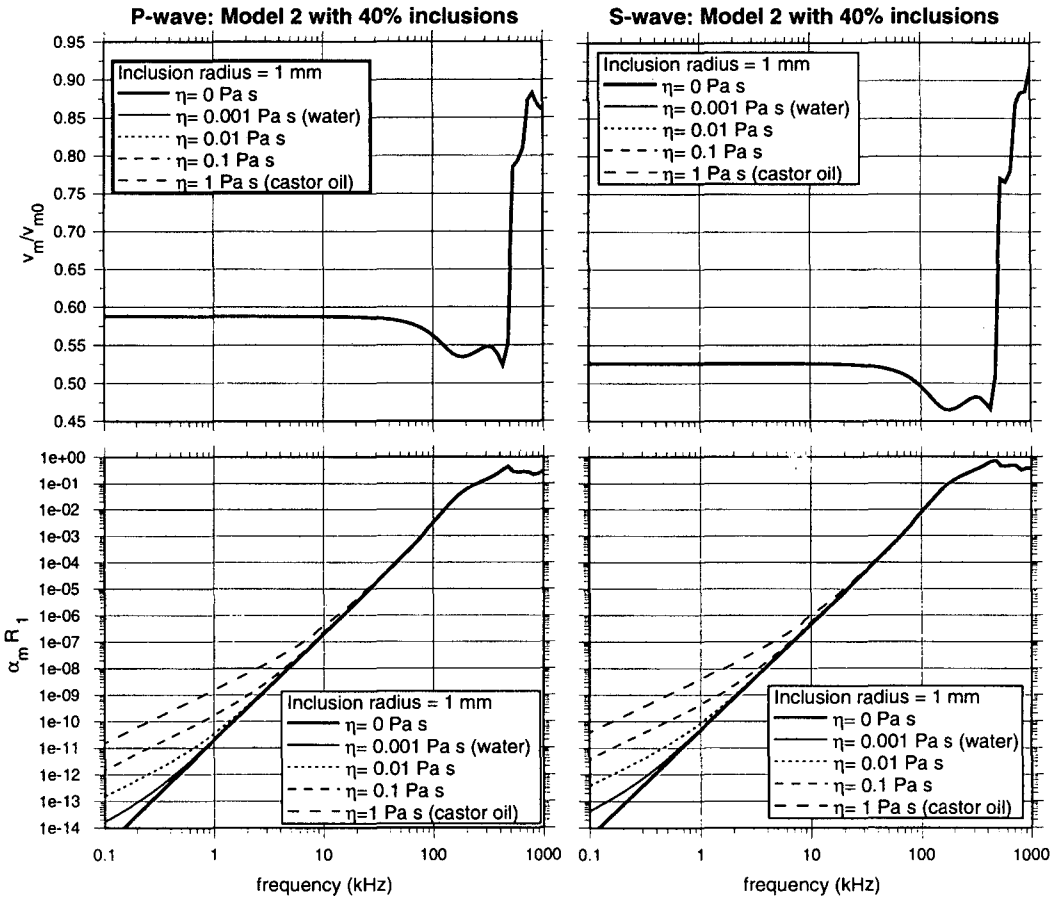

Figure 3.11: Similar to Figure 3.10 for Model 2 with 40% inclusions.

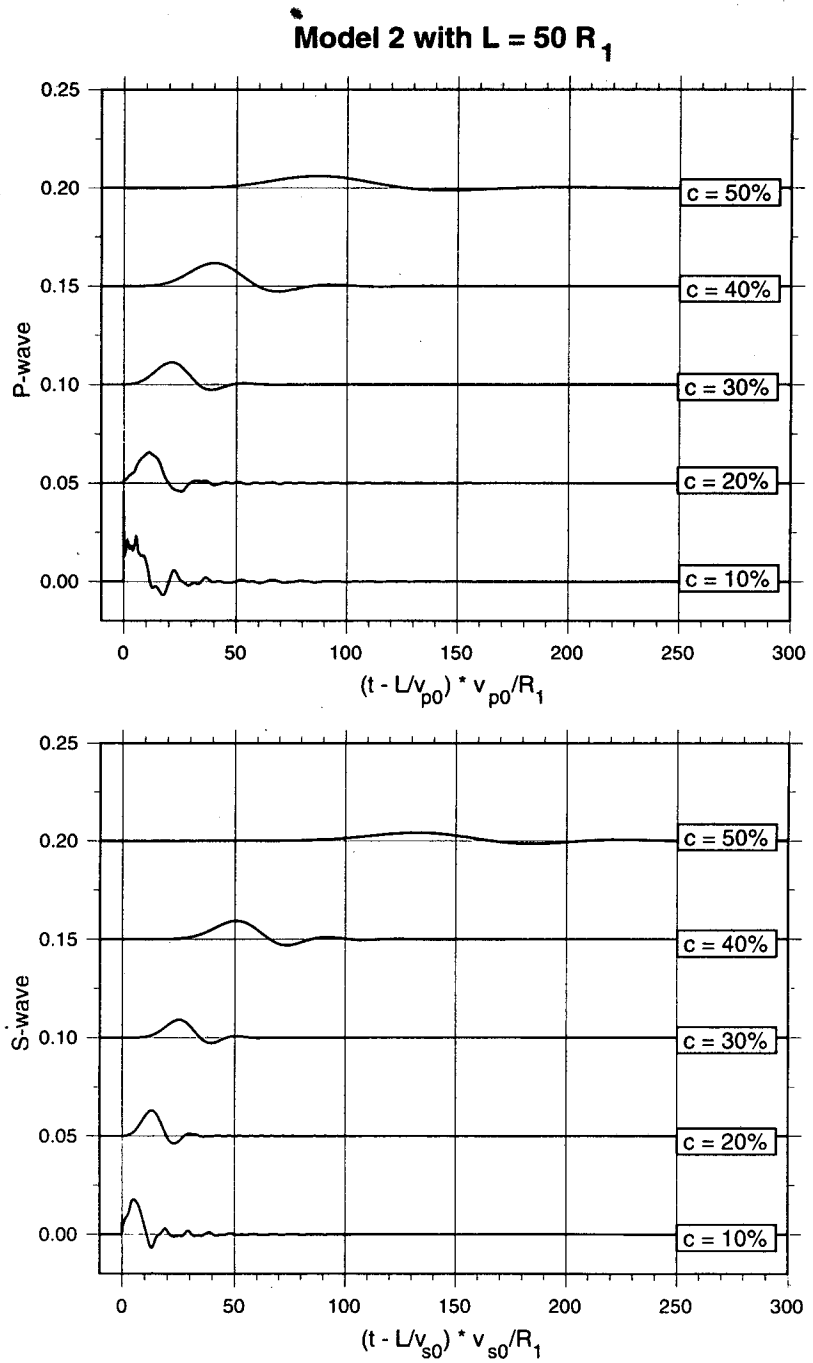

Figure 3.12: Similar to Figure 3.5 for Model 2 with $R_1 = 1$ mm inclusion radius and $L = 50\ R_1$ propagation distance.

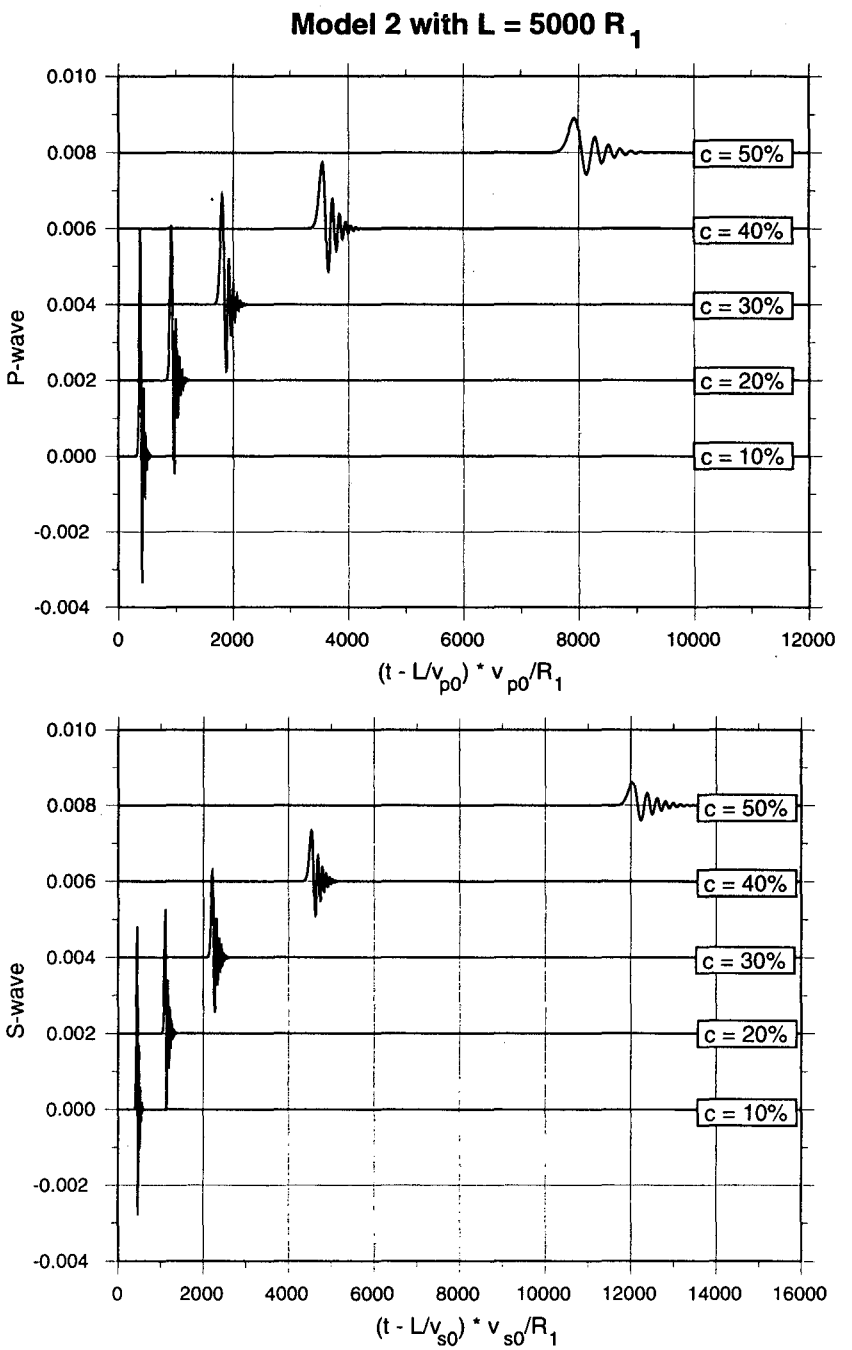

Figure 3.13: Similar to Figure 3.6 for Model 2 with $R_1 = 1$ mm inclusion radius and $L = 5000\ R_1$ propagation distance.

wave followed by waves with lower frequencies. With increasing inclusion concentration the high frequency wave is attenuated and the slower low frequency waves become dominant. With 50% concentration the wavelet has widened and the amplitudes have decreased. With L = 5000 R_1 propagation distance, the differences between the different concentrations become even more pronounced (Figure 3.13). Travel time as a function of concentration is strongly nonlinear and all the wavelets show strong dispersion.

3.7 Discussion and conclusions

We have modeled the coherent part of the wave field propagating in an isotropic medium with randomly distributed three-dimensional inclusions by the scattering function of the individual inclusions. Analogous to the one-dimensional media, we have derived self-consistent wavenumbers for media with large numbers of inclusions and arbitrary impedance contrast. The special case of spherical inclusions has been used to gain more insight into the elastic properties of media with three-dimensional inclusions. The calculations have shown that the exact scattering functions are required to adequately describe wave propagation at all frequencies. The properties of P-waves and S-waves are strongly dependent on the normalized frequency $k_m R$, i.e., they are dependent both on frequency and inclusion size.

At low frequencies ($k_m R < 0.1$), the dynamic composite elastic medium the-

ory is consistent with Berryman's results. The phase velocity depends on the inclusion concentration only, whereas the attenuation also depends on the inclusion size. At higher frequencies the scattering functions become more complex and there exists no simple power law frequency dependence. This might explain the frequently observed scale problem between measurements at exploration frequencies (~100 Hz), logging frequencies (~10 kHz) and laboratory frequencies (~1 MHz). Furthermore, we have shown that the coherent signal is not confined to one cycle. Because dispersion becomes very pronounced in media with three-dimensional inclusions, data analysis must be performed on full waveforms to obtain correct results.

The analysis of liquid inclusions has demonstrated that viscous damping is generally smaller than scattering attenuation due to spherical pores for the parameters used. Fluid viscosity may become important only if the normalized frequency $k_m R$ is very small or if the impedance contrast between matrix and inclusion is small. Non-linear fluid flow due to large displacements within the solid matrix may also be important and requires further investigation. However, a recent study of laboratory measurements on sand samples with different viscous fluids has shown no significant effect on ultrasonic waves (Seifert et al., 1998).

Chapter 4

Seismic rock properties of partially water saturated tuffs in the Yucca Mountain region derived from well logs and VSP data

4.1 Abstract

We have analyzed VSP data of partially water saturated tuffs in the Yucca mountain region. The tuffs are generally poorly to moderately consolidated and show porosities between 10% and 70%. We found that the VSP velocities can be explained by combining self-consistent theories for pores and cracks. The parameters needed for the calculations are porosity, pore water saturation, bulk density and mineral composition. All these parameters are commonly obtained in well logs and no further microstructural information is needed. The effective matrix velocities in the studied tuffs deviate strongly from the uncracked matrix velocities. In our interpretation, this effect is due to the presence of two dimensional inhomogeneities like cracks and mineral contacts. The strongest

manifestation of this effect was found in one of the vitric zones, where the matrix velocities are reduced by about 50%. The theoretical model used is suitable for poorly to moderately consolidated sediments and large porosities, if the long wavelength assumption is fulfilled.

4.2 Introduction

Seismic waves are widely used in the oil industry to investigate rock properties (e.g., Gregory, 1977; Wang and Nur, 1992; Winkler and Murphy III, 1995). Seismic measurements are important in environmental projects in the shallow subsurface. Unfortunately, most of the theories developed by the oil industry provide unreliable results at shallow depths. It has been generally accepted that the low effective pressure environment and poor consolidation are mainly responsible for this failure (e.g., Gregory, 1977; Dvorkin and Nur, 1996). Extensive theoretical work has been done in the past to explain seismic velocities in porous media (e.g., Gassmann, 1951; Biot, 1956a; Biot, 1956b; Kuster and Toksöz, 1974; Berryman, 1980a; Berryman, 1980b; Dvorkin et al., 1995; Bryant and Raikes, 1995). Most of these theories require microstructural information or broad frequency band data, which are generally not available. In this study we present a new approach to predicting of seismic velocities in porous media by using *in situ* measurements only. The theory for spherical inclusions by Berryman (1980a) and the theory for cracked solids by O'Connell and Budi-

ansky (1974) are combined to calculate the seismic velocities of porous media. The parameters needed are porosity, pore water saturation, bulk density, mineral composition and seismic velocities of the minerals. All these parameters are commonly obtained in well logs and VSP (Vertical Seismic Profiling) measurements. We use this information to calculate the effective matrix velocities, which are generally smaller than the mineral velocities due to low pressure environment and imperfections of the minerals.

We apply our approach to partially saturated tuffs in the Yucca mountain region in the southwestern part of Nevada, which is currently being evaluated as a potential site for a nuclear waste repository. The zone of interest consists mainly of partially saturated thick tuff layers (Nelson and Anderson, 1992), which show variable degrees of welding and diagenetic alterations (Broxton et al., 1987).

4.3 Long wavelength theory for seismic velocities in porous media

At low frequencies, seismic velocities of porous materials are determined by the solid matrix and the pore fluid. In low effective pressure environments one has to consider mineral contacts and possible cracks within the solid matrix. We want to use the most general theories to describe pores and cracks, which are much smaller than the wavelength of the seismic waves. Several studies have

shown that for high porosities only the self-consistent theories are applicable (e.g., Berge et al. 1995). In the following we will use the classical theory for cracks by O'Connell and Budiansky (1974) and Berryman's theory for spheres (1980a) to calculate the seismic velocities of porous media. Both theories are self-consistent and valid only if the wavelength of the displacement field is large compared to the pore and crack size.

In general, porous media consist of different minerals. If the grain boundaries are perfectly tied together and the minerals are perfect crystals the bulk modulus K_s, shear modulus μ_s and density ρ_s of the solid matrix can be calculated using Berryman's (1980a) self-consistent theory:

$$\begin{aligned} \frac{1}{K_s + \frac{4}{3}\mu_s} &= \sum_{i=1}^{n} \frac{(c_s)_i}{(K_s)_i + \frac{4}{3}\mu_s} \\ \frac{1}{\mu_s + F_s} &= \sum_{i=1}^{n} \frac{(c_s)_i}{(\mu_s)_i + F_s} \\ F_s &= \frac{\mu_s}{6}\left(\frac{9K_s + 8\mu_s}{K_s + 2\mu_s}\right) \\ \rho_s &= \sum_{i=1}^{n} (c_s)_i (\rho_s)_i, \end{aligned} \tag{4.1}$$

where $(K_s)_i$, $(\mu_s)_i$, $(\rho_s)_i$ and $(c_s)_i$ are the bulk modulus, shear modulus, density and relative volume concentration of each different mineral (Figure 4.1a). In reality, the minerals in porous media are usually not perfect crystals. Since these imperfections have approximately zero volume, they will not be considered as pores. One simple way to include their effect on the seismic velocity is to introduce cracks with zero volume into the solid matrix (Figure 4.1b). O'Connell

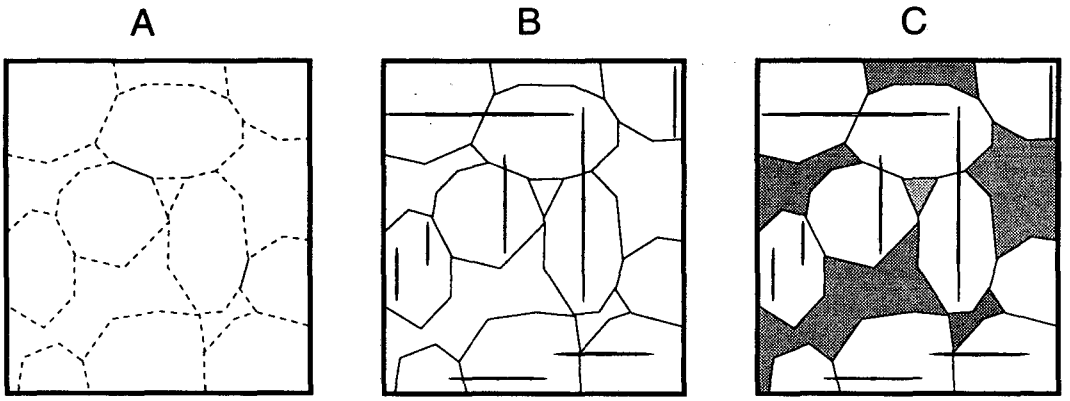

Figure 4.1: Schematic outline of the theory. Step A: Calculation of the uncracked matrix. Step B: Introducing grain boundaries and cracks into the matrix. Step C: Introducing pores and porefluids.

and Budiansky formulated the effect of cracks in a solid matrix and calculated the effective bulk modulus $\tilde{K}_s$ and shear modulus $\tilde{\mu}_s$ of the cracked solid for different shapes of cracks. They concluded that the shape of the cracks does not change the moduli significantly. Hence, the fluid saturation of the cracks ξ and the crack density ϵ are the only two parameters needed to describe a cracked solid. The number of cracks is defined by the crack density

$$\epsilon = \frac{2N}{\pi} < \frac{A^2}{P} >, \tag{4.2}$$

where N is the number of cracks per unit volume, A is the area and P the perimeter of the cracks, respectively. The effective moduli of the cracked solid are

$$\begin{aligned} \frac{\tilde{K}_s}{K_s} &= 1 - \frac{16}{9}\left(\frac{1-\tilde{\nu}_s^2}{1-2\tilde{\nu}_s}\right)(1-\xi)\,\epsilon \\ \frac{\tilde{\mu}_s}{\mu_s} &= 1 - \frac{32}{45}(1-\tilde{\nu}_s)\left(1-\xi+\frac{3}{2-\tilde{\nu}_s}\right)\epsilon \end{aligned} \tag{4.3}$$

$$\epsilon = \frac{45}{16}\left(\frac{\nu_s - \tilde{\nu}_s}{1-\tilde{\nu}_s^2}\right)\frac{(2-\tilde{\nu}_s)}{[(1-\xi)(1+3\nu_s)(2-\tilde{\nu}_s)-2(1-2\nu_s)]},$$

where ν_s is the Poisson ratio of the uncracked matrix and $\tilde{\nu}_s$ of the effective matrix. The density is not affected by cracks, since the cracks have approximately zero volume.

Finally the effect of the porespace itself has to be considered (Figure 4.1c). For pores with different fluids, the bulk modulus K_f of the fluid mixture within the pores can be calculated by the Reuss average (Reuss, 1929), the shear modulus μ_f is zero and the density ρ_f is the volumetric average of the individual components

$$\begin{aligned} \frac{1}{K_f} &= \sum_{i=1}^{m}\frac{(c_s)_i}{(K_f)_i} \\ \mu_f &= 0 \\ \rho_f &= \sum_{i=1}^{m}(c_f)_i(\rho_f)_i, \end{aligned} \tag{4.4}$$

where $(K_f)_i$, $(\rho_f)_i$ and $(c_f)_i$ are the bulk modulus, density and relative volume concentration of each different fluid. Assuming the pores have approximately spherical shape, Berryman's theory can be used to calculate the effective bulk modulus K, shear modulus μ and density ρ of the porous medium

$$\begin{aligned} \frac{1}{K+\frac{4}{3}\mu} &= \frac{1-\phi}{\tilde{K}_s+\frac{4}{3}\mu}+\frac{\phi}{K_f+\frac{4}{3}\mu} \\ \frac{1}{\mu+F} &= \frac{1-\phi}{\tilde{\mu}_s+F}+\frac{\phi}{F} \\ F &= \frac{\mu}{6}\left(\frac{9K+8\mu}{K+2\mu}\right) \\ \rho &= (1-\phi)\rho_s+\phi\rho_f, \end{aligned} \tag{4.5}$$

where ϕ is the total porosity. It has to be pointed out that none of the governing equations contains any information about the dimensions of the pores or crack sizes, i.e., the relative volume concentrations are important only.

4.4 Application for partially water saturated tuffs

4.4.1 Log data and VSP data

The theory described above is used to calculate the effective matrix velocities in partially saturated tuffs in the Yucca mountain region at well UZ16. Several logs (Lugo, 1993) and a zero offset VSP survey (Balch and Erdemir, 1996) were available for the analysis. The log data consist of porosity, water saturation and density measurements every 0.15 m (0.5 ft). The VSP survey was conducted with three component receivers, placed every 4.9 m (16 ft) between 29 m (95 ft) and 492 m (1615 ft) depth. The maximum frequency of the seismic waves varies between 40 and 100 Hz. P- and S-wave interval velocities were derived from the phase difference of the first arrivals between two adjacent receivers. For this purpose the first arrival in the seismic trace was interpreted as the direct wave from source to receiver. We transformed both signals into the frequency domain and determined the low frequency velocity in the appropriate frequency range. Figure 4.2 shows all the log and VSP data, which were used in the following analysis. The profiles are divided into lithological units which are significantly different from each other (Geslin et al., 1994). It turns out that there are four

Table 4.1: Seismic velocity, Poisson ratio and density of the important minerals in UZ16.

Mineral	v_p (m/s)	v_s (m/s)	ν	ρ (kg/m^3)	Reference
Fused Quartz	5600	3600	0.15	2200	Carmichael, 1982
K-Feldspar	5880	3050	0.32	2570	Anderson, 1989
Glass	5850	3250	0.28	2300	Johnson and Plona, 1982
Zeolite	6110	3530	0.25	2300	Carmichael, 1982

major groups in UZ16: lithophysal (L), vitric (V), zeolitic (Z) and welded (W) zones.

An analog mineral log was available to provide the approximate mineral composition in all the lithological units. The four important minerals are fused quartz, K-feldspar, glass and zeolite. The elastic properties of these minerals are listed in Table 4.1. Comparing the matrix densities derived from the logs with the mineral densities, a more accurate mineral composition log was constructed, which was used to calculate the uncracked matrix velocities in each interval. Table 4.2 shows the average mineral composition and its variation in each lithological unit.

4.4.2 Calculations

The data described above provide almost all the information needed to calculate the theoretical seismic velocities. The only undefined parameters are the crack density and the water saturation in the cracks. Using the VSP velocities

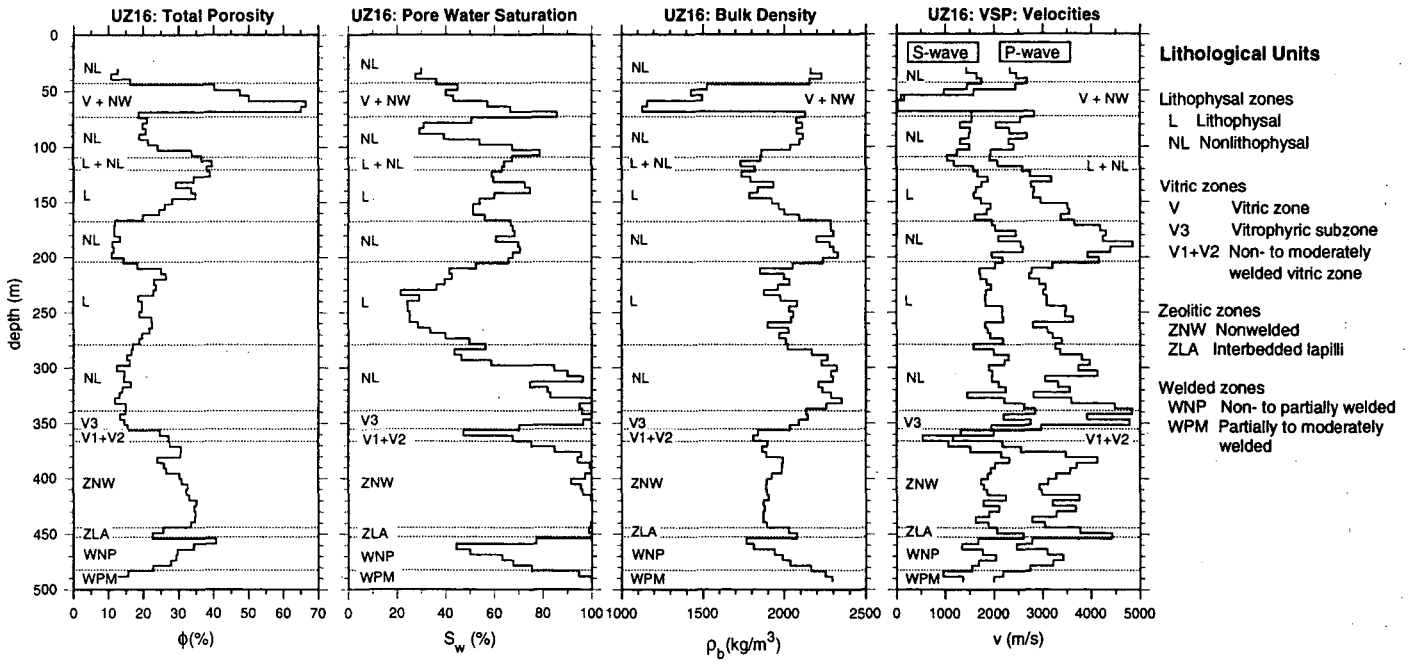

Figure 4.2: Interval measurements of porosity, pore water saturation, bulk density, P-velocity and S-velocity. The lithological identifications were obtained from Geslin et al. (1994).

Table 4.2: Average volume concentrations and one standard deviation of the different minerals in UZ 16.

Lithologic unit	Fused Quartz (%)	K-Feldspar (%)	Glass (%)	Zeolite (%)
Lithophysal zone	25 ± 36	75 ± 36	-	-
Vitric zone	37 ± 12	9 ± 32	54 ± 19	-
Zeolitic zone	15 ± 1	20 ± 6	-	65 ± 5
Welded zone	15 ± 16	85 ± 16	-	-

together with equation (4.5) we can solve two equations for the crack density ϵ and the water saturation in the cracks ξ, defined in equation (4.3). Equation (4.5) can therefore be solved in each depth interval for ϵ and ξ. In general, the solution will not be exact, since there are uncertainties in our measurements and phase analysis, but the theoretical approach will find the best physically correct solution under the assumption of our model. Hence, we have to expect a slight misfit between real data and theoretical estimates. The results for the smallest misfit for P- and S-velocities are shown in Figure 4.3.

The fit of the VSP velocities is generally very good, except for the first vitric and nonwelded zone (42.8 - 72.5 m). The calculations predict much smaller velocities due to the high porosity in this zone. For porosities larger than about 60% the calculated shear velocity actually vanishes since there are no grain contacts left according to the model of spherical pores. However, the measured porosity in the bedded tuffs exceeds 60%, but at the same depth the VSP velocities show no change. There are different explanations for this disagreement:

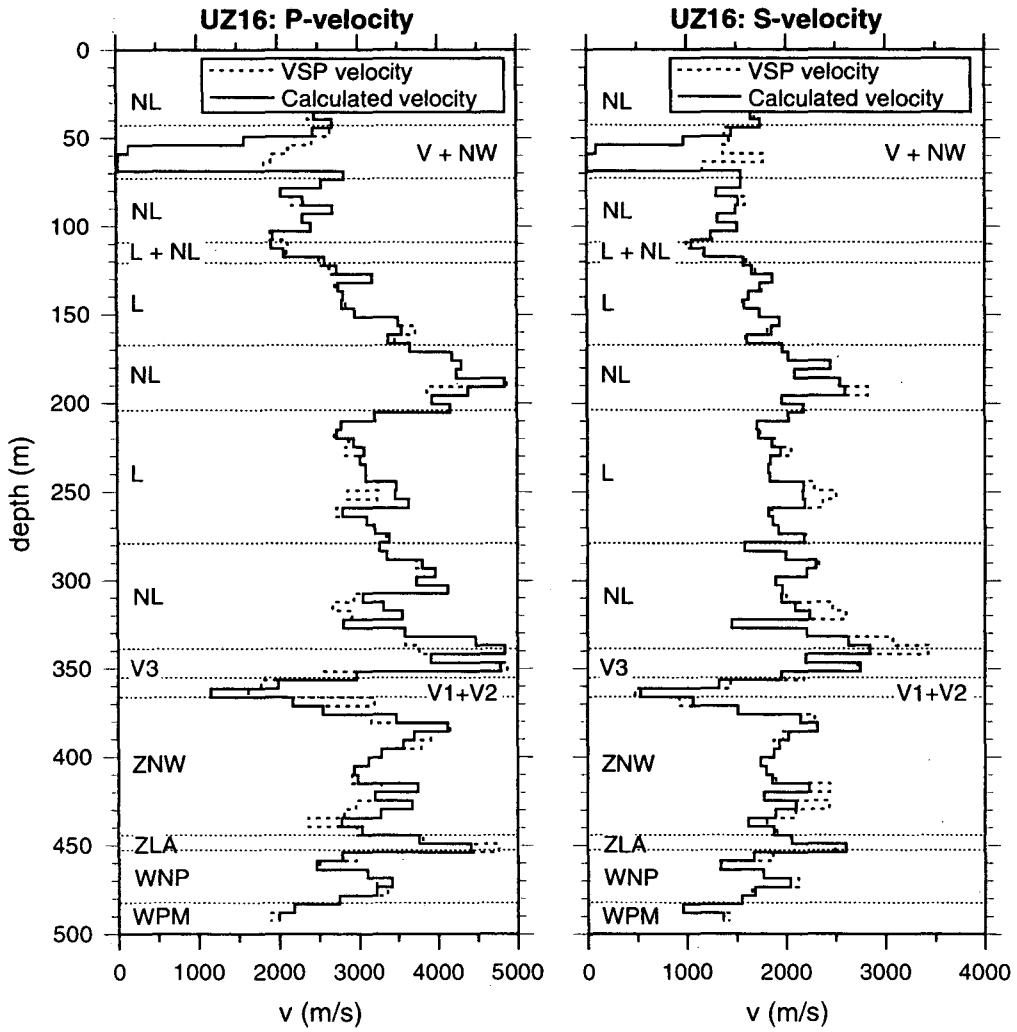

Figure 4.3: Comparison of measured VSP-velocities and calculated velocities.

1. The log data overestimate the actual porosity.

2. The large porosity is only a local effect and the seismic waves find a fast path.

The velocities of the uncracked matrix, the calculated crack densities, crack water saturations and effective matrix velocities are shown in Figure 4.4. As discussed above, the first 72 m can not be explained by our model and have to be disregarded. The effective matrix velocities are relatively smooth within the units, but show sharp changes at the unit boundaries. The crack density varies between 0.3 and 0.6 all the way down to about 330 m depth. In the vitrophyric subzone (V3) the value drops to 0.1 and reaches a maximum of about 1.1 in the nonwelded vitric zone (V1+V2). Such large crack densities have a strong effect on the effective matrix velocities. In the nonwelded vitric zone the P- and S-velocities of the matrix drop below 3500 m/s and 1200 m/s, respectively. But P- and S-velocities sometimes show quite different behaviors. For instance, between 120 and 340 m the matrix S-velocity remains relatively unchanged, but the P-velocity shows a sharp change at about 200 m depth, which results in a large change of the Poisson ratio. Figure 4.4 shows that this change is mainly due to smaller water saturation in the cracks, whereas the crack density does not change. Figure 4.5 shows the Poisson ratio as a function of depth, which illustrates in a more pronounced form the different behavior of P and S-velocities.

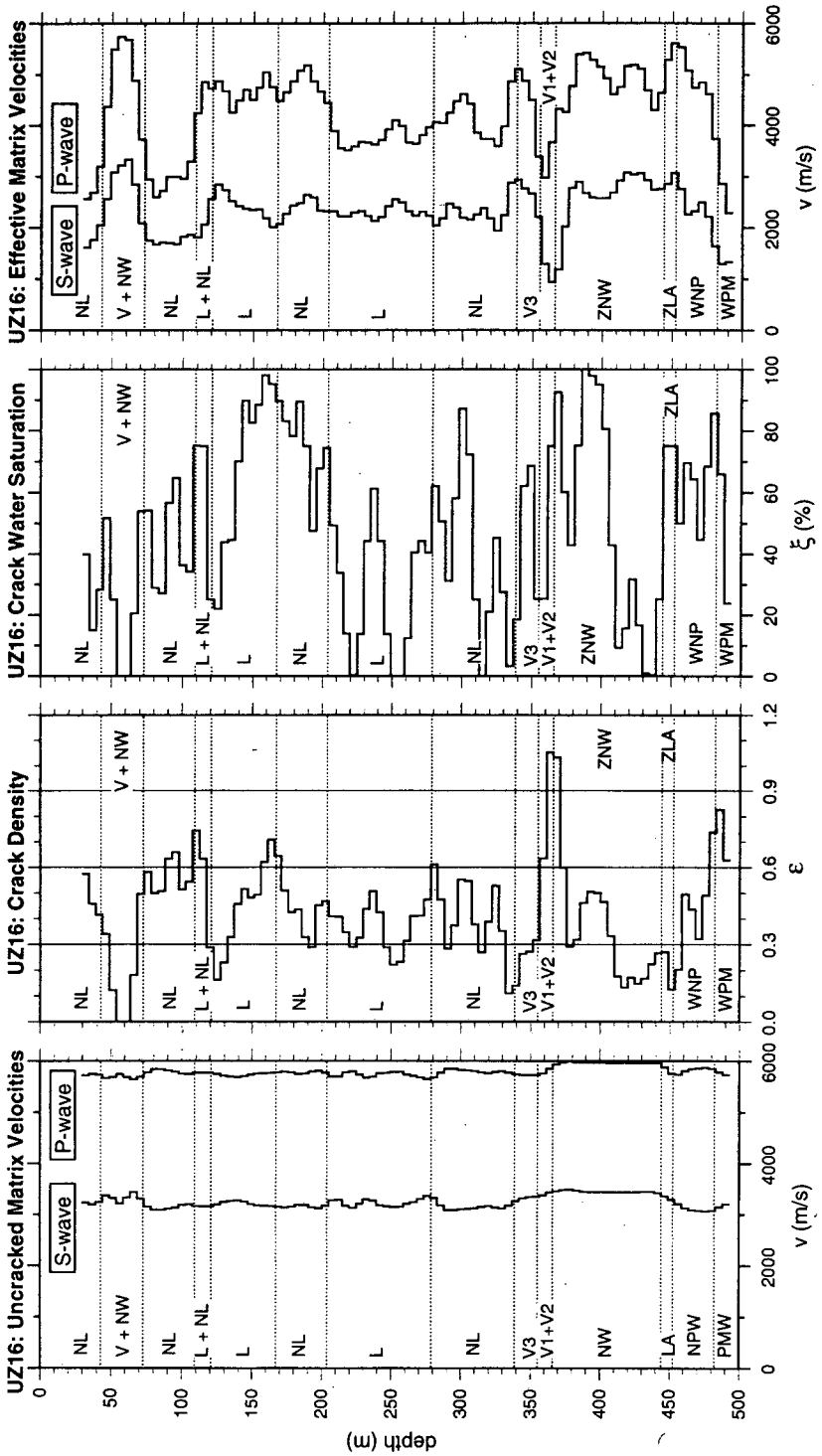

Figure 4.4: Velocities of the uncracked matrix and calculated crack densities, crack water saturations and effective matrix velocities.

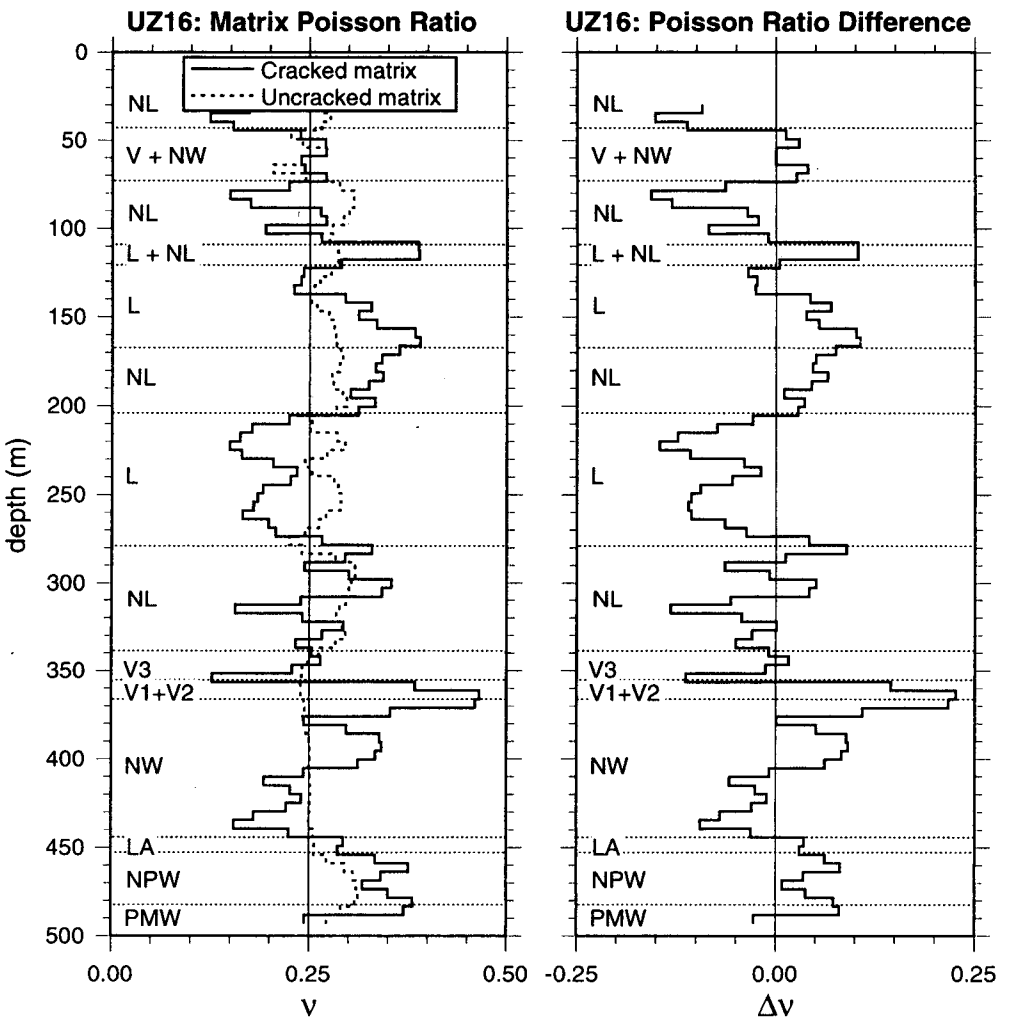

Figure 4.5: Poisson ratio of the uncracked and cracked matrix.

4.5 Discussion

The presented method explains seismic velocities accurately, as long as the porosity is smaller than about 60%. In this case the correct seismic velocities and information about the matrix properties can be obtained. For larger porosities Berryman's theory for spherical inclusions is probably not appropriate. The analysis has shown that in partially water saturated tuffs the matrix properties vary significantly over short distances. Simple seismic velocity-to-porosity relationships are therefore not appropriate in this environment. In contrast to empirical relationships the presented method always yields physically correct results within the limits of the model assumptions and the measured data do not have to be smoothed for the analysis.

It has to be noted that none of the effective matrix parameters shows a simple correlation with porosity, pore water saturation or bulk density. This indicates that the approach used separates the properties of the matrix and of the pores in an effective way. For instance, the extreme changes of the seismic velocities in the vitric zone are due to changes of the matrix velocities and not due to changes in porosity or pore water saturation. The reason for these abrupt changes is most likely the diagenetic or tectonic history. Using a similar modeling approach Berge et al. (1995) did not infer a significant number of cracks in fused glass beads, consistent with direct observations. We suspect that the cooling history and the variety of minerals with different thermal properties will alter the matrix

in a specific way. We also found that the volume concentration of the minerals is not critical in the studied tuffs. The velocity of the uncracked matrix shows relatively little variation compared to the effective matrix velocities (Figure 4.4).

Before using the presented method for other data one has to carefully examine the scale problem. If gaseous phases are present in the pores, the seismic velocity within the pores can be as small as 25 m/s, as one can see by examining equation (4.4). If the seismic frequencies are in the kHz range, the smallest wavelengths are only on the order of centimeters. Such slow velocities are rather common in marine seismology and have been studied in great detail (e.g., Anderson and Hampton, 1980). The long wavelength assumption is fulfilled for the presented data since the frequencies are always smaller than 100 Hz and the corresponding smallest wavelengths are in the order of tens of centimeters. However, frequencies in the kHz range may violate the long wavelength assumption and Berryman's theory has to be replaced by a more general theory. For instance, sonic logs which commonly use frequencies larger than 10 kHz may only be used with caution for a similar analysis since the smallest wavelengths are on the order of millimeters.

4.6 Conclusions

We find that the VSP velocities in partially saturated tuffs can be explained by combining self-consistent theories for pores and cracked matrix material. If

the long wavelength assumption is fulfilled no microstructural information is required. To derive the velocity of the cracked matrix, *in situ* measurements of porosity, pore water saturation, bulk density, mineral composition and mineral velocities are needed. It turns out that the volume concentration of the minerals is not critical in the studied tuffs. The major changes are probably due to cracks and mineral contacts. The presented method separates the matrix and pore properties in an efficient way if the pore and crack sizes are much smaller than the seismic wavelength. In this case the presented approach is very suitable for poorly to moderately consolidated sediments. Further studies have to be conducted to investigate the effect of smaller wavelengths, which are common in high resolution seismic surveys and laboratory measurements.

Chapter 5

Using seismic crosswell surveys to determine the aperture of partially water-saturated fractures

5.1 Abstract

An air injection experiment in a shallow fractured limestone at Conoco's borehole test facility near Newkirk, Oklahoma has shown large effects on the amplitude, but small effects on the travel time of the transmitted seismic waves. We have analyzed data from a seismic monitor survey in the kilohertz range performed during the experiment and have modeled the fracture zone as a single fracture. The large amplitude decrease during the experiment is mainly due to the impedance contrast between the small velocities of gas-water mixtures inside the fracture and the formation. The intrinsic attenuation of the fracture fluid seems to be a second order effect for small apertures. During the experiment the seismic wavelengths inside the fracture become comparable to the aperture

dimension, which allows an estimation of fracture apertures. We also have analyzed a crosswell survey acquired shortly after the experiment and computed aperture and gas concentration profiles. Our aperture estimates range from less than one millimeter to a few millimeters, which is comparable to previous tracer tests. The results of this study are generally consistent with prior hydrologic work and single well surveys. This study demonstrates that crosswell surveys are an effective tool for obtaining *in situ* estimates of fracture aperture and gas concentration.

5.2 Introduction

When present, fractures can play a dominant role in fluid transport in the shallow subsurface. In the oil industry, fractures are important as reservoirs and high permeability flow paths. In environmental applications, knowledge about fracture location and properties in the subsurface helps to contain contaminants. The Berkeley National Laboratory has an ongoing effort, in cooperation with Conoco and Amoco, to characterize fractured heterogeneous media. A series of joint seismic and well-test field experiments have been conducted at Conoco's Newkirk, Oklahoma, Borehole Test Facility (Majer et al., 1996). Pump tests showed good hydraulic connections between some of the wells, which indicated a local fracture zone (Datta-Gupta et al., 1994). An air injection experiment was carried out in 1994 to seismically image this fracture zone (Majer et al., 1997).

A monitor survey during the experiment showed large amplitude changes which have been interpreted as an indication of air entering the fracture zone. From single well surveys, the position of the fracture zone was determined and later verified by slant well drilling (Majer et al., 1997). From core analysis and single well surveys Majer et al. (1997) inferred a single vertical fracture perpendicular to the crosswell survey analyzed in this study.

The purpose of our analysis is to explain quantitatively the effects of the air injection experiment on the seismic waves and to obtain air concentration and aperture estimates from crosswell surveys. In the following we use the *a priori* information and represent the fracture as a single vertical fluid layer with variable air concentration. To invert the seismic data for the fracture aperture and air concentration inside the fracture, we developed an inversion scheme which is then applied to the seismic monitor survey. The same scheme is also applied to a crosswell survey acquired shortly after the air injection to obtain aperture and air concentration profiles.

5.3 Theory

5.3.1 Effect of a single vertical fracture on seismic waves

Majer et al. (1997) have shown that a single vertical fracture lies perpendicular to the analyzed crosswell surveys. Given aperture d, velocity v and density ρ of the fluid inside the fracture and a normally incident plane P-wave $u_0(t)$,

the transmitted P-wave u[t,(v,ρ),d] can be written as (Aki and Richards, 1980)

$$u\left[t,(v,\rho),d\right] = u_0(t) * \left(1-R^2\right) * \left[\delta\left(t-\frac{d}{v}\right) + R^2\delta\left(t-\frac{3d}{v}\right) + ...\right] \quad (5.1)$$

$$R = \frac{\rho v - (\rho v)_{formation}}{\rho v + (\rho v)_{formation}},$$

where R is the reflection coefficient between formation and fracture fluid, δ(t) is the unit impulse function and the star symbol denotes the convolution. In the frequency domain, equation (5.1) becomes

$$U\left[\omega,(v,\rho),d\right] = \left(1-R^2\right)\frac{e^{-i\frac{\omega}{v}d}}{1-R^2e^{-i\frac{2\omega}{v}d}}U_0(\omega) = G\left[\omega,(v,\rho),d\right]U_0(\omega), \quad (5.2)$$

where U and U_0 are the spectra of u and u_0, respectively. G[ω,(v,ρ),d] represents Green's function of a fracture with given velocity v, density ρ and aperture d. The effect of intrinsic attenuation of the fluid can be included by adding the appropriate imaginary part to the fluid velocity (Aki and Richards, 1980).

During the air injection experiment, an air compressor rated at 345 kPa was used to inject air into the fracture (Majer et al., 1997). Assuming 23 kPa/m (1 psi/ft) parting pressure of the formation, the pressure inside the fracture was always kept below the parting pressure of the formation. Hence, we only have to consider a change in the fluid velocity and density inside the fracture (i.e., air-water mixtures), but not of the aperture. Using equation (5.2), the measured spectrum before the air injection U_{before} and the calculated spectrum after the air injection $\hat{U}_{after}$ can be written as

$$U_{before}\left[\omega,(v,\rho)_{before},d\right] = G\left[\omega,(v,\rho)_{before},d\right]S(\omega)\,I(\omega)\,L(\omega)\,U_0(\omega) \quad (5.3)$$

$$\hat{U}_{after}\left[\omega,(v,\rho)_{after},d\right] = G\left[\omega,(v,\rho)_{after},d\right] S(\omega)\, I(\omega)\, L(\omega)\, U_0(\omega),$$

where S(ω), I(ω) and L(ω) represent the effect of the source, receiver and site, respectively. These three effects remain unchanged during the experiment. Equation (5.3) can therefore be rewritten as

$$\hat{U}_{after}\left[\omega,(v,\rho)_{after},d\right] = \frac{G\left[\omega,(v,\rho)_{after},d\right]}{G\left[\omega,(v,\rho)_{before},d\right]} U_{before}\left[\omega(v,\rho)_{before},d\right] \quad (5.4)$$

$$\frac{G\left[\omega,(v,\rho)_{after},d\right]}{G\left[\omega,(v,\rho)_{before},d\right]} = \frac{1-R^2_{after}}{1-R^2_{before}} \frac{1-R^2_{before}e^{-i\frac{2\omega}{v_{before}}d}}{1-R^2_{after}e^{-i\frac{2\omega}{v_{after}}d}} \cdot e^{-i\omega\left(\frac{1}{v_{after}}-\frac{1}{v_{before}}\right)d}, \quad (5.5)$$

where R_{before} and R_{after} are the reflection coefficients before and after the air injection. In equation (5.5), the spectrum after the air injection is a function of the velocities and densities inside the fracture before and after the air injection, the aperture of the fracture and the measured spectrum before the air injection. The first term in equation (5.5) is the ratio of the squared transmission coefficients. The second term describes the sense of motion change due to reverberation inside the fracture and the third term is the time delay of the first transmitted wave due to the velocity change inside the fracture.

5.3.2 Seismic properties of air-water mixtures

In most studies of the seismic properties of air in water it is generally assumed that air exists in the form of spherical bubbles inside the fluid. Numerous observations have shown that the radii of air bubbles in natural waters range

between 1 μm to about 3000 μm (e.g., Anderson and Hampton, 1980). The acoustic properties can be divided into two different frequency ranges relative to the resonance frequency of the air bubbles. By neglecting the surface tension of an air bubble, the resonance frequency f_0 is (Minnaert, 1933)

$$f_0 = \frac{1}{2\pi r_0}\sqrt{\frac{3K_{air}}{\rho_{fluid}}}, \qquad K_{air} = \gamma p_0, \tag{5.6}$$

where r_0 is the air bubble radius, K_{air} the bulk modulus of air, ρ_{fluid} the density of the surrounding fluid, γ the ratio of specific heats and p_0 the ambient pressure. The ratio of specific heats for air is one for frequencies much smaller than the resonance frequency (i.e., isothermal pulsation) and 1.4 for frequencies much higher than the resonance frequency (i.e., adiabatic pulsation). Within the two frequency limits the ratio of specific heats lies between the isothermal and adiabatic limits (Devin, 1959).

Spitzer (1943) developed the theoretical background of the acoustic properties of gas bubbles in water for all frequencies, which has been confirmed by various laboratory measurements (e.g., Silberman, 1957). Beyond the resonance frequency the velocity of air-water mixtures equals the water velocity. The attenuation is extremely strong close to the resonance frequency and decreases to a smaller constant value at higher frequencies. At frequencies below the resonance frequency, the pulsation of the air bubble is approximately isothermal and the

velocity v can be calculated by Wood's equation (Wood, 1930)

$$\frac{1}{v} = \sqrt{\left[\frac{c}{K_{air}} + \frac{1-c}{K_{water}}\right]\left[c\rho_{air} + (1-c)\,\rho_{water}\right]} \tag{5.7}$$

$$K_{air} = p_0,$$

where c is the air concentration, K_{water} the bulk modulus of water, and ρ_{air} and ρ_{water} are the density of air and water, respectively. It is interesting to note that Wood's equation (Wood, 1930) is equivalent to the Reuss average (Reuss, 1929), which is commonly used in one-dimensional wave propagation. The attenuation in the low frequency range is dominated by thermal damping and increases proportional to the frequency squared (Devin, 1959; Eller, 1970).

During the experiment, the water table was on the average at about 7 m depth and the fracture fluid was unconfined. With the crosswell survey covering 14-30 m depth, this results in ambient pressures between 170 kPa and 330 kPa. Figure 5.1 shows the velocity of air-water mixtures as a function of air concentration for similar ambient pressures of 100, 200 and 300 kPa calculated with Wood's equation. Figure 5.1 shows clearly the strong effect of very small air concentrations, which lead to a drop in the velocities far below the velocities of the individual constituents. The minimum velocity is reached when the mixture consists of 50% air and 50% water. At 100 kPa pressure, the velocity inside the fracture can therefore vary between 1500 m/s and 20 m/s.

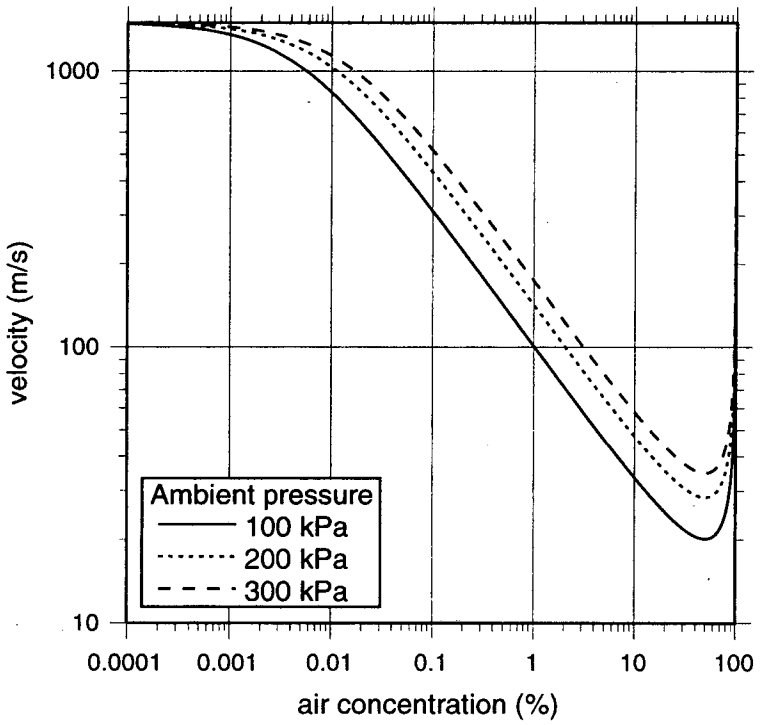

Figure 5.1: Velocity of air-water mixtures calculated with Wood's equation. Small amounts of air have a strong effect and the velocity can be smaller than the velocity of each individual constituent.

5.3.3 Example of a single fracture with 0.5 mm aperture

The effect of a partially water saturated single fracture on transmitted seismic waves is demonstrated in Figure 5.2. For the computation of the seismograms, we have used the same formation properties (velocity=3860 m/s, density=2450 kg/m^3) and ambient pressure (230 kPa) as in the observed monitor survey at receiver 1 (Figure 5.4) with 0.5 mm fracture aperture. Velocities and densities inside the fracture for different air concentrations are given in Table 5.1. Green's function obtained from equation (5.2) has been convolved with the initial signal of the monitor survey before the air injection. Table 5.1 shows that the transmission coefficient drops by almost two orders of magnitudes when air is injected into the fracture, but the travel time delay is less than 20 μs. Table 5.1 also shows that for large air concentrations, the seismic wavelength inside the fracture becomes comparable to the aperture.

Figure 5.2a shows that there are large amplitude changes due to the air-water mixtures inside a single fracture with only small changes in travel times. The modulus changes in Figure 5.2b are almost frequency independent, whereas the phase in Figure 5.2c shows significant frequency dependence at large air concentrations and high frequencies. Analysis of equation (5.5) demonstrates that it is capable of explaining these types of frequency behavior of modulus and phase. The modulus changes are mainly determined by the first term in equation (5.5), which describes the ratio of the squared transmission coefficients.

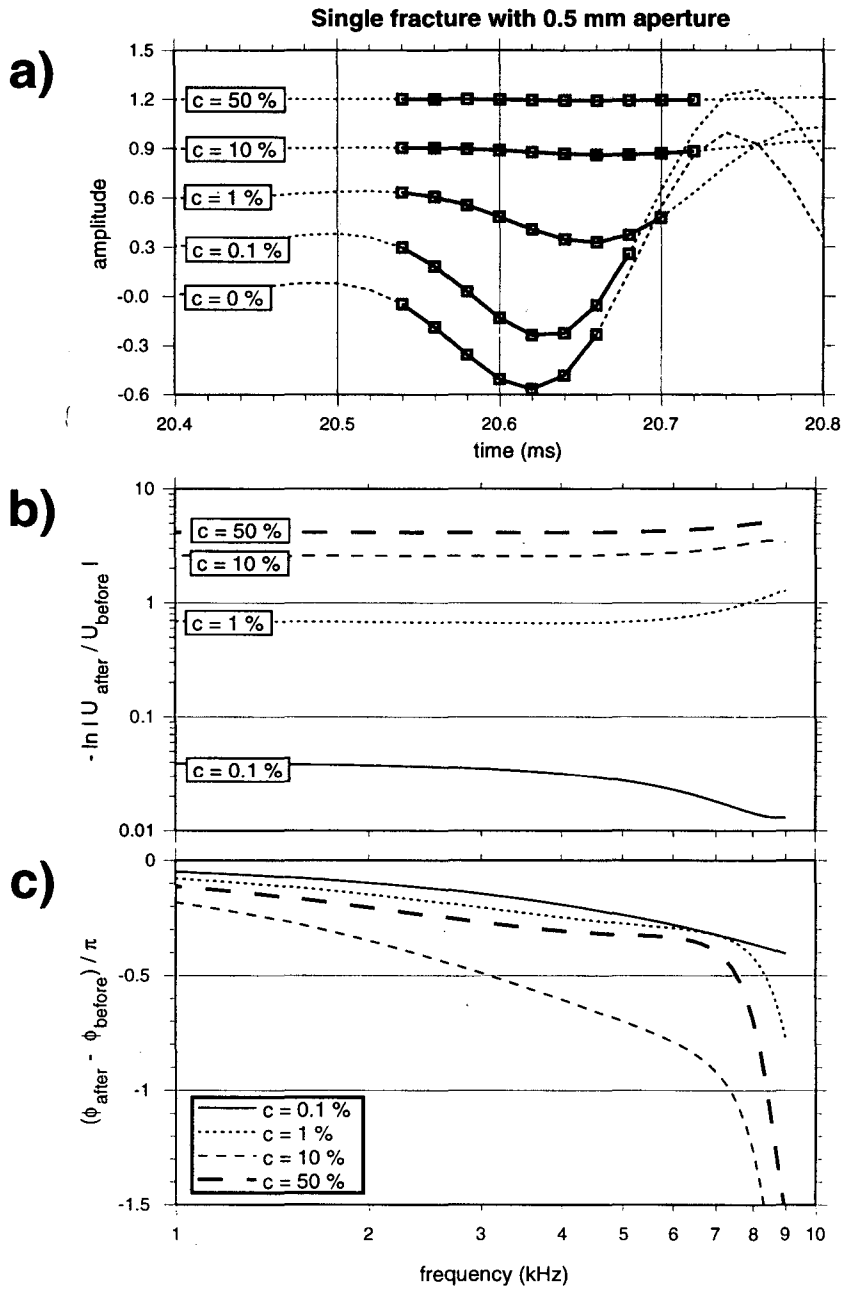

Figure 5.2: Example of seismic waves transmitted through a partially water saturated single fracture with 0.5 mm aperture. The ambient pressure inside the fracture is 230 kPa and the velocity and density of the formation are 3860 m/s and 2450 kg/m^3, respectively. These values are equal to the top receiver of the monitor survey (Figure 5.4). The solid lines and boxes show the time window, which was used to compute the spectra. a) shows the seismogram, b) the modulus changes and c) the phase changes for different air concentrations.

Table 5.1: Parameters for Figure 5.2. c is the air concentration, v the velocity and ρ the bulk density inside the fracture, dt the travel time delay of the first transmitted wave, λ the seismic wavelength, d = 0.5 mm the fracture aperture and f the frequency. The velocity v has been calculated with Wood's equation and 230 kPa ambient pressure. To calculate the reflection coefficient R between formation and fracture, we have used the same formation properties (velocity=3860 m/s and density=2450 kg/m^3) as in Figure 5.4.

c (%)	v (m/s)	ρ (kg/m^3)	dt(μs)	λ/d (f=5kHz)	(1-R^2) (%)
0	1500	1000	0.33	600	47
0.1	461	999	1.1	184	18
1.0	153	990	3.3	61	6.2
10	51.0	900	9.8	20	1.9
50	30.5	501	16	12	0.64

The phase changes at higher frequencies are due to the reverberations inside the partially saturated fracture, described by the second term in equation (5.5). Furthermore, if the frequency dependence of the phase is strong enough, as it is for high frequencies and large concentrations in Figure 5.2c, then the effects of velocity and aperture can be separated. From this we conclude that the inversion for apertures is only reliable if the velocity inside the fracture is small enough and the seismic wavelengths become comparable to the aperture. We found that the velocity inside the fracture must drop below 100 m/s before apertures in the millimeter range can be resolved.

5.4 Inversion method

5.4.1 Windowing the direct wave

Seismograms consist of different waves which have to be identified and extracted by windowing before equation (5.5) can be applied. In general, the arrivals can never be sorted out perfectly because they often represent a superposition of waves with different travel paths. In crosswell surveys the direct wave is a clean arrival only if it is the fastest wave on the seismogram. Hence, we have applied the following procedure in our analysis. First we have identified the direct wave before the air injection and defined the time t_0 at the maximum amplitude. We have centered a time window W with length a_m at t_0 and applied this window to the measured signal before u_{before} and after the air injection u_{after} to compute the observed changes due to the air injection. From equation (5.5), we know that the fracture delays the first transmitted wave by $dt=(1/v_{after}-1/v_{before})d$. Thus, we have centered the same time window W at t_0+dt and applied it to the measured signal after the air injection u_{after} and the calculated signal $\hat{u}_{after}$, as follows

$$
\begin{aligned}
u_{before}^{<a_m,0>}(t) &= u_{before}(t)\,W\left[\frac{t-t_0}{a_m}\right] \qquad (5.8)\\
u_{after}^{<a_m,0>}(t) &= u_{after}(t)\,W\left[\frac{t-t_0}{a_m}\right]\\
u_{after}^{<a_m,dt>}(t) &= u_{after}(t)\,W\left[\frac{t-(t_0+dt)}{a_m}\right]\\
\hat{u}_{after}^{<a_m,dt>}(t) &= \hat{u}_{after}(t)W\left[\frac{t-(t_0+dt)}{a_m}\right],
\end{aligned}
$$

where the calculated signal $\hat{u}_{after}$ is the Fourier inverse transform of $\hat{U}_{after}$ (equation (5.5)). In a last step, we have transformed all the windowed arrivals into the frequency domain, where we defined the objective function for the inversion. Since we have chosen the windows for the measured and the calculated signals to be exactly the same, we consider the effect of the time window on the objective function to be small. Performing the inversion in the frequency domain has the advantage of using an appropriate frequency range and, more importantly, to give adequate weight to the higher frequencies.

5.4.2 Defining the objective function

After windowing the measured and calculated signals, we can compute their spectra and express the observed changes Z_n and the difference between the estimated and measured spectra z_n at a given frequency ω_n as follows

$$\begin{aligned} Z_n^{<a_m,0>} &= \mid U_{before}^{<a_m,0>}(\omega_n) - U_{after}^{<a_m,0>}(\omega_n) \mid^2 \quad (5.9) \\ z_n^{<a_m,dt>}\left[(v,\rho)_{before},(v,\rho)_{after},d\right] &= \mid \hat{U}_{after}^{<a_m,dt>}(\omega_n) - U_{after}^{<a_m,dt>}(\omega_n) \mid^2, \end{aligned}$$

where $U_{before}^{<a_m,0>}$, $U_{after}^{<a_m,0>}$, $U_{after}^{<a_m,dt>}$ and $\hat{U}_{after}^{<a_m,dt>}$ are the spectra of $u_{before}^{<a_m,0>}$, $u_{after}^{<a_m,0>}$, $u_{after}^{<a_m,dt>}$ and $\hat{u}_{after}^{<a_m,dt>}$, respectively. The spectral differencies of equation (5.9) can be combined for a range of frequencies to obtain

$$\begin{aligned} Z^{<a_m,0>} &= \frac{1}{N}\sum_{n=1}^{N} Z_n^{<a_m,0>} \quad (5.10) \\ z^{<a_m,dt>}\left[(v,\rho)_{before},(v,\rho)_{after},d\right] &= \frac{1}{Z^{<a_m,0>}}\frac{1}{N}\sum_{n=1}^{N} z_n^{<a_m,dt>} \end{aligned}$$

$$\left(S_z^{<a_m,dt>}\right)^2 [(v,\rho)_{before},(v,\rho)_{after},d] \;=\; \frac{1}{N-1}\sum_{n=1}^{N}\left[\frac{z_n^{<a_m,dt>}}{Z^{<a_m,0>}} - z^{<a_m,dt>}\right]^2,$$

where $z^{<a_m,dt>}$ represents the weighted objective function and $(S_z^{<a_m,dt>})^2$ its variance in the frequency range from ω_1 to ω_N for the given parameters $(v,\rho)_{before}$, $(v,\rho)_{after}$ and d. By normalizing with the observed change before and after air injection, the objective function is equal to the unexplained changes in the observed data.

In the experiment analyzed, the fracture is fully water-saturated prior to the air injection and the velocity v_{before} and density ρ_{before} are therefore equal to the water velocity and density, respectively. Hence, we can perform a grid search for the remaining parameters $(v,\rho)_{after}$ and d, and determine the values associated with minima in the objective function. In the low frequency range only the air concentration and aperture are independent parameters, since velocity and density are functions of the air concentration (equation (5.7)). To obtain a measure for the uncertainty of our estimates, we have used the t-test (Student, 1908) to decide if the minima in the objective function are significantly different from each other and used the results to define the confidence interval of our estimates. Since the variances of the objective functions are in general not the same, we have applied Welch's t (Smith, 1936) to compute the pooled standard errors and degrees of freedom. More details about determining the confidence interval of our estimates are given in section 5.8.

As it turns out, the objective function for a single window is not sufficient to

obtain a reliable estimate of the parameters. In general, the objective function increases with longer windows and the confidence intervals of the estimates are generally large. In addition, there often exist several local minima for a single window length which are not significantly different from each other. Hence, we have averaged the objective functions for different window lengths with the same parameter pairs and obtained the absolute minimum of the stacked objective functions with a minimum of four different window lengths.

5.5 Data and results

A detailed description of the Conoco test site and the air injection experiment can be found in Majer et al. (1997). We therefore only describe the information needed for the analysis of our data. Figure 5.3 shows the geometry of the wells used in this analysis. Air injection in GW5 was started at 12:15 p.m. on DAY 1 and lasted for about 6 hours. On the DAY 2, the air injection was continued at 7:15 a.m. for about 2 hours. The analyzed crosswell data consist of a seismic monitor survey between GW1 and GW4 during the air injection and crosswell surveys between GW1 and GW3 before and shortly after the air injection. The horizontally layered lithologies covered by the crosswell survey consist of the Fort Riley limestone, which is bounded by shale layers at the top and bottom. Table 5.2 shows P-wave velocity and density for this formation derived from the crosswell survey and well logs. After the air injection, a change in the seismic

Table 5.2: Velocity and density in the Fort Riley formation derived from the crosswell survey between GW1 and GW3. Depth is relative to the surface at the location of the fracture.

Zone	depth (m)	P-wave velocity (m/s)	bulk density (kg/m^3)
1	13.8 - 19.7	4120	2500
2	19.7 - 26.5	3860	2450
3	26.5 - 28.0	3400	2320
4	28.0 - 29.5	3740	2420

signal could only be observed within the Fort Riley formation and we therefore concentrated our analysis on this formation. Both surveys used a piezoelectric source with a swept sine wave from 1 to 10 kHz tapered at both ends and a sample interval Δt=20 μs. For the analysis, we avoided the tapering effects and used the frequencies from 2 to 9 kHz only.

5.5.1 Seismic monitor survey: data and inversion results

During air injection, a piezoelectric source was placed in well GW1 at 20.2 m depth relative to the surface at the location of the fracture. An 8-element hydrophone string with 1 m spacing was placed in GW4 at 21.7 m depth (top receiver) to monitor the changes in the fracture zone between GW1 and GW4. The transmitter and receiver were not moved during the air injection.

Figure 5.4a shows the changes on the seismograms for the top receiver at different times during the experiment. The modulus and phase changes relative

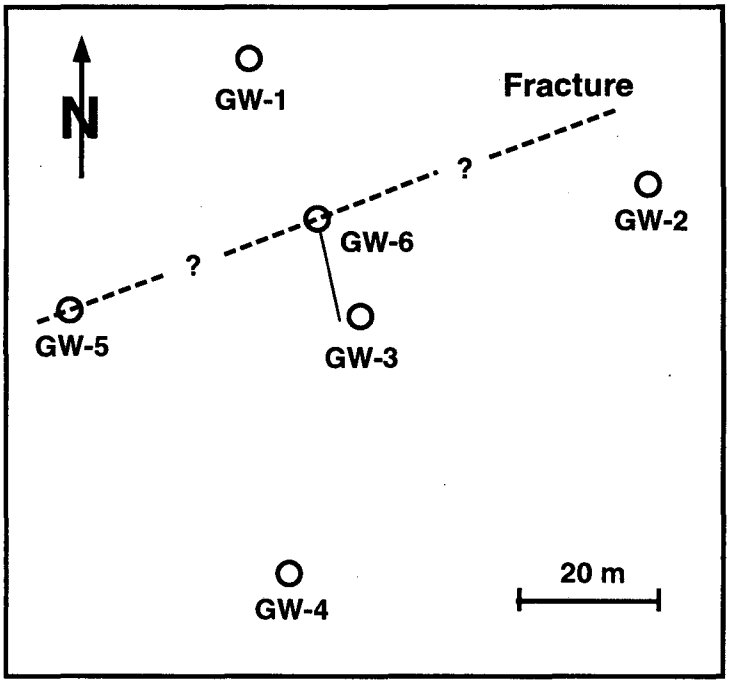

Figure 5.3: Geometry of the shallow wells at the Conoco borehole test facility. GW6 was drilled at GW3 with a slant well drilling rig at 30° from the vertical and penetrates the fracture at 25 m depth.

to the initial trace are shown in Figure 5.4b and 5.4c, respectively. The modulus changes show only small frequency dependence, which indicates that the intrinsic attenuation, i.e., thermal and viscous damping, is only a secondary effect in our data and has been neglected in the following inversions. The comparison of Figure 5.2 and Figure 5.4 shows strong similarities, which suggests that the changes on the seismogram can mainly be attributed to strong scattering attenuation due to air-water mixtures inside the fracture.

After air injection we usually observed a small time delay in the arrival time of the direct wave (Figure 5.4a). Hence, the resonance frequency of the majority of the air bubbles had to be larger than the maximum measured frequency (Spitzer, 1943). Using equation (5.6) and the frequency and depth range of the experiment, the maximum radii of the air bubbles were therefore smaller than about 500 μm, which is consistent with observations in natural waters (Anderson and Hampton, 1980). The velocity of the air-water mixture can therefore be described by Wood's equation.

For the inversion of the monitor survey we have used Wood's equation to calculate velocity and density as a function of air concentration inside the fracture. We have used hydrostatic conditions together with water levels in the wells to calculate the ambient pressure in the fracture fluid at the appropriate depth. Majer et al. (1997) derived an aperture estimate of 1 mm from core analysis in well GW6. We set the maximum aperture to 30 mm to include possible larger

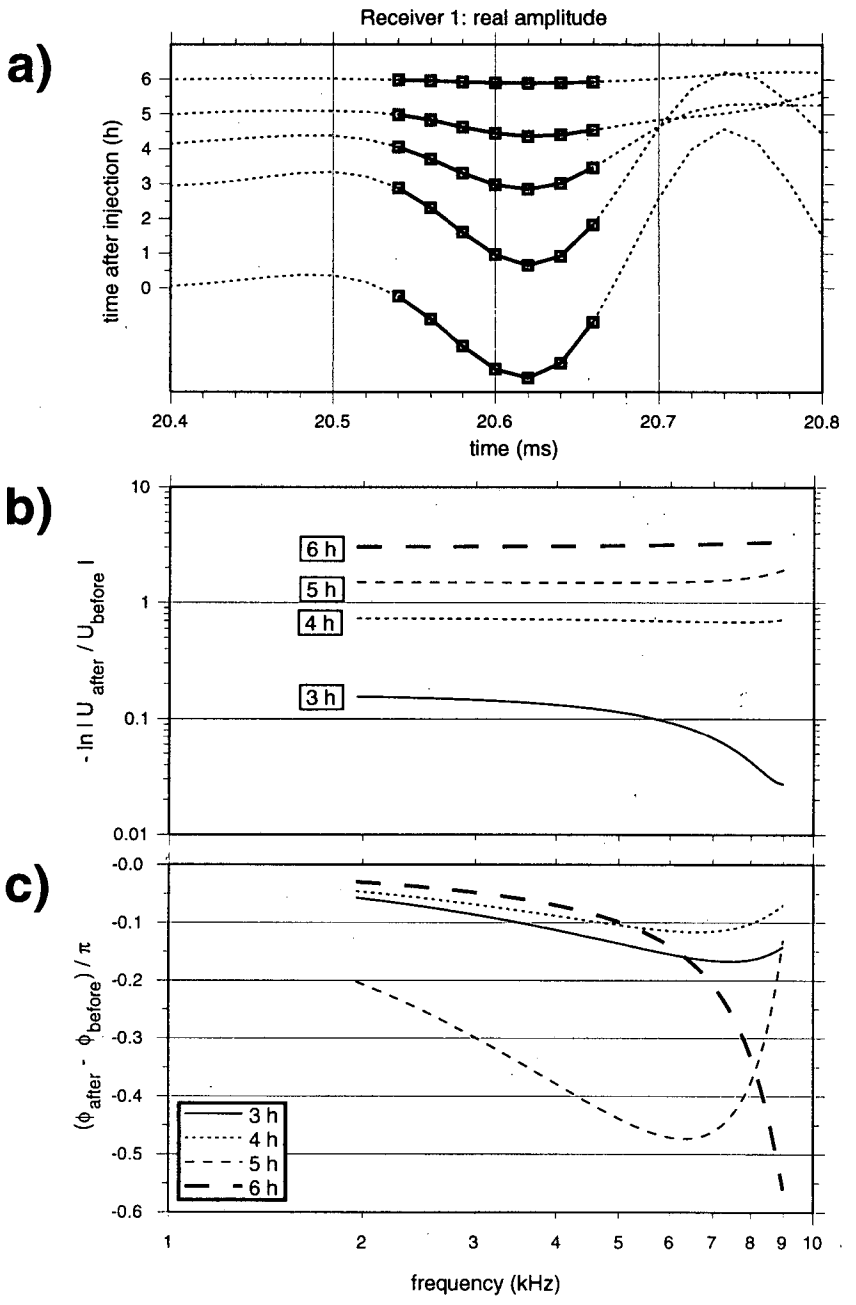

Figure 5.4: Monitor survey: Measured data at receiver 1 at different times during air injection. Similar to Figure 5.2, the solid lines and boxes show the time window, which was used to compute the spectra. a) shows the seismogram, b) the modulus changes and c) the phase changes at different times.

apertures. The monitor data show maximum time delays due to the air injection of less than two sample intervals. Hence, we performed the inversion only in the range where $dt < 2\Delta t$ with a $(c_1, \ldots, c_{100}) \times (d_1, \ldots, d_{200})$ grid. For windowing, we have used a minimum of four different lengths of boxcar functions to fit about half a cycle of the signal, starting with a length of 11 sample intervals. For the t-test, we used the 95% confidence interval.

Figures 5.5 and 5.6 show the inversion results for the first two receivers at 21.7 m and 22.7 m depth, respectively. The inversion of both receivers show very similar features during the experiment. About two hours after starting the air injection, a decrease in the travel time can be observed (Figure 5.7). Our model of a single fracture is not capable of explaining this first small change. It is possible that large air bubbles were entering the fracture, which would lead to smaller travel times (Spitzer, 1943). In this case a detailed analysis of the air bubbles would be required, but such an analysis is beyond the scope of this study. About two hours later, our model starts to explain most of the observed changes, which indicates small air bubbles in the fracture. At the end of DAY 1, air concentrations exceed 10% for both receivers and the velocities inside the fracture drop below 100 m/s, which allows reliable aperture estimates. It also can be observed, that the objective function is decreasing by the end of DAY 1. At the beginning of DAY 2, air concentrations have dropped below 1%, but increase rapidly about one hour after starting the air injection again. Using

only the reliable aperture estimates, the aperture at the first receiver is 0.5 mm and at the second receiver 0.9 mm.

Figure 5.7 shows the fit to the measured traces for the same two receivers of Figure 5.5 and 5.6. About two hours after the air injection the waveforms start to change. By the end of DAY 1 the amplitudes have decreased significantly without significant travel time changes. The other six receivers show generally the same features as the top two, although the uncertainty of the parameter estimates is larger for the lower receivers.

5.5.2 Crosswell survey: data and inversion results

The results of the monitor survey have shown that we can resolve apertures in the millimeter range due to the extremely slow velocity of air-water mixtures. In the following we have applied the same inversion scheme as before to a crosswell survey between GW1 and GW3 (48.4 m apart) perpendicular to the fracture zone and derived velocity, air concentration and aperture profiles. For the crosswell survey, the same instruments and technical specifications as in the monitor survey were used. The piezoelectric source was placed in well GW3 and the fourth receiver from the top (receiver 4) was placed in GW1 directly across from the source. During the crosswell survey the source and the 8-element hydrophone string were moved concurrently in 0.25 m increments up the holes.

Figure 5.8a shows the seismogram before the air injection for receiver 4 in

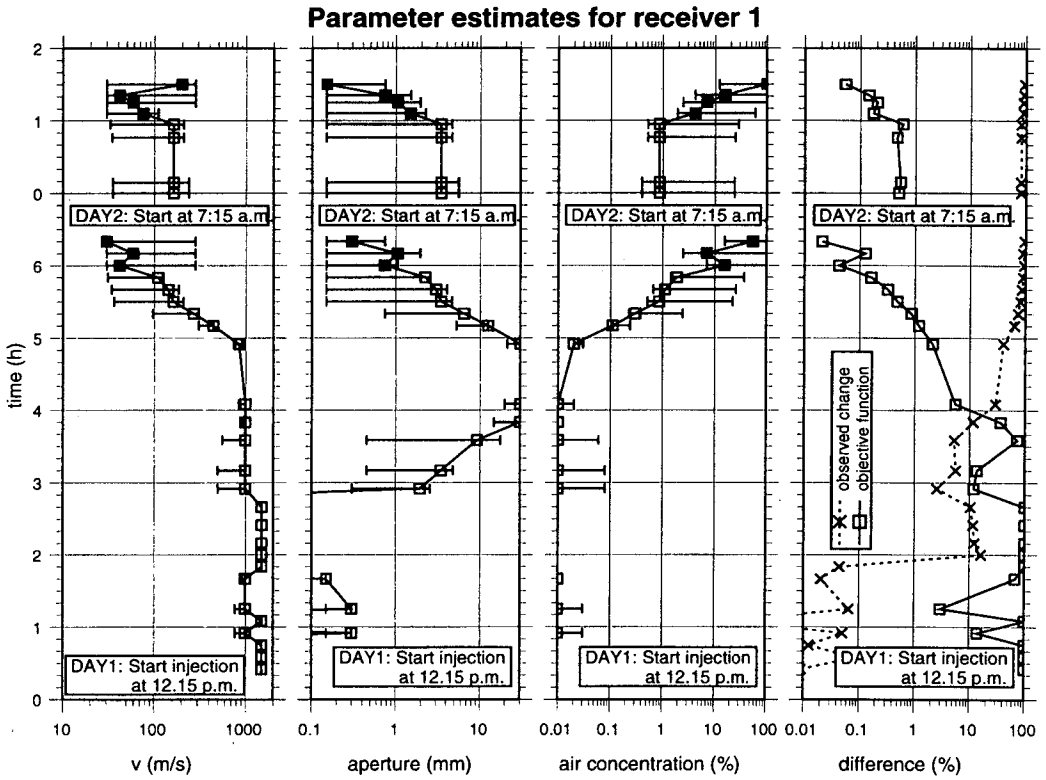

Figure 5.5: Monitor survey: Inversion results for the top receiver at 21.7 m depth. The error bars indicate the 95% confidence interval determined by the t-test. The last figure on the right hand side shows the observed changes (dotted line) and the unexplained part of those changes by the single fracture model (solid line, equation (5.10)). Reliable aperture estimates can only be obtained if the velocity drops below 100 m/s and are marked by solid boxes. The mean aperture for the first receiver is 0.49 mm (95% confidence interval: 0.35 mm-0.66 mm)

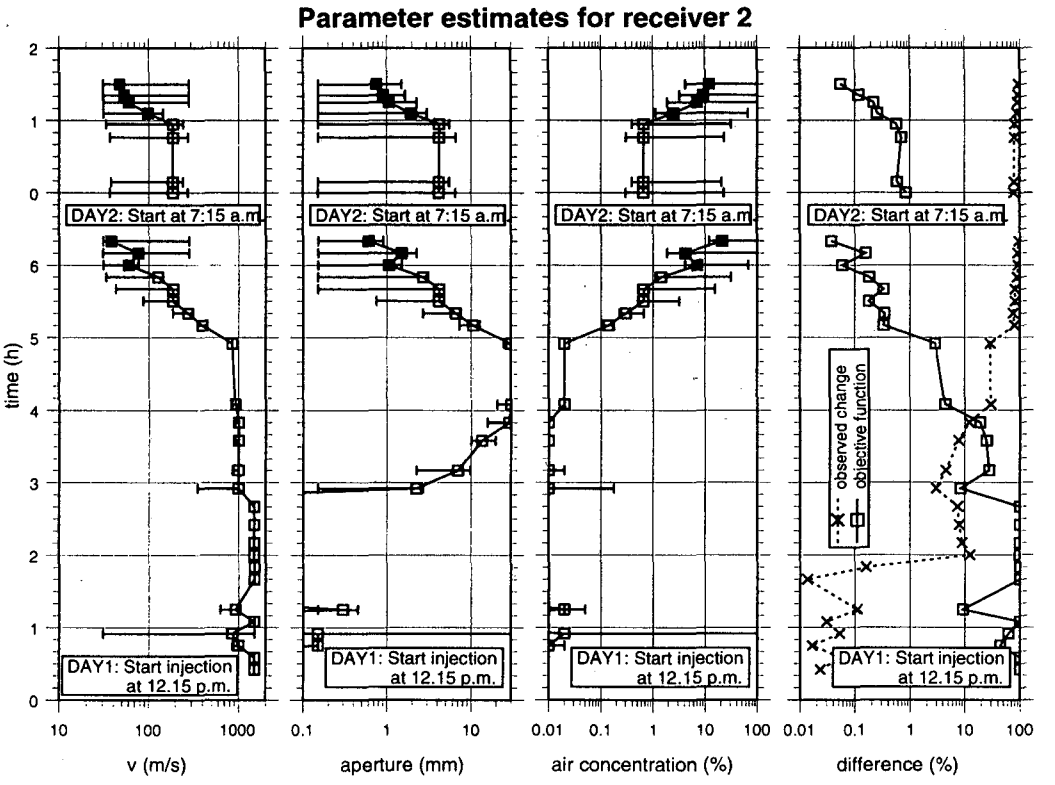

Figure 5.6: Similar to Figure 5.5. Monitor survey: Inversion results for receiver 2 at 22.7 m depth. The mean aperture for the second receiver is 0.90 mm (95% confidence interval: 0.62 mm-1.07 mm)

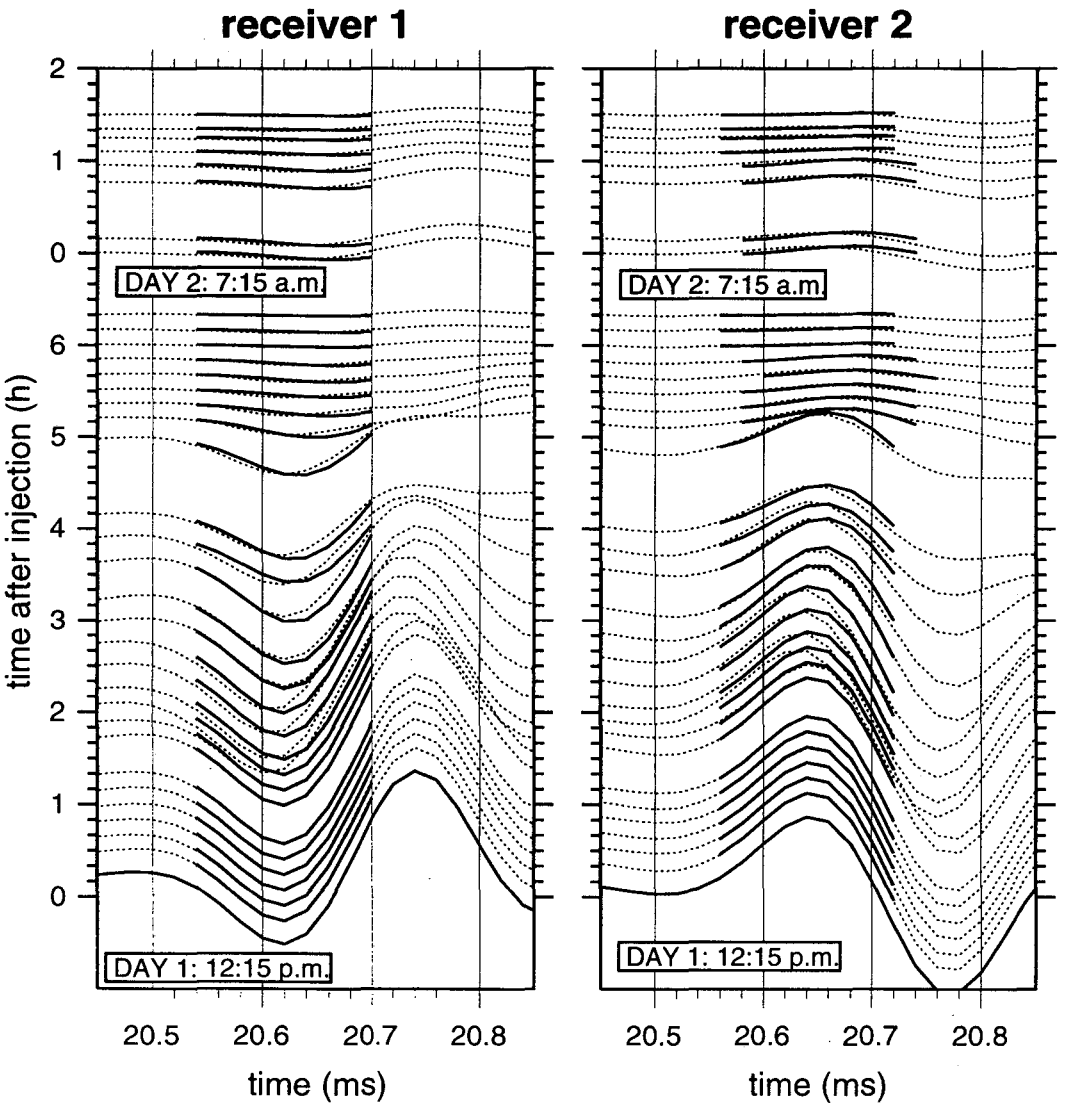

Figure 5.7: Monitor survey: The dotted lines are the measured traces at receiver 1 and 2 during the experiment. The fitted traces are overlain on top of the data and are calculated using the parameters in Figure 5.5 and 5.6.

the Fort Riley formation. The traces have been individually normalized by their maximum amplitude. Figure 5.8b and Figure 5.8c show the seismogram for receiver 4 after the air injection. The traces have been individually normalized by the maximum before the air injection and after the air injection, respectively. Figure 5.8b shows strong attenuation from the top of the Fort Riley to the bottom of ZONE 2 (26.5 m depth). Below this zone the amplitudes are hardly affected by the experiment.

Before a parameter profile can be constructed, one must first identify the direct waves on the seismogram. For this purpose, we have used the velocities in Table 5.2 to pick the direct waves (Figure 5.8a). We have noticed that close to velocity boundaries the direct wave cannot be separated from reflections and refractions. Hence, we expect considerable uncertainty of our inversion close to velocity boundaries. Stacking can not be used to enhance the direct wave, because the moveout of the later arrivals is not large enough. We therefore performed the inversion procedure for three receivers (receiver 3, 4 and 5) and calculated the average of the individual inversion results. The average was computed with weighted least squares, using the objective function as the weighting function. The stacked parameter profiles are shown in Figure 5.9. The inversion results show variable air concentrations and fracture apertures as a function of depth. Reliable aperture estimates could only be obtained between 16.4-19.4 m and 22.9-24.2 m depth, where air concentrations are large. The aperture esti-

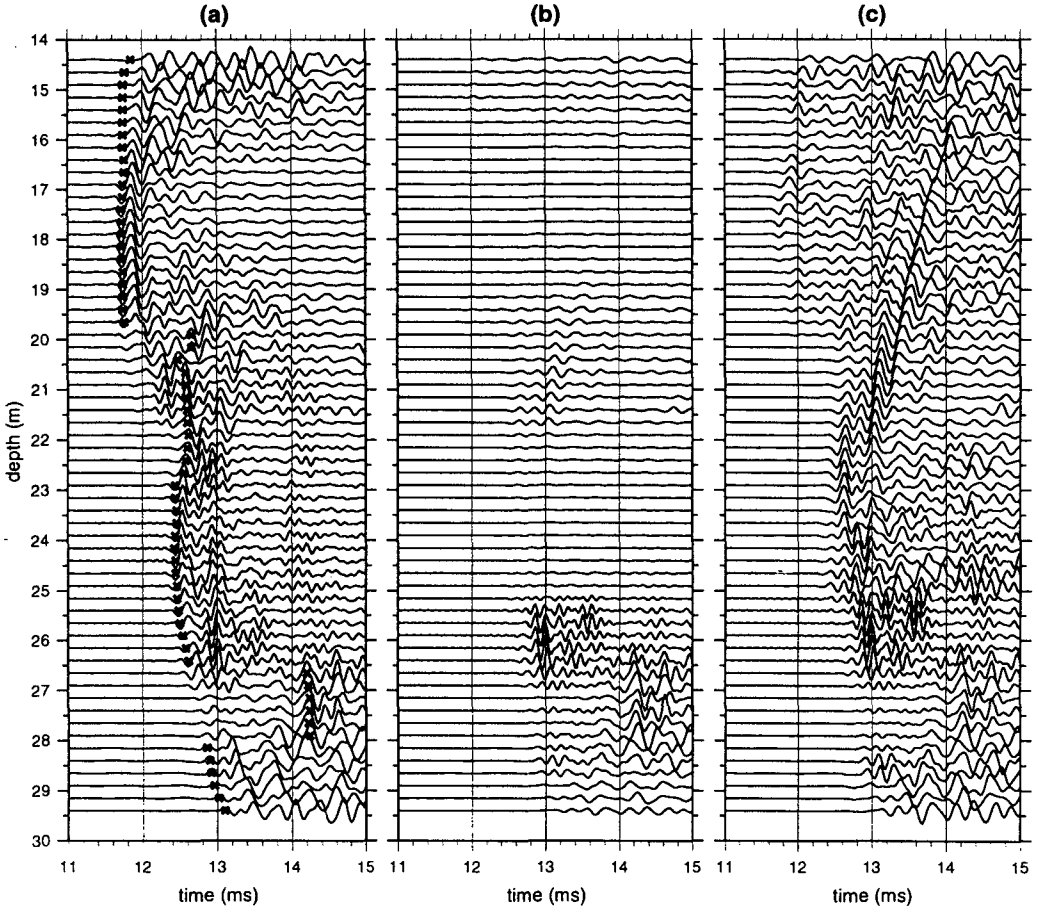

Figure 5.8: Seismograms of receiver 4: a) Seismogram before the air injection. Traces have been individually normalized by their maximum. Crosses denote the arrival time of the direct wave. b) Seismogram after the air injection. Traces have been individually normalized by the maximum before the air injection. c) Seismogram after the air injection. Traces have been individually normalized by their maximum.

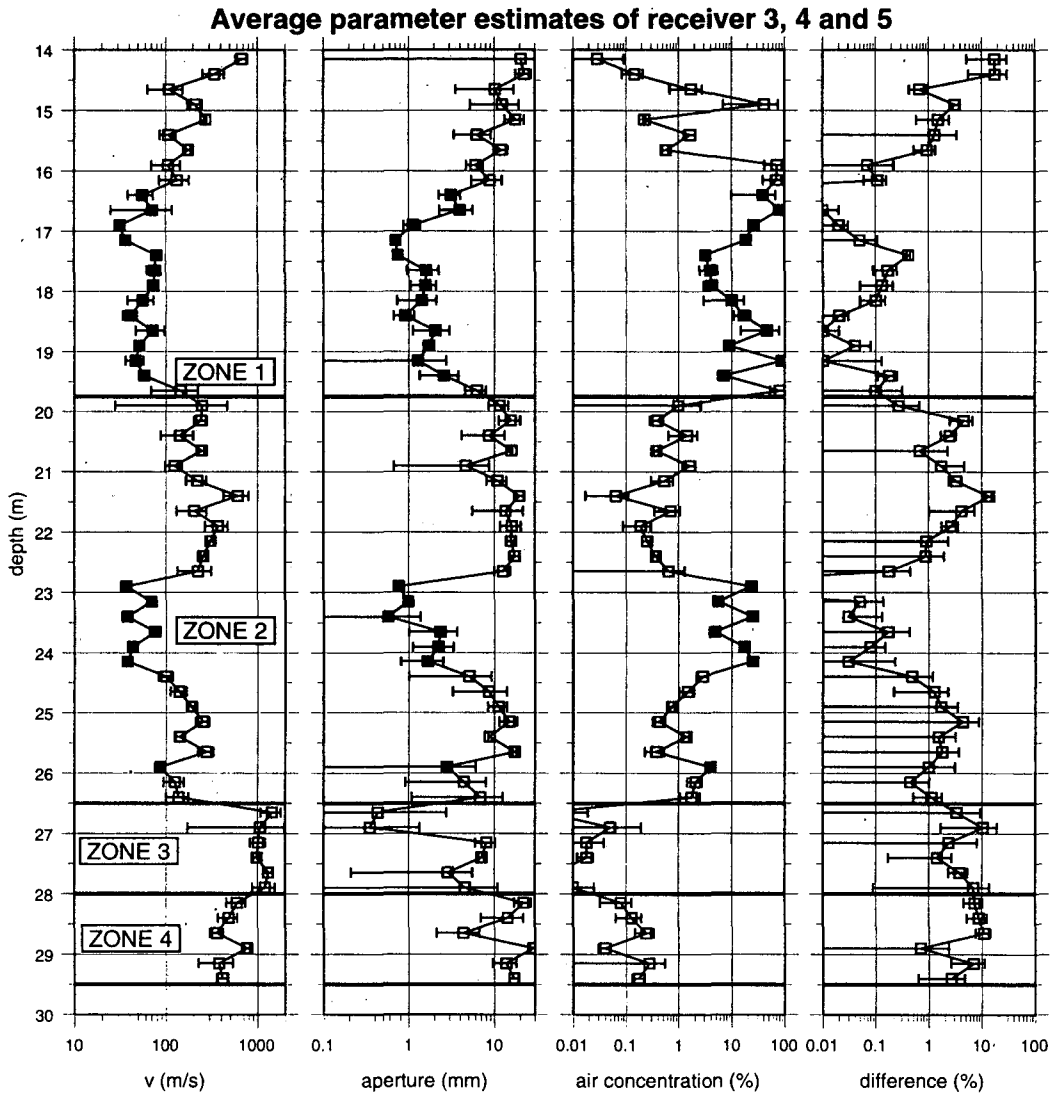

Figure 5.9: Average parameter estimates derived from the individual inversions of receiver 3, 4 and 5. The error bars denote one standard error derived by the weighted least square method. Reliable aperture estimates can only be obtained if the velocity drops below 100 m/s and are marked by solid boxes.

mates vary between the submillimeter range to a few millimeters. At 22.9 m depth, the aperture estimate is 0.8 mm, which agrees well with the monitor survey. At the top of the Fort Riley formation the objective function is large. As we have discussed above, the inversion may be affected by the large velocity contrast between the Fort Riley formation and the shale layer at the top. At about 16 m depth air concentrations rise sharply and the objective function decreases. The same feature can be observed at the interface between ZONE 2 and ZONE 3. Within ZONE 3 and ZONE 4, air concentrations are very small and the objective function is large. Hence, from the results in Figure 5.8 and Figure 5.9 we conclude that the fracture extends only from 16 m to 26.5 m depth, which is consistent with the single well survey (Majer et al., 1997).

Since the crosswell survey was acquired after the air injection, air may have risen due to the density difference between air and water. One would therefore expect larger air volumes, where the flow of air has been blocked. In fact, air has accumulated in ZONE 1 at the top of the fracture at 16 m depth. In ZONE 2 large air concentrations can only be observed from 23 m to 24 m depth, whereas air concentrations are significantly smaller below and above this depth interval. Hence, apertures may become smaller above 23 m depth or the fracture may not be continuous.

5.6 Discussion

The model of one single fracture provides consistent results for the monitor survey. Both amplitudes and phase of the seismic signals can be matched accurately and aperture and air concentration estimates are consistent for different receivers. The analysis of the monitor survey shows that apertures in the millimeter range can actually be resolved by seismic waves in the kilohertz range. The crosswell survey revealed large variability of apertures and air concentrations. The depth range of the fracture from about 16 m to 26.5 m is consistent with the single well survey (Majer et al., 1997).

Majer et al. (1997) estimated a fracture aperture of 1 mm at about 25 m depth from core analysis. However, one side of the fracture was broken into rubble, which made it especially difficult to estimate the *in situ* fracture aperture. At 25 m depth we were not able to obtain a reliable aperture estimate, because air concentrations were too small at this depth. Our aperture estimates in ZONE 1 and part of ZONE 2 range from less than one millimeter to a few millimeters, which is comparable to the core analysis. We are therefore confident in our inversion results, which provide the only high resolution aperture estimates from *in situ* measurements.

The question remains if it is appropriate to represent a possible fracture zone by a single fracture, which we have assumed from core analysis in well GW5 and GW6. In general, seismic measurements will rarely provide an unique solution,

because there is no single model which can explain the data perfectly. It is therefore essential to use additional information to assess the validity of a single fracture model. Our aperture estimates are also supported by the interpretation of a tracer survey that suggested average fracture apertures between 0.7 mm and 1.2 mm (Sheely, 1991). However, since we have analyzed the difference before and after air injection, we have only imaged fractures which were actually affected by the experiment. There might be smaller fractures with lower permeabilities which prevented air from entering. Thus, our inversion of the seismic waves probably yields the largest fracture which acted as the main flow path during the experiment.

5.7 Conclusions

We have shown that the single fracture model with variable air-water mixtures can explain the two major features encountered during an air injection experiment in a fractured limestone:

1. The amplitude of the seismic waves decreases by orders of magnitudes during air injection due to strong scattering attenuation of the fracture.

2. Travel time changes are very small.

If air concentrations inside the fracture become large and the seismic velocity drops below 100 m/s, apertures in the millimeter range can be resolved with

seismic waves in the kilohertz range because the corresponding wavelengths become comparable to the fracture dimension. These results are generally true for any gassy fluid, where the compressibility of the gas is much larger than of the surrounding fluid. Intrinsic attenuation of gassy fluids, i.e. thermal and viscous damping, does not seem to be important for small apertures. However, velocity and amplitude of the transmitted wave become frequency dependent due to reverberations inside the fracture. We have also shown that crosswell surveys can be used to compute air concentration and aperture profiles, which give more insight into aperture changes with depth and the preferential flow paths.

A priori information about the subsurface and the fracture zone itself is very important in obtaining an accurate starting model for the inversion. In our case a combination of tracer tests, crosswell and single well surveys proved to be appropriate tools for locating and characterizing the fracture zone. There may be a variety of other applications for the method we have used, where a combination of fractures and volatiles enables seismic methods to resolve features of very small dimension. In particular, seismic monitor surveys during steam injection could be used to detect and delineate changes in the subsurface.

5.8 Appendix: Confidence interval of the parameter estimates

To estimate fracture aperture and the elastic properties of the fracture fluid, we have performed a grid search for the aperture and air concentration. For every parameter pair (c_i,d_j), the objective function $(z^{<a_m,dt>})_{i,j}$ and its variance $(S_z^{<a_m,dt>})^2_{i,j}$ with the time window length a_m have been calculated (equation (5.10)). Among all objective functions for a single window length a_m, there is one parameter pair c_{i0},d_{j0} with the minimum objective function. We have used the t-test (Student, 1908) to decide, if $(z^{<a_m,dt>})_{i0,j0}$ is significantly different from the objective function of a different parameter pair (c_i,d_j)

$$t_{i,j} = \frac{(z^{<a_m,dt>})_{i,j} - (z^{<a_m,dt>})_{i0,j0}}{SE\left[(z^{<a_m,dt>})_{i,j} - (z^{<a_m,dt>})_{i0,j0}\right]}, \tag{5.11}$$

where SE is the standard error. Since the variance of the objective functions is generally not the same, we have applied Welch's approximate t (Smith, 1936) to calculate the standard error SE and the degrees of freedom ν

$$SE\left[(z^{<a_m,dt>})_{i,j} - (z^{<a_m,dt>})_{i0,j0}\right] = \sqrt{\frac{(S_z^{<a_m,dt>})^2_{i,j} + (S_z^{<a_m,dt>})^2_{i0,j0}}{N}} \tag{5.12}$$

$$\nu(c_i, d_j; c_{i0}, d_{j0}) = (N-1)\frac{\left[(S_z^{<a_m,dt>})^2_{i,j} + (S_z^{<a_m,dt>})^2_{i0,j0}\right]^2}{(S_z^{<a_m,dt>})^4_{i,j} + (S_z^{<a_m,dt>})^4_{i0,j0}}, \tag{5.13}$$

where N is the number of frequency values. With equation (5.11), (5.12) and (5.13) Student's t for every parameter pair (c_i,d_j) can be calculated. Figure 5.10 shows Student's t for the measurement at receiver 1 during the monitor survey

at the end of the experiment (Figure 5.7) with four stacked windows. The minimum objective function at t=0 is obtained with the parameter pair (c=66.7%, d=0.33 mm). For this example, the degrees of freedom are ν=9, which yields the critical t-value t=2.26 for the 95% confidence level. Parameter pairs with t-values smaller than the critical t-value are not significantly different from the minimum objective function. The 95% confidence interval for the air concentration is therefore 40-100% and for the aperture 0.33-1.00 mm (Figure 5.10).

aperture (mm)

air concentration (%)	0	0.33	1.00	1.67	2.33	3.00	3.67	4.33	5.00	5.66	6.33	7.00	7.67	8.33	9.00	9.67
0.07	-	-	-	9.85	9.44	9.20	9.06	8.96	8.90	8.85	8.82	8.80	8.78	8.77	8.76	8.76
0.44	-	9.45	8.86	8.85	8.87	8.88	8.89	8.89	8.90	-	-	-	-	-	-	-
3.0	-	9.01	9.22	8.60	-	-	-	-	-	-	-	-	-	-	-	-
13.3	-	8.90	-	-	-	-	-	-	-	-	-	-	-	-	-	-
20.0	-	7.01	-	-	-	-	-	-	-	-	-	-	-	-	-	-
26.7	-	4.43	-	-	-	-	-	-	-	-	-	-	-	-	-	-
33.3	-	2.43	-	-	-	-	-	-	-	-	-	-	-	-	-	-
40.0	-	1.20	-	-	-	-	-	-	-	-	-	-	-	-	-	-
46.7	-	0.51	-	-	-	-	-	-	-	-	-	-	-	-	-	-
53.3	-	0.16	-	-	-	-	-	-	-	-	-	-	-	-	-	-
60.0	-	0.02	-	-	-	-	-	-	-	-	-	-	-	-	-	-
66.7	-	0	-	-	-	-	-	-	-	-	-	-	-	-	-	-
73.3	-	0.05	-	-	-	-	-	-	-	-	-	-	-	-	-	-
91.8	-	0.36	-	-	-	-	-	-	-	-	-	-	-	-	-	-
96.6	-	0.45	2.20	-	-	-	-	-	-	-	-	-	-	-	-	-
98.6	-	0.50	2.22	2.61	2.77	-	-	-	-	-	-	-	-	-	-	-
99.4	-	0.51	2.23	2.61	2.77	2.86	-	-	-	-	-	-	-	-	-	-
99.8	-	0.51	2.23	2.61	2.77	2.86	2.91	2.95	-	-	-	-	-	-	-	-
99.9	-	0.51	2.23	2.61	2.77	2.86	2.91	2.95	2.98	-	-	-	-	-	-	-
100	-	0.51	2.23	2.61	2.77	2.86	2.92	2.95	2.98	3.00	3.02	-	-	-	-	-

Figure 5.10: Example of an inversion: Student's t for different pairs of air concentration and aperture at the first receiver during the monitor survey at the end of the experiment with four stacked windows. The minimum objective function is at 66.7% air concentration and 0.33 mm aperture. The critical t-value for this example is t = 2.26 for the 95% confidence level and the shaded area denotes the 95% confidence interval. If Student's t exceeds 9.99, no values are plotted.

References

Aki, K., and Richards, R. G., 1980, Quantitative Seismology: Theory and Methods: W. H. Freeman & Co.

Anderson, A. L., and Hampton, L. D., 1980, Acoustics of gas-bearing sediments I. Background: J. Acoust. Soc. Am., **67**, no. 6, 1865–1889.

Anderson, D. L., 1989, Theory of the earth: Blackwell Scientific Publications.

Balch, A. H., and Erdemir, C., 1996, A Nine-Component, Multi-Offset Vertical Seismic Profile at the UE-25 UZ#16 Borehole, Nevada Test Site, Nye County, Nevada: Taking VSP's to a New Level: Yucca Mountain Site Characterization Office, **Milestone 3GUP622M**.

Banik, N. C., Lerche, I., Resnick, J. R., and Shuey, R. T., 1985a, Stratigraphic filtering, Part I: Derivation of the O'Doherty-Anstey formula: Geophysics, **50**, 2768–2774.

——— 1985b, Stratigraphic filtering, Part II: Model spectra: Geophysics, **50**, 2775–2783.

Berge, P. A., Bonner, B. P., and Berryman, J. G., 1995, Ultrasonic velocity-porosity relationships for sandstone analogs made from fused glass beads: Geophysics, **60**, 108–119.

Berryman, J. G., 1980a, Long-wavelength propagation in composite elastic media I. Spherical inclusions: J. Acoust. Soc. Am., **68**, no. 6, 1809–1819.

——— 1980b, Long-wavelength propagation in composite elastic media II. Ellipsoidal inclusions: J. Acoust. Soc. Am., **68**, no. 6, 1820–1831.

Biot, M. A., 1956a, Theory of propagation of elastic waves in a fluid saturated porous solid: I. Low frequency range: J. Acoust. Soc. Am., **28**, 168–178.

——— 1956b, Theory of propagation of elastic waves in a fluid saturated porous solid: II. Higher frequency range: J. Acoust. Soc. Am., **28**, 179–191.

Broxton, D. E., Bish, D. L., and Warren, R. G., 1987, Distribution and chemistry of diagenetic minerals at Yucca mountain, Nye County, Nevada: Clays and Clay Miner., **35**, no. 2, 89–110.

Bryant, S., and Raikes, S., 1995, Prediction of elastic-wave velocities in sandstones using structural models: Geophysics, **60**, 437–446.

Burridge, R., Papanicolaou, R., Sheng, G., and White, B., 1988, One-dimensional wave propagation in a highly discontinuous medium: Wave Motion, **10**, 19–44.

Carmichael, R. S., 1982, Practical handbook of physical properties of rocks and minerals: CRC Press.

Caviglia, G., and Morro, A., 1988, Inhomogeneous waves and sound absorption in viscous fluids: Physics Letter A, **134**, no. 2, 127–130.

Datta-Gupta, A., Vasco, D. W., and Long, J. C., 1994, Detailed characterization of a fractured limestone formation using stochastic inverse approaches: SPE/DOE Paper 27744, pages 71–86.

Devin, C. D., 1959, Survey of Thermal, Radiation, and Viscous Damping of Pulsating Air Bubbles in Water: J. Acoust. Soc. Am., **31**, no. 12, 1654–1667.

Dvorkin, J., and Nur, A., 1996, Elasticity of high-porosity sandstones: Theory for two north sea data sets: Geophysics, **61**, 1363–1370.

Dvorkin, J., Mavko, G., and Nur, A., 1995, Squirt flow in fully saturated rocks: Geophysics, **60**, 97–107.

Eller, A. I., 1970, Damping Constants of Pulsating Bubbles: J. Acoust. Soc. Am., **47**, no. 5, 1469–1470.

Foldy, L. L., 1945, The multiple scattering of waves: Physical Review, **67**, 107–119.

Frazer, L. N., 1994, A pulse in a binary sediment: Geophysical Journal International, **118**, no. 1, 75–93.

Gassmann, F., 1951, Über die Elastizität elastischer Medien: Vierteljahresschrift der Naturforschenden Gesellschaft Zürich, **96**, 1–21.

Geslin, J. K., Moyer, T. C., and Buesch, D. C., 1994, Summary of lithostratigraphic logging of new and existing boreholes at Yucca Mountain, Nevada, August 1993 to February 1994: U.S. Geological Survey Open-File Report 94-342.

Goff, J. A., Hollinger, K., and Levander, A., 1994, Modal fields: A new method for characterization of random seismic velocity heterogeneity: Geophysical Research Letters, **21**, no. 6, 493–496.

Gregory, A. R., 1977, Aspects of rock physics from laboratory and log data that are important to seismic interpretation, *in* Payton, C. E., Ed., Seismic Stratigraphy - applications to hydrocarbon exploration: Am. Assn. Petr. Geol., Memoir, 26, 15–47.

Groenenboom, J., and Snieder, R., 1995, Attenuation, dispersion, and anisotropy by multiple scattering of transmitted waves through distributions of scatterers: J. Acoust. Soc. Am., **98**, no. 6, 3482–3492.

Hashin, Z., and Shtrikman, S., 1963, A variational approach to the elastic behavior of multiphase materials: J. Mech. Phys. Solids, **11**, 127–140.

Ishimaru, A., 1978, Wave propagation and scattering in random media: Academic Press, John Wiley Inc.

Johnson, L. J., and Plona, T. J., 1982, Acoustic slow waves and the consolidation transition: J. Acoust. Soc. Am., **72**, no. 2, 556–564.

Kennett, B. L. N., 1983, Seismic wave propagation in the stratified media: Cambridge University Press.

Korneev, V. A., and Johnson, L. R., 1993, Scattering of elastic waves by spherical inclusions - 1. Theory and numerical results: Geophysical Journal International, **115**, 230–250.

Korneev, V. A., and Johnson, L. R., 1996, Scattering of P and S waves by a spherically symmetric inclusion: Pure and applied geophysics, **147**, 675–718.

Korneev, V. A., and Johnson, L. R., 1998, Fluctuations in elastic waves due to random scattering from inclusions: in preparation.

Kuster, G., and Toksöz, M., 1974, Velocity and attenuation of seismic waves in two-phase media: Part I. Theoretical formulations: Geophysics, **39**, 587–606.

Lugo, C. L., 1993, Preliminary Field Composite Borehole Log for Borehole UE-25 UZ number 16: Letter: Lugo, C. L. (SAIC) to Gertz, C. P. (DOE), April 15, 1993, RIS document NNA.930427.0128.

Majer, E. L., Datta-Gupta, A., Peterson, J. E., Vasco, D. W., Myer, L. R., Daley, T. M., Kaelin, B., Queen, J., D'Onfro, P. S., Rizer, W. D., and Sinton, J., 1996, Utilizing crosswell, single well and pressure transient tests for characterizing fractured gas reservoirs: The Leading Edge, **15**, no. 8, 951–956.

Majer, E. L., Peterson, J. E., Daley, T. M., Kaelin, B., Myer, L., Queen, J., D'Onfro, P., and Rizer, W., 1997, Fracture detection using crosswell and single well surveys: Geophysics, **62**, 495–504.

Marion, D., Mukerji, T., and Mavko, G., 1994, Scale effects on velocity dispersion: From ray to effective medium theories in stratified media: Geophysics, **59**, 1613–1619.

Mehta, C. H., 1983, Scattering theory of wave propagation in a two-phase medium: Geophysics, **48**, 1359–1370.

Mie, G., 1908, Contribution on the optics of cloudy media, special colloidal metal solutions: Annalen der Physik, **25**, 377–445.

Minnaert, M., 1933, On musical air bubbles and the sound of running water: Philos. Mag., **10**, 235–248.

Nelson, P. H., and Anderson, L. A., 1992, Physical properties of ash flow tuff from Yucca mountain, Nevada: Journal of geophysical research, **97**, 6823–6841.

O'Connell, R. J., and Budiansky, B., 1974, Seismic velocities in dry and saturated cracked solids: Journal of geophysical research, **79**, 5412–5426.

O'Connell, R. J., and Budiansky, B., 1977, Viscoelastic properties of fluid-saturated cracked solids: Journal of geophysical research, **82**, 5719–5735.

O'Doherty, R. F., and Anstey, N. A., 1971, Wave propagation in stratified medium: Geophys. Prosp., **19**, 430–458.

Petrashen, G. I., 1950, Dynamic problem of the theory of elasticity in the case of isotropic sphere: Scientific papers of Leningrad State University, Series in mathematical sciences, **135**, 24–70.

Press, W. H., Teukolsky, S. A., Vetterling, W. T., and Flannery, B. P., 1992, Numerical Recipes: The Art of Scientific Computing, Second Edition: Cambridge University Press.

Reuss, A., 1929, Berechnung der Fliessgrenze von Mischkristallen auf Grund der Plastizitätsbedingung für Einkristalle: Zeitschrift für angewandte Mathematik und Mechanik, **9**, 49–58.

Richards, P. G., and Menke, W., 1983, The apparent attenuation of a scattering medium: Bull. seism. Soc. Am., **73**, 1005–1021.

Sams, M. S., Neep, J. P., Worthington, M. H., and King, M. S., 1997, The measurement of velocity dispersion and frequency-dependent intrinsic attenuation in sedimentary rocks: Geophysics, **62**, 1456–1464.

Schoenberger, M., and Levin, F. K., 1974, Apparent attenuation due to intrabed multiples: Geophysics, **39**, 278–291.

Seifert, P. K., Kaelin, B., and Johnson, L. R., 1998, Viscosity effect of pore fluids in unconsolidated sand on ultrasonic signals: J. Acoust. Soc. Am., submitted.

Shapiro, S. A., Zien, H., and Hubral, P., 1994, A generalized O'Doherty-Anstey formula for waves in finely layered media: Geophysics, **59**, 1750–1762.

Sheely, C. Q., 1991, Tracer survey conducted in the shallow wells of the Fort Riley formation at the Newkirk Borehole Test Facility during October 1990: Conoco Research report.

Silberman, E., 1957, Sound velocity and attenuation in bubble mixtures measured in standing wave tubes: J. Acoust. Soc. Am., **29**, 925–933.

Smith, H., 1936, The problem of comparing the results of two experiments with unequal means: J. Council Sci. Indust. Res., **9**, 211–212.

Spitzer, L., 1943, Acoustic properties of gas bubbles in a liquid: Office of scientific research and development, Report 1705, Division of War Research, Columbia University.

Student, 1908, The probable error of mean: Biometrika, **6**, 1–25.

Truell, R., Elbaum, C., and Chick, B. B., 1969, Ultrasonic methods in solid state physics: Academic Press, New York.

Twersky, V., 1975, Transparency of pair-correlated, random distributions of small scatterers, with applications to the cornea: J. Opt. Soc. Am., **65**, 524–530.

Van de Hulst, H. C., 1957, Light scattering by small particles: New York, John Wiley Inc.

Wang, Z., and Nur, N. A., 1992, Seismic and acoustic velocities in reservoir rocks, 2 - Theoretical and model studies:, number 10 in Geophysics reprint series Soc. Expl. Geophys.

White, B., Sheng, P., and Nair, B., 1990, Localization and backscattering spectrum of seismic waves in stratified lithology: Geophysics, **55**, 1158–1165.

Winkler, K. W., and Murphy III, W. F., 1995, Acoustic velocity and attenuation in porous rocks, *in* Ahrens, T. J., Ed., Rock physics & phase relations : a handbook of physical constants: American Geophysical Union, AGU reference shelf, 3, 20–34.

Wood, A. B., 1930, A textbook of sound: McGraw-Hill, New York.

Yamakawa, N., 1962, Scattering and attenuation of elastic waves: Geophysical Magazine (Tokyo), **31**, 63–103.

Ying, C. F., and Truell, R., 1956, Scattering of a plane longitudinal wave by spherical obstacle in an isotropically elastic solid: Journal of applied physics, **27**, 1086–1097.

Appendix A

Comparison between Berryman's theory and Gassmann's equations

For the case of saturated and dry inclusions, Berryman's equation (1980a) becomes

$$\begin{aligned}
\frac{1}{K_{sat}+\frac{4}{3}\mu_{sat}} &= \frac{1-\phi}{K_0+\frac{4}{3}\mu_{sat}}+\frac{\phi}{K_f+\frac{4}{3}\mu_{sat}} \qquad \text{(A.1)}\\
\frac{1}{\mu_{sat}+F_{sat}} &= \frac{1-\phi}{\mu_0+F_{sat}}+\frac{\phi}{F_{sat}}\\
F_{sat} &= \frac{\mu_{sat}}{6}\left(\frac{9K_{sat}+8\mu_{sat}}{K_{sat}+2\mu_{sat}}\right)\\
\frac{1}{K_{dry}+\frac{4}{3}\mu_{dry}} &= \frac{1-\phi}{K_0+\frac{4}{3}\mu_{dry}}+\frac{\phi}{K_{air}+\frac{4}{3}\mu_{dry}} \qquad \text{(A.2)}\\
\frac{1}{\mu_{dry}+F_{dry}} &= \frac{1-\phi}{\mu_0+F_{dry}}+\frac{\phi}{F_{dry}}\\
F_{dry} &= \frac{\mu_{dry}}{6}\left(\frac{9K_{dry}+8\mu_{dry}}{K_{dry}+2\mu_{dry}}\right),
\end{aligned}$$

where K_0, K_{sat}, K_{dry}, K_f and K_{air} are the bulk moduli of the mineral grains, the saturated composite, the dry composite, the pore fluid and the air, respectively. μ_{sat} and μ_{dry} are the shear moduli of the saturated composite and the dry composite and ϕ is the porosity. Gassmann (1951) assumed that the shear

moduli of the saturated composite and the dry composite are the same. If this assumption is applied to equation (A.1) and (A.2), we obtain

$$\frac{1}{K_{sat}+x} = \frac{1-\phi}{K_0+x} + \frac{\phi}{K_f+x} \tag{A.3}$$

$$\frac{1}{K_{dry}+x} = \frac{1-\phi}{K_0+x} + \frac{\phi}{K_{air}+x}, \tag{A.4}$$

where

$$x = \frac{4}{3}\mu_{sat} = \frac{4}{3}\mu_{dry} \tag{A.5}$$

After some manipulation, equation (A.3) becomes

$$x = \frac{\frac{1-\phi}{K_0} + \frac{\phi}{K_f} - \frac{1}{K_{sat}}}{\frac{1-\phi}{K_f K_{sat}} + \frac{\phi}{K_0 K_{sat}} - \frac{1}{K_0 K_f}} \tag{A.6}$$

and equation (A.4) becomes

$$x\left[(1-\phi) + \phi\frac{K_{air}}{K_0} - \frac{K_{dry}}{K_0}\right] = \frac{K_{air}}{K_0}\left[(1-\phi)K_{dry} - K_0\right] + \phi K_{dry}. \tag{A.7}$$

Since $K_{air}/K_0 \ll 1$, equation (A.7) simplifies to

$$x = \frac{\phi}{\frac{1-\phi}{K_{dry}} - \frac{1}{K_0}}. \tag{A.8}$$

Combining equation (A.8) and equation (A.6), we obtain

$$\frac{1}{K_{sat}}\left[\frac{\phi}{K_f} - \frac{1+\phi}{K_0} + \frac{1}{K_{dry}}\right] = \frac{1-\phi}{K_0 K_{dry}} + \frac{\phi}{K_f K_{dry}} - \frac{1}{K_0^2} \tag{A.9}$$

$$\frac{1}{K_{sat}} = \frac{\frac{\phi}{K_f K_{dry}} + \frac{1-\phi}{K_0 K_{dry}} - \frac{1}{K_0^2}}{\frac{\phi}{K_f} - \frac{1+\phi}{K_0} + \frac{1}{K_{dry}}} \tag{A.10}$$

$$\frac{1}{K_{sat}} = \frac{1}{K_{dry}} - \frac{\left(\frac{1}{K_{dry}} - \frac{1}{K_0}\right)^2}{\left(\frac{1}{K_{dry}} - \frac{1}{K_0}\right) + \phi\left(\frac{1}{K_f} - \frac{1}{K_0}\right)} \tag{A.11}$$

$$\frac{1}{K_{dry}} - \frac{1}{K_{sat}} = \frac{\left(\frac{1}{K_{dry}} - \frac{1}{K_0}\right)^2}{\left(\frac{1}{K_{dry}} - \frac{1}{K_0}\right) + \phi\left(\frac{1}{K_f} - \frac{1}{K_0}\right)}, \tag{A.12}$$

where equation (A.12) is exactly Gassmann's equation. Hence, Gassmann's equations are a special case of Berryman's equation if the saturated and the dry shear modulus are the same.

Figure A.1 shows the bulk and the shear modulus for different porosities and 0.10 Poisson's ratio of the mineral grains. The relative differences between Gassmann's equations and Berryman's exact theory are

$$\begin{aligned} \Delta_K &= \frac{K_{GA} - K_{BE}}{K_{BE}} \\ \Delta_\mu &= \frac{\mu_{GA} - \mu_{BE}}{\mu_{BE},} \end{aligned} \tag{A.13}$$

where K_{GA}, μ_{GA}, K_{BE} and μ_{BE} are the bulk modulus and shear modulus of Gassmann's equations and Berryman's theory, respectively. For small porosities the differences between Gassmann's equations and Berryman's exact theory is small. However, for porosities larger than 30% the differences exceed 1% and for porosities larger than about 40% the differences exceed 10% and increase rapidly. This discrepancy is due to the violation of the assumption that the saturated and dry shear moduli are the same. For 0.25 Poisson's ratio (Figure A.2) and 0.40 Poisson's ratio (Figure A.3) of the mineral grains, the differences become larger for smaller porosities.

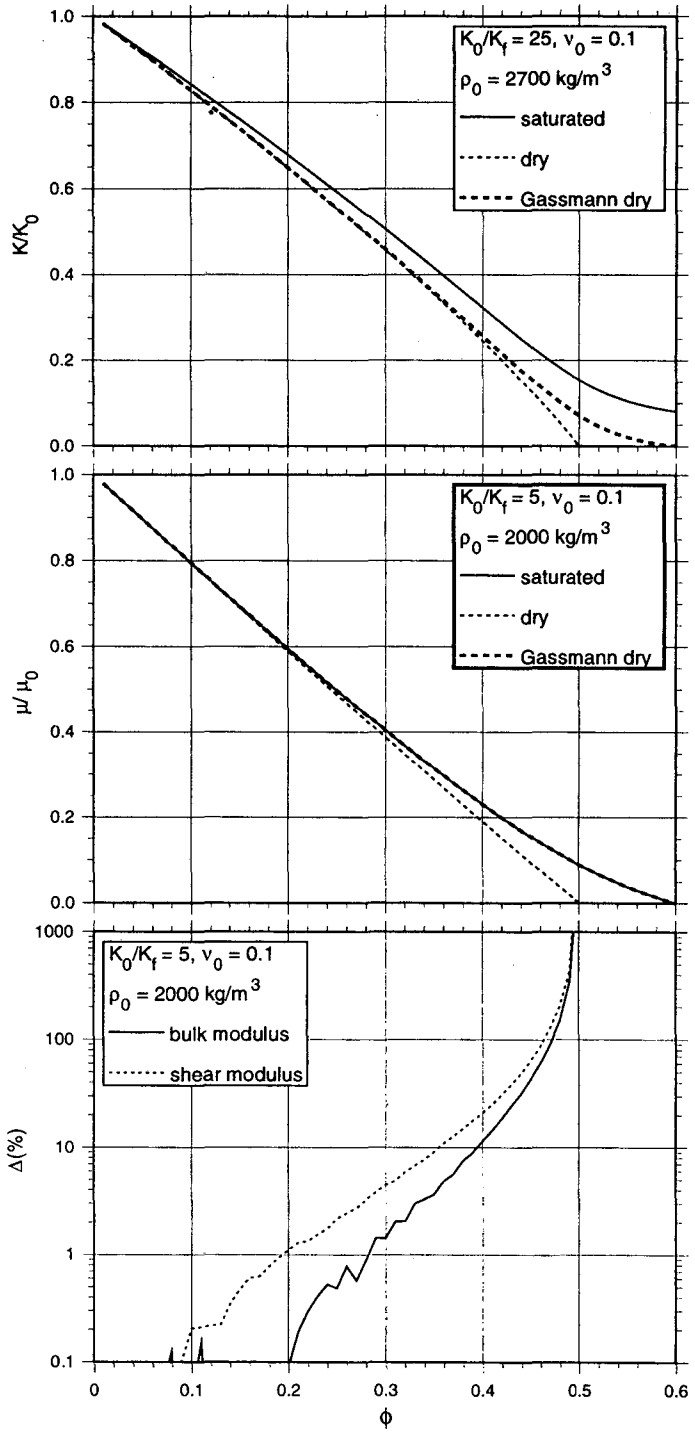

Figure A.1: Comparison between Beryman's exact theory and Gassmann's equations. K is the bulk modulus, μ the shear modulus, Δ the relative difference, ν the Poisson's ratio, ρ the density and ϕ the porosity. $K_0/K_f = 5$ and $\nu_0 = 0.1$.

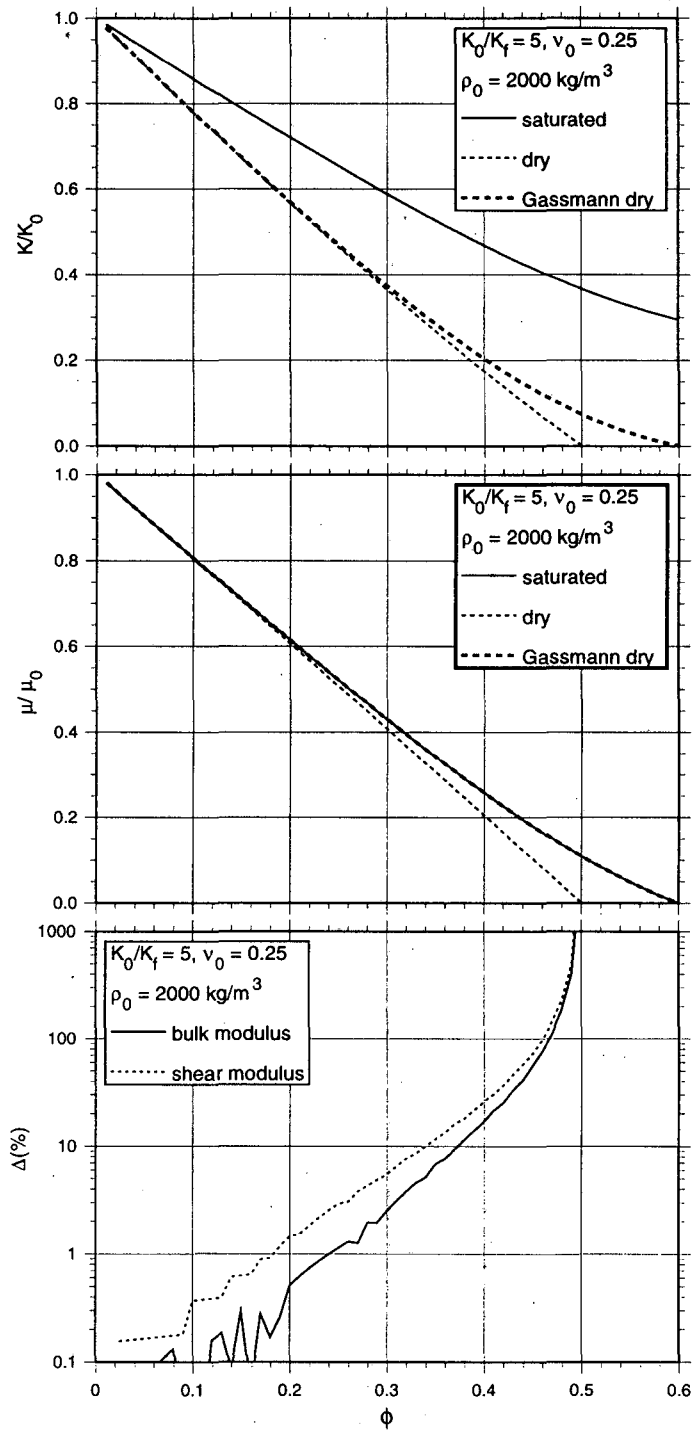

Figure A.2: Similar to Figure A.1: $K_0/K_f = 5$ and $\nu_0 = 0.25$

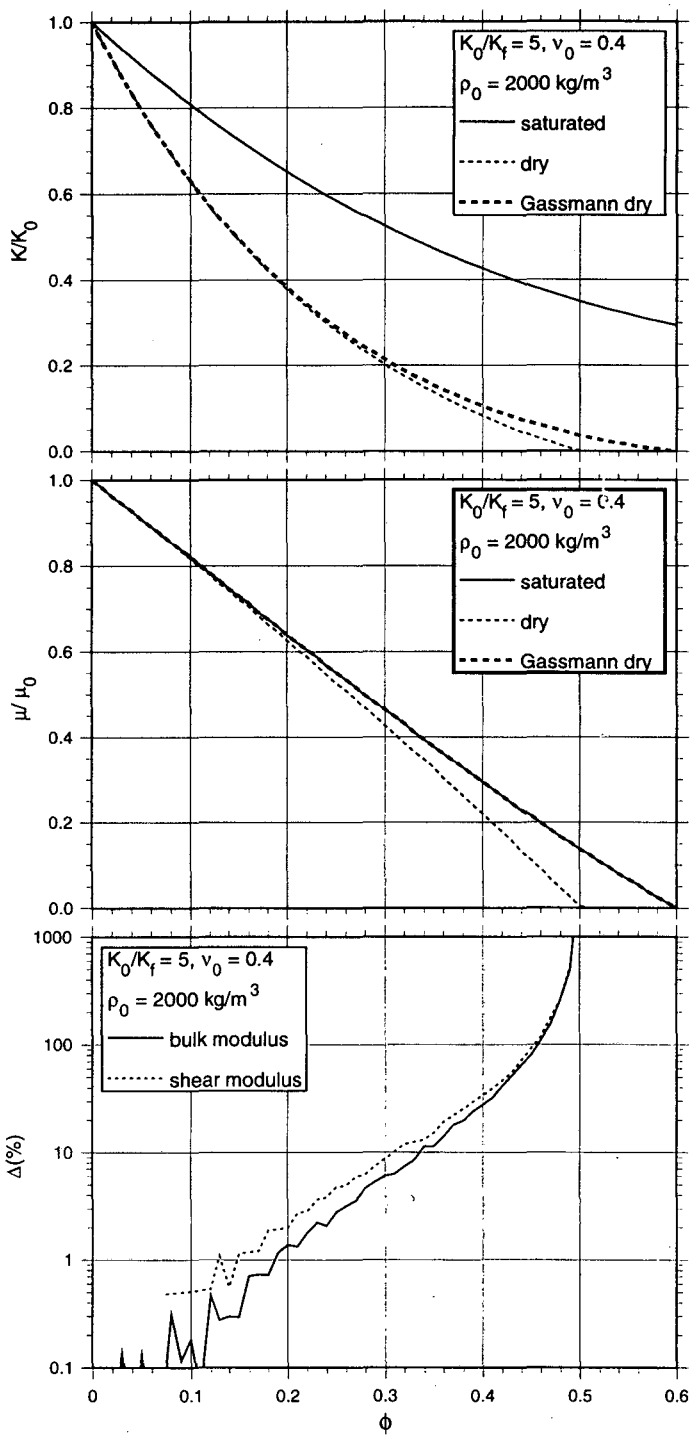

Figure A.3: Similar to Figure A.1: $K_0/K_f = 5$ and $\nu_0 = 0.4$

ERNEST ORLANDO LAWRENCE BERKELEY NATIONAL LABORATORY
ONE CYCLOTRON ROAD | BERKELEY, CALIFORNIA 94720

Prepared for the U.S. Department of Energy under Contract No. DE-AC03-76SF00098

ABT228
LBL Libraries